NASA Contractor Report 4136

Analytical Modeling of the Structureborne Noise Path on a Small Twin-Engine Aircraft

J. E. Cole III, A. Westagard Stokes,
J. M. Garrelick, and K. F. Martini

CONTRACT NAS1-18020
JUNE 1988

NASA

NASA Contractor Report 4136

Analytical Modeling of the Structureborne Noise Path on a Small Twin-Engine Aircraft

J. E. Cole III, A. Westagard Stokes,
J. M. Garrelick, and K. F. Martini
Cambridge Acoustical Associates, Inc.
Cambridge, Massachusetts

Prepared for
Langley Research Center
under Contract NAS1-18020

National Aeronautics
and Space Administration

Scientific and Technical
Information Division

1988

TABLE OF CONTENTS

Table of Contents (Continued)

EXECUTIVE PROJECT SUMMARY

Passenger comfort in aircraft using advanced propeller concepts requires that interior noise levels be comparable with those of existing jet aircraft. Based on the exterior airborne noise levels of current advanced propeller designs, the insertion loss required of the aircraft structure to achieve acceptable interior noise levels is substantial (e.g., 40-50 dB). As a result, all noise paths from the propeller source to the interior must be considered in order to design effective noise control treatments.

The focus of this study is the structureborne noise path of propeller induced noise. We define this path to be the noise induced in the cabin space by unsteady propeller loads acting on the wing. The objective of this study has been to develop analytical models of the entire structureborne path including propeller loading, structural vibrations of the wing and fuselage, and the acoustic space inside the fuselage. Development of these models has been guided by results of testing performed on a small twin-engine aircraft, a Beechcraft Baron 58P, located at NASA Langley Research Center. The analytical models have been used to examine the sensitivity of the interior noise to structural and acoustic parameters.

Loads induced by the propeller on the structure of the wing at the blade-passage frequency and its harmonics are calculated using unsteady aerodynamic theories (Ref. 1). Two mechanisms have been modeled. The first is the loading due to the downwash of the tip vortices on the plane of the wing, this mechanism being applicable to a tractor configuration. The second mechanism is the unsteady thrust resulting from a non-uniform inflow to the propeller. In the tractor configuration the non-uniformity is due to the upstream influence of the wing, while in a pusher configuration the non-uninformity is caused by the wake of the upstream wing or pylon. Calculations are performed for a Hamilton-Standard 8-bladed advanced propeller design in a pusher configuration as well as for the 3-bladed propeller of the Beechcraft Baron (tractor configuration). Several implications for noise control resulting from this modeling are as follows:

A. Nonuniform propeller inflow as a mechanism of thrust generation

(1) When designed for constant steady thrust, a large number of blades provides lower individual blade tip speeds and reduces unsteady propeller thrust levels. For a given propeller rotational speed (i.e., rpm) use of more blades yields a higher value of reduced frequency associated with the blade-passage fundamental; therefore, lower levels of noncompact blade-sectional loadings contribute to total thrust.

(2) The number of propeller blades should be kept even in the pylon-mounted, once-per-revolution excitation mode. In this configuration odd blades yield better coupling between odd harmonics of thrust and those of the inflow nonuniformity and therefore are undesirable. By the same reasoning, if a pusher propeller is considered for general wing installation, it should contain an odd number of blades since the excitation then occurs twice per revolution rather than once.

B. Wing excitation by wake of a tractor propeller

(3) Similar to Item (1) a large number of blades will yield higher reduced frequencies based on wing semi-chord dimension and flight speed. As a result, lower levels of wing pressure distributions are obtained for this mechanism.

(4) Increasing the radius of the propeller should result in a decrease in strength of blade-tip vortices driving the downstream wing. A more gradual spanwise load distribution for individual blades and a lower near-tip value of steady blade-sectional lift result when constant total steady thrust is specified.

A program of testing on the Beechcraft Baron was undertaken to measure the structural characteristics of the wing and fuselage and to evaluate the effects of alterations on the interior noise. This experimental program is documented in Ref. 2. Tests included measurements of structural and acoustic responses to impact excitation, measurements of structural and acoustic loss factors, and modal analyses. The measured structural characteristics were used to guide the development of the analytical models of the structureborne path. Path alterations included the addition of simulated fuel mass, changes in the torque of the bolts connecting wing and fuselage, and the addition of acoustic absorption to the interior space. Major conclusions drawn from the results of these tests include the following:

(1) the addition of approximately one-quarter of the mass of a full fuel load to the tanks on the inboard leading edge of the wing results in a decrease in interior noise by 10-15 dB in the frequency range 50-1000 Hz. (Fig. 11a, Ref. 2);

(2) impact excitation of the wing produces higher interior noise levels than impact excitation of the fuselage at frequencies below 150 Hz (Fig. 6a, Ref. 2);

(3) the airborne flanking path to the fuselage induced by radiation of sound from the vibrating wing is approximately 15 dB below the direct structureborne path (Fig. 8, Ref. 2);

(4) increasing the torque on the wing attachment bolts from 50 to 150 ft-lbf has a negligible effect on the interior noise (Fig. 9, Ref. 2);

(5) adding acoustic absorption to the fully trimmed interior produces a small reduction in interior noise above 600 Hz (Fig. 12, Ref. 2).

Analytical models of the structureborne path including the wing, fuselage, and cabin space are documented in the present report. The fuselage structure is modeled as a cylindrical shell and includes discrete circumferential stiffeners and the effects of longitudinal stringers. The presence of air both inside and outside the shell is included as well as an acoustically absorptive blanket liner on the interior. Parameters of the model are based on physical dimensions of the fuselage as well as on the results of the measurements. Good agreement with the measurements is obtained for structural and acoustic response functions (Figs. II.14 and II.15, respectively). Major conclusions regarding noise control on the Beechcraft Baron drawn from parameter studies using this model include the following: (1) increasing the structural loss factor by an order of magnitude results in a broad band reduction of interior noise levels by 5-10 dB above 100 Hz (Fig. II.21); (2) the interior noise is relatively insensitive to structural stiffness away from the excitation location (see Figs. II.19 and II.20).

The wing structure is modeled using the finite element method. Included in the model are the spars, ribs, and skin. The fundamental bending and torsional modes measured on the wing of the Baron are well matched by the model, and at higher frequencies the mean level of the calculated response is in good agreement with the measurements (Figs. III-8). Parameter studies with this model show sensitivity of the structural response to the membrane stiffness of the wing skin. In addition the simulated presence of fuel is effective in reducing the response levels of the wing (Figs. III.6).

The analytical models of the wing and fuselage have been coupled by simulating a connection of four bolts. The resulting global structural model is used to calculate interior noise levels resulting from the distributed unsteady loading induced on the wing by the propeller downwash. Interior noise levels are found to be sensitive to impedance matching in each of the degrees-of-freedom connected between the wing and fuselage structures (Fig. IV.4). Calculated interior noise levels are found to be approximately 10 dB below measured in-flight noise at the fundamental blade-passage frequency; however, the calculated response is quite variable within the associated one-third octave band of frequencies.

Conclusions drawn from this global model with regard to noise control are the following: (1) control of structureborne noise over regions of frequency may be possible by mismatching structural impedances in one or more directions between wing and fuselage structures; (2) the sensitivity to frequency of the structureborne path obtained in this study suggests that substantial narrowband benefits can be achieved through design of wing and fuselage structures. While current analytical tools are not sufficiently accurate for a priori determination of beneficial designs, it may be possible to achieve narrowband improvements through the process of design iteration.

A statistical energy model of the structureborne noise path of the global aircraft structure has also been developed to gain further insight into mechanisms influencing the interior cabin pressure. Assumptions of this high frequency technique with respect to long wavelength compressional waves are found to be violated in the frequency range of interest. Estimates of loss factors based on measurements indicate that limiting results for the case of heavy damping are applicable to the Baron structure. The conclusion drawn from this result is that damping added to any subsystem of the Baron (viz., wing, fuselage, cabin space) should be equally effective in reducing the interior noise.

I. INTRODUCTION

Analytical models of the structureborne path consisting of the wing and fuselage structures as well as the interior acoustic space of the cabin have been developed and used to evaluate sensitivity to structural and acoustic parameters. Different modeling approaches have been used to examine aspects of the structureborne path. These approaches have been guided by a number of considerations including the geometry of the structures, the frequency range of interest, and the tractability of the computations.

The focus of the modelling has been a six passenger twin-engine aircraft, a Beechcraft Baron 58P. Measurements performed on this aircraft at NASA Langley Research Center to help develop the models are detailed in the companion report (Ref. 2).

An analytical representation of the fuselage and cabin space as an orthotropic, frame-stiffened cylindrical shell having interior and exterior fluid is described in Section II. Modeling of the wing using finite elements is presented in Section III. Coupling of these models through simulated bolt connections to form a global model of the structure is discussed in Section IV. Section V describes the development and results of high frequency asymptotic modeling of the entire structureborne path. Results of each of these models are compared with results from the experimental testing.

II. FUSELAGE AND CABIN SPACE MODEL

A. Introduction

The geometry of the Beechcraft Baron's fuselage is irregular, being somewhat rectangular in the lower portion and curved near the top. In addition the cross section is tapered towards the rear (see Fig. II.1). The irregularity of the geometry carries through to the structure; structural stiffeners are neither uniform in dimension nor located at uniform intervals (Fig. II.2a). Internally, the seats take up a substantial portion of the volume (see Fig. 2b). By way of contrast, the fuselage cross section of larger aircraft that ultimately will be powered by propfan technology (e.g., Boeing 7J7, McDonnell Douglas MD-80) is more nearly cylindrical.

Although a general modeling approach for treating such irregular geometries such as the finite element method could be used to model the fuselage and cabin space, it would result in a large model and require simplifications in the structure to maintain a tractable model size. This modeling approach is therefore not adopted for the fuselage, although it is used for modeling the dynamics of the wing. Rather, a model of the Baron's fuselage and cabin space based on a cylindrical shell is developed. This modeling approach is tractable and applicable to the more regular geometries of advanced aircraft designs.

The assumption of a cylindrical geometry for the fuselage structure and the internal cabin space permits a computationally efficient model to be constructed that contains many of the physical elements considered to be important to the structureborne noise path along the fuselage. These elements include structural stiffeners, in- and out-of-plane noise paths, structural damping, both interior and exterior fluid, acoustic absorption along the interior surface, and multi-directional excitation loads. An overview of the model is given in the next sub-section; details of the modeling approach are found in Appendices A-E of this report.

Several different response quantities calculated from the model include the following: frequency dependence of drive-point accelerances and structural acoustic transfer functions; fuselage acceleration and cabin pressure as functions of space; and fuselage acceleration and cabin pressure as functions of spatial wavenumber. Analysis of these responses provides insight into propagation paths and the influence of structural and acoustic elements on the cabin acoustic pressure field.

B. Model Overview

The fuselage structure is modeled as an orthotropically-stiffened cylindrical shell that both contains and is immersed in a compressible fluid. Simply-supported (i.e., shear diaphragm) boundary conditions are assumed to exist at the ends of the shell. These boundary conditions permit a solution to be obtained in terms of simple modal expansions in the axial and circumferential directions of the shell.

Structural stiffeners on the fuselage of the Baron consist of longitudinal stringers at various separation distances along the fuselage ranging from 5 to 9 inches. Stiffening in the orthogonal direction is by means of frames spaced roughly 12 inches apart.

Discrete stiffeners modeled as line loads imparted to the structure are compatible with the model of a simply-supported shell. When modeled in this manner, however, discrete stiffeners in either the axial or circumferential directions along the shell couple all vibrational modes in the same direction. Solution for the modal amplitudes involves a set of simultaneous equations for each mode of order N_dN_s where N_d is the number of degrees-of-freedom of attachment (e.g., 3 translational and 1 rotational) and N_s is the number of stiffeners.

Given the large number of discrete stiffeners and shell modes involved, an alternative assumption for modeling the effects of stiffeners is used. The assumption represents a hybrid approach in which the relatively sparsely distributed circumferential frames are included as discrete stiffeners while the stiffening effect of the more closely spaced axial stringers is averaged in an orthotropic shell model. This approach permits panel resonances in the skin located axially between circumferential stiffeners to be included but does not allow for resonances in the skin between stringers.

The presence of fluid inside and outside the shell is included by expanding the pressure field in the same axial and circumferential modes as the radial displacement of the shell. By invoking compatability of shell and fluid displacements at the shell surface, the modal loading provided by the fluid motion on the shell is computed. Since the axial modes for the fluid are those of the radial shell displacement (i.e., $\sin k_m x$, where $k_m = m\pi/L$, L is the shell length between supports and $m=1,2,\ldots$), the acoustic pressure vanishes at both ends of the shell. Although this expansion allows the fully coupled fluid-structural interaction problem to be solved mode by mode, it introduces an artificial "pressure-release" condition at the ends of the cabin space.

As a means of avoiding zero pressure at the cabin ends, the model assumes the length between simple supports to be longer than the actual length of the cabin space. Large structural frames inboard of the simple supports are used to terminate the structure, and the pressure field within this shortened space is used to represent the cabin pressure.

An acoustically absorptive lining on the interior of the fuselage is developed by extending the model of Ref. 3. This model assumes a locally reacting acoustic element having mass, stiffness, and resistance. The fuselage motion excites this element and its response then excites the interior fluid space. Because the shell and fluid are fully coupled, the loading of the fluid acts through the acoustic lining to impart loads on the shell.

For completeness the details of the models of the shell, fluid, frames, and acoustic lining are given in Appendices A-F.

C. Model Parameters

The physical properties and dimensions of the Beechcraft Baron 58P are used to define the numerous parameters entering the analytical model of the fuselage and cabin space. Because of the irregularity of the fuselage geometry and structural dimensions, however, this process is not straight forward. The geometry of the fuselage and cabin space, assumed to be cylindrical, is taken to have a diameter of 44 inches and a length of 154 inches. These dimensions approximate the maximum cross-sectional dimensions of the fuselage and the length of the interior cabin space (see Figs. II.3 and II.4). As discussed subsequently, the length of the shell between its simple supports is 24 inches longer than the 156 inch length of the fuselage. The thickness of the fuselage skin is 0.020 inches, and the mass of the attached damping treatment is accounted for by taking the mass density of the skin to be 3.0 times greater than that of aluminum.

Structural damping is included in the model through a material loss factor (i.e., $E^*=E(1-i\eta_s)$, where E is the elastic modulus of the shell material and η_s is the loss factor). The loss factor is determined from measurements of the decay rate of structural vibrations on the fuselage. Results presented in Fig.II.5 show a reasonably constant value of $\eta_s=0.03$.

The dimensions of the axial stringers on the fuselage shown in Fig.II.6 are reasonably constant throughout the fuselage; however, their spacing varies considerably ranging from 3 inches on sections aft of the cabin to 10 inches along mid portions of the fuselage. A uniform spacing of 8 inches is selected for evaluating the orthotropic shell stiffness.

Definition of parameters for the axisymmetric frame stiffeners in the analytical model is made difficult by the extreme irregularity of the transverse stiffeners on the Baron. The dimensions of each of the physical stiffeners vary with transverse location, being larger near the bottom and smaller along the sides and top of the fuselage. The two most important transverse stiffeners in the structureborne path are those that bolt to the fore and aft wing spars. These stiffeners are highly built up at the bottom of the fuselage where they attach to the wings (see Fig. II.7). The dimensions of these two wing attachment frames in the analytical model are selected to be representative of the physical frames along the side wall, that is, somewhat less than the dimensions of the highly stiffened bottom portion. The dimensions of the equivalent "Tee" section frame are given on Table II.1. Six smaller frames spaced 16 inches apart are included to represent the remaining transverse fuselage stiffeners (see Table II.1). In addition large frames located 12 inches in from each end of the simply-supported shell are used in the model to represent the termination of the cabin and to include the mass of the nose and tail sections of the fuselage. Dimensions for these frames are also given in Table II.1 (see Fig. II.4).

Air is assumed to fill the interior of the shell and to surround it on the exterior. The purpose of the exterior air is to allow for radiation damping. As discussed in Section B and Appendix B the pressure field in the analytical model vanishes at the axial locations of the simple supports. Stated differently the fluid boundary condition of the simple supports is one of a pressure release termination. This termination clearly does not represent the physical boundary condition for the fluid forward and aft ends of the cabin space. A means to allow for more representative acoustic termination of the cabin space in an unframed shell is developed in Ref. 5. In the presence of discrete frame stiffeners however this procedure would greatly complicate the analysis.

As a means of partially compensating for the pressure-release acoustic termination at the simple supports, the cabin space is assumed to be located in-board of the simple-supports by 12 inches at each end. This distance which measures one-quarter of an acoustic wavelength at 275 Hz is insufficient to remove entirely the effects of the pressure release terminations from the pressure field at low frequencies; however, it eliminates the region near the supports where the largest gradients in pressure are found.

The acoustic treatment along the side walls and ceiling of the Baron is reasonably dense fiberglass having a thickness of approximately 1/2 inch. This acoustic lining is modeled using parameters for the specific flow resistance and density of similar materials (see Table II.1). These parameters are used to obtain the plane wave absorption coefficient for the material backed by a rigid termination (see Appendix E). Shown on Fig. II.8 is the frequency dependence of the absorption coefficient for different material thicknesses.

D. Results

1. Response Quantities

Several response functions are calculated from the analytical model for each set of parameters. The drive point accelerance in three orthogonal directions at the forward bolt attachment point (location 12, Fig. II.3) is calculated as a function of frequency to compare with measurements. Other functions calculated for comparison with measurements are input power and the transfer function between cabin acoustic pressure at microphone location 1 (see Fig. II.3) and the force applied to point 12 in three orthogonal directions. Results for the accelerance and transfer function are calculated in one-third octave bands, the band levels being obtained from a sum of five frequencies within each band. The purpose of this presentation is to minimize the effects of narrow-band oscillations in these functions.

For purposes of diagnostics and insight, two other response functions are calculated. The variation with longitudinal distance along the shell of acceleration and pressure is calculated at three frequencies. Additonally the spatial Fourier transform of the response along the shell aft of the drive is evaluated. This calculation described in Appendix F results in the axial wavenumber spectrum at specified frequencies. Like its counterpart in the temporal domain, this presentation of the spatial information in transform space is useful for identifying certain features of the response field including dominant modes of structural propagation (e.g., effective flexural wavenumber on the shell), direction of propagating modes, and wavenumber contributions to the acoustic pressure field.

2. Unframed Heavily Damped Fuselage

It is useful to examine a relatively simple structural configuration as a limiting case to guide the interpretation of results from more complex configurations. The structure is an orthotropic shell having no circumferential frame stiffeners that is excited by point loads. A structural loss factor of 0.30 is assumed as a means of reducing the effects of reflections from the supported ends of the shells and thus to provide responses representative of a shell that is infinite in length. The acoustic lining on the interior of the shell is not included in the calculations.

The spatial dependence of the acceleration along the generator of the shell containing the excitation point is shown on Fig. II.9 at three frequencies. The response peaks at the point of excitation (x=67 in.) and decays away from this point. The decay is relatively monotonic on the larger side of the shell, while on the shorter side, the oscillations result from reflections induced by the support. Since the frequency range is well below the fundamental breathing mode resonance frequency of the shell (i.e., $f_b = \frac{c_p}{2\pi a} = 1500$ Hz, where c_p is the speed of compressional waves in the skin), the structural waves are membrane-like rather than purely flexural (see Ref. 6).

The spatial dependence of the acoustic pressure field in the shell is shown on Figs. II.10. The four curves shown at each frequency give the pressure at different radii along the generator containing the applied load. For this simple structure the pressure field at the shell surface is nearly identical to the acceleration field that excites it. As we shall see this is not the case in the presence of structural discontinuities or acoustic liners.

The spatial wavenumber spectra of the acceleration and pressure given at the three frequencies on Figs. II.9 and II.10 are shown on Figs. II.11. For the given frequency each figure shows the wavenumber spectrum of the wall acceleration and the pressure at a radius of 10 inches along the generator that includes the excitation. These spectra are obtained from the spatial field on one side of the excitation ($75'' \leq x \leq 165''$). For reference the wavenumber of an acoustic wave propagating as a plane wave along the axis of the cylindrical shell (i.e., the fundamental mode in a rigid duct) is given by

$$k_a = \pm \frac{\omega}{c_a}$$

where c_a is the sound speed in air. At frequencies of 125, 250, and 500 Hz, these wavenumbers are respectively, 0.060, 0.12, and 0.24 in^{-1}. In Fig. II.11a

(125 Hz) the pressure peaks near k=0 while the structural acceleration shows a forward propagating wave peaking near $k=.15\ \text{in}^{-1}$ and a negative propagating wave having the same wavenumber (i.e., $k=-.15\ \text{in}^{-1}$) but reduced in amplitude by approximately 8 dB. At 250 Hz peaks having comparable amplitude in the acoustic pressure are found near the acoustic wavenumbers. The structural field is dominated by a forward propagating wave near $k \simeq .25\ \text{in}^{-1}$. The forward and backward propagating structural waves at 500 Hz are clearly seen on Fig. II.11c. At this frequency however the wavenumbers contributing to the acoustic field are reasonably broad within the acoustic range.

The drive-point accelerances in three directions (i.e., a_r/F_r, a_x/F_x, a_ϕ/F_ϕ) are shown in Fig. II.12 along with the root-mean-square (RMS) accelerance (i.e., $[(a/F)_r^2+(a/F)_x^2+(a/F)_\phi^2]^{1/2}$). The relatively constant level of the axial accelerance at low frequencies is the mass-like response of the shell. Because of the fixed boundary conditions on the radial and circumferential motions of the shell at the supports, the response at very low frequencies in these directions is stiffness-like (i.e., $a/F \sim \omega^2$). The highest accelerance is in the radial direction.

The transfer functions between acoustic pressure at the equivalent location of the rear seat on the side opposite of the excitation and the applied force in three directions is shown on Fig. II.13. For this configuration the transfer function increases on average with frequency. The RMS transfer function is dominated by the radial and circumferential transfer functions.

For purposes of comparison the pressure radiated to the farfield by a force-driven orthotropic flat plate of infinite extent is also shown on Fig. II.13. This model which assumes the plate to be submerged in an infinite acoustic medium is known to somewhat underestimate the low frequency sound radiated externally by a force driven shell. When the acoustic pressure is evaluated along one principle direction of the plate (e.g., the direction of the longitudinal stringers in the fuselage skin), the transfer function is given by

$$\frac{p}{F} = \frac{-ik}{2\pi R} \frac{\cos\theta}{1-i \frac{\rho_s}{\rho} kh\cos\theta \left[1- \frac{\omega^2}{\omega_c^2} \sin^4\theta\right]} \tag{II.1}$$

where $k=\omega/c$, R is the range, ($\rho_s h$ is the plate mass per unit area, θ is the angle measured from the normal to the plate, and ω_c is the coincidence frequency). If we include the mass of stringers in an effective material density ρ_{se} and the stiffness of the plate in an effective plate thickness h_e, the coincidence frequency is given by

$$\omega_c = 2\pi f_c = c^2 \left[\frac{12\rho_{se}}{E} \frac{h}{h_e^3}\right]^{1/2} \tag{II.2}$$

where h is the thickness of the unstiffened plate and c is the sound speed in air. The equivalent density for the fuselage skin is 3 times that of aluminum while the bending stiffness in the stringer direction is equivalent to a plate 0.19 inches thick. For these parameters the coincidence frequency is 1.4 kHz. Most of the frequency range of interest is therefore well below coincidence. Furthermore the plating mass impedance (i.e., $\rho_{se}\omega h$) is much greater than the characteristic impedance of air (i.e., ρc) above a frequency of several Hertz. Therefore the ratio of pressure to force approaches a constant value over much of the frequency range of interest, this value being given by

$$\frac{p}{F} \simeq \frac{\rho}{2\pi R\rho_{se} h} \tag{II.3}$$

Using a range of 81 inches and a density given by ρ_{se}, we obtain the following narrowband pressure level:

$$20 \log p/F = 73.8 \text{ dB (re: } 20\mu\text{Pa/lbf)} \tag{II.4}$$

when expressed in one-third octave band levels the transfer function is equal to

$$p/F(\text{dB}) = 73.8 + 10 \log (.23 f_c) \text{ (re: } 20\mu\text{Pa/lbf)} \tag{II.5}$$

where f_c is the center frequency of the band. As seen on Fig. II.13 this flat plate transfer function is greater than the results for the damped unframed shell below 200 Hz, but the levels are comparable at high frequencies. This comparison is consistent with there being no reverberant buildup of the pressure field within the cabin.

3. Baseline Configuration

The baseline configuration for the fuselage is defined as the frame stiffened, orthotropic shell having a structural loss factor of 0.03 and a 1/2 inch thick acoustic blanket. The complete list of parameters for this configuration is given on Table II.1 Results calculated using this set of parameters are compared with experimental data and with the set of calculations on the simpler configuration discussed in the previous section. In subsequent sections the sensitivity of the results to several important parameters is presented.

The measured and calculated drive-point accelerances at the top forward bolt attachment point of the fuselage are shown respectively on Figs. II.14a and b. The three measured curves show the accelerance in the spanwise, lift, and thrust directions on the fuselage while the calculated curves provide the results in the radial, circumferential, and axial directions of the cylindrical shell. These two sets of directions are coincident when the bolt is assumed to be located at the horizontal diameter of the cylindrical shell. The calculated RMS accelerance is higher than that measured throughout the frequency range with the differences being greater above 200 Hz. This high RMS accelerance is due to the high radial accelerance over most of the frequency range. The likely reason for the lower experimental accelerance is the stiffened section of the lower fuselage where the wing spar attaches. Because the structure in the analytical model is axisymmetric and uses average dimensions, this enhanced stiffness is not completely accounted for.

The measured and calculated transfer functions between cabin pressure at location 1 and forces applied to the fuselage at the location of the top forward bolt are shown on Fig. II.15a and b, respectively. The two experimental results on Fig. II.15a are direct and reciprocal measurements for a spanwise excitation. Calculated results are given on Fig. II.15b for excitations in the three shell directions. Over most of the frequency range the transfer function for excitation in the thrust direction is well below those for radial and circumferential excitations. Because of the low frequency stiffness of the simply-supported shell, the calculated results are lower than the measured values below approximately 40 Hz. Above 100 Hz the calculated functions for radial and circumferential excitations are comparable with the direct measured transfer function.

The spatial variation of the fuselage acceleration along the generator containing the excitation is shown on Fig. II.16 for three frequencies. Several differences are found when these results are compared with those of the heavily damped unframed shell (Fig. II.9). The response at 125 Hz contains small features occuring at the locations of the frames. At the higher frequencies the smaller structural damping results in acceleration levels that do not display much spatial decay along the length, while at 500 Hz scattering of structural waves from the frames and from the supports lends to a strong standing wave pattern.

Shown on Figs. II.17a-c is the spatial dependence of the pressure along the shell generator containing the radial excitation at three frequencies. The results at 125 Hz are similar with those of the highly damped unframed shell (Fig. II.10) in the vicinity of the excitation. At the higher frequencies, however, there is little similarity with the results of Fig. II.10. The surface pressure does not follow that of the acceleration as well due to the presence of the acoustic blanket and to radiation and scattering of acoustical energy at the frame stiffeners. Substantial variations inside the shell interior space in the pressure field with axial and radial distances is found (e.g., 30-40 dB).

The spatial wavenumber spectra of the shell acceleration and of the pressure field at a radius of 10 inches is shown on Figs. II.18. As in the previous wavenumber calculations the spatial response between 75 and 165 inches (i.e., one side of the excitation) is transformed to obtain the response in wavenumber space. At 125 Hz (Fig. II.18a) both the acceleration and the pressure are dominated by forward propagating waves, the wavenumber of the structural wave being somewhat higher than that of the acoustic wave. The wavenumber spectra at 250 Hz shown on Fig. II.18b indicate that the shell acceleration is dominated by a forward propagating wave. The acoustic field however is dominated by a backwards propagating wave, this presumably arising because of scattering and radiation at the frame stiffeners. Similar characteristics are found in the wavenumber spectra at 500 Hz (Fig. II.18c).

4. Effects of Parameter Changes on Calculated Response

a. Circumferential Stiffness

As a means of evaluating the effect of the circumferential stiffening frames on the interior sound field, results are calculated for a configuration having frames only at the drive location and at the "ends" of the cabin space (i.e., x=12 and 166 inches). None of the smaller intermediate frames nor the large frame representing the aft spar carry-through are present in this configuration. By maintaining the frame at the drive point, the drive point accelerance is similar to that of the baseline configuration. All other structural and acoustic parameters are those of the baseline configuration.

Shown on Fig. II.19 are the pressures at cabin location 1 per fuselage excitation force for the baseline (i.e., 10 frame) configuration and the four-frame configuration. The transfer functions are the RMS values for excitations in the three orthogonal directions at the bolt location. Although there are regions where differences approaching 6 dB are found, there is no consistent difference between the two transfer functions shown on Fig. II.19. The implication of this result is that scattering caused by the presence of the intermediate frames is not a strong effect on the calculated interior sound field in this frequency range.

b. Axial Stiffness

The axial stringers add significant stiffness to the thin skin of the fuselage (h_s=0.02 inch). Using the stringer parameters of the baseline model (Table II.1), the static stiffness of the skin with attached stringers is equivalent to a uniform aluminum plate having a thickness of 0.19 inches.

The effect of the axial stiffness of the shell on the interior pressure field is evaluated by reducing the stiffness of the stringers in the analytical model. This is accomplished by reducing both the elastic and shear modulus of the stringers (i.e., E_{st} and G_{st}) by a factor of four. All other parameter values given on Table II.1 are maintained.

Shown on Fig. II.20 are the RMS transfer functions between acoustic pressure and excitation force for the configuration having more compliant stringers and the baseline configuration. Aside from small changes at frequencies below 100 Hz, little difference is found in the transfer function between these two configurations. This implies that the cabin pressure is not a strong function of stringer stiffness. Since this stiffness primarily determines the flexural stiffness of the skin, this result is consistent with the view that the pressure field is dominated by the membrane response of the shell in this frequency range.

c. Structural Damping

The role of structural damping on the interior pressure field is examined by calculating the response of the frame stiffened shell model using a structural loss factor ten times larger than that of the baseline configuration. Little change is found in the drive-point accelerances, these response functions for simple structures being known to have a weak dependence on damping (Ref. 7). The RMS transfer functions between acoustic pressure and excitation force are compared on Fig. II.21. A reduction of approximately 15 dB in the peak at 50 Hz is found for the more highly damped structure. Furthermore, above 100 Hz a reduction of 5-10 dB relative to the baseline configuration is achieved through the enhanced structural damping. This result is consistent with the statistical energy analysis in Section V which would give a 10 dB reduction.

Because the drive-point shell response is minimally influenced by damping, the reduction of interior pressures shown on Fig. II.21 must be achieved by a reduction in the components of the structural field that propagate along the shell. Since the reductions are on the order of 6 dB, however, it is inferred that the magnitude of these contributions to the pressure field are comparable to the coherent components of the pressure field contributions resulting from the nonpropagating near field of the structural excitation. The broadband effectiveness of structural damping is particularly useful for reduction of tonal noise in a complex structure such as the fuselage when narrowband structural tuning becomes impractical.

d. Acoustical Absorption

Acoustical absorption is included in the analytical model through the parameters of the blanket liner on the interior of the shell. Over most of the frequency range the acoustic wavelength is reasonably large in terms of typical thicknesses of an acoustic liner (e.g., $\lambda_{ac} \tilde{=} 10$ ft at 100 Hz). Because of this the acoustic liner would be expected to have little effect on the interior pressure field at low frequencies.

Results in Fig. II.22 showing the transfer function for three thicknesses of the acoustic blanket are consistent with this expectation. Except for the blanket thickness all parameters are those of the baseline configuration (Table II.1). Differences between the results on Fig. II.22 do not appear below 150 Hz. The insensitivity of the internal pressure field to absorption at low frequency using a more simple model has also been found. Substantial effectiveness with increasing blanket thickness is found in the frequency range above 500 Hz. This high frequency blanket effectiveness is somewhat better than that predicted by the statistical energy analysis (Section V) where cabin pressure level is found to vary as $-10 \log \alpha_a$ (where α_a is the acoustic absorption coefficient given on Fig. II.8).

The relatively flat frequency dependence of the transfer function above 200 Hz obtained using a two inch blanket thickness is similar to the character of the transfer function measured on the Baron (Fig. II.15a). Although the acoustic blanket contained in the sidewall trim is approximately 0.5 inches in thickness, the 6 seats add substantially to the interior absorption. The absorption added by the seats was not directly measured; however, the acoustic loss factors derived from reverberation time measurements are shown on Fig.II.4 for the bare and fully trimmed cabin. Based on the analytical results for a 0.5 inch blanket shown on Fig. II.22, the increased loss factor at low frequency in the fully trimmed cabin is attributed to the presence of the seats. Under this assumption, a 2 inch thick blanket in the analytical model is a more representative value for the acoustic liner.

TABLE II.1

NOMINAL DIMENSIONS AND PARAMETERS FOR ANALYTICAL MODEL OF THE FUSELAGE AND CABIN SPACE

I. MATERIAL

A. Shell (Aluminum)

Elastic modulus (psi)	1.0×10^{7}
Poisson's ratio	0.30
Mass density (effective) ($\mathrm{lbf\text{-}s^2/in^4}$)	7.77×10^{-4}
Loss factor	0.03

B. Frames and Stringers (Aluminum)

Elastic modulus (psi)	1.0×10^{7}
Poisson's ratio	0.30
Mass density ($\mathrm{lbf\text{-}s^2/in^4}$)	2.57×10^{-4}
Loss factor	0.03

C. Acoustic Fluid (Air)

Mass density ($\mathrm{lbf\text{-}s^2/in^4}$)	1.13×10^{-7}
Sound speed (in/s)	1.30×10^{4}

D. Acoustic Liner (Fiberglass)

Mass density ($\mathrm{lbf\text{-}s^2/in^4}$)	1.10×10^{-6}
Flow resistivity (lbf-s/in)	5.50×10^{-3}

II. DIMENSIONS

A. Shell

Length (in)	178.00
Radius (in)	22.00
Thickness (in)	0.02

B. Frames	End	Driven	Small
Web thickness (in)	2.00	0.50	0.06
Web length (in)	4.00	2.00	2.00
Flange thickness (in)	2.00	0.50	0.06
Flange length (in)	4.00	2.00	1.00

C. Stringers

Cross-sectional area (in^2)	8.20×10^{-2}
Moment of inertia of cross-section about centroidal axis (in^4)	2.10×10^{-3}
Distance to centroidal axis (in)	0.15
Torsional stiffness ($lbf\text{-}in^2$)	1.22×10^{2}
Spacing (in)	8.00

D. Acoustic Liner

Thickness (in)	0.50

Fig. II.1 Test aircraft Beechcraft Baron 58P in laboratory space at NASA Langley Research Center.

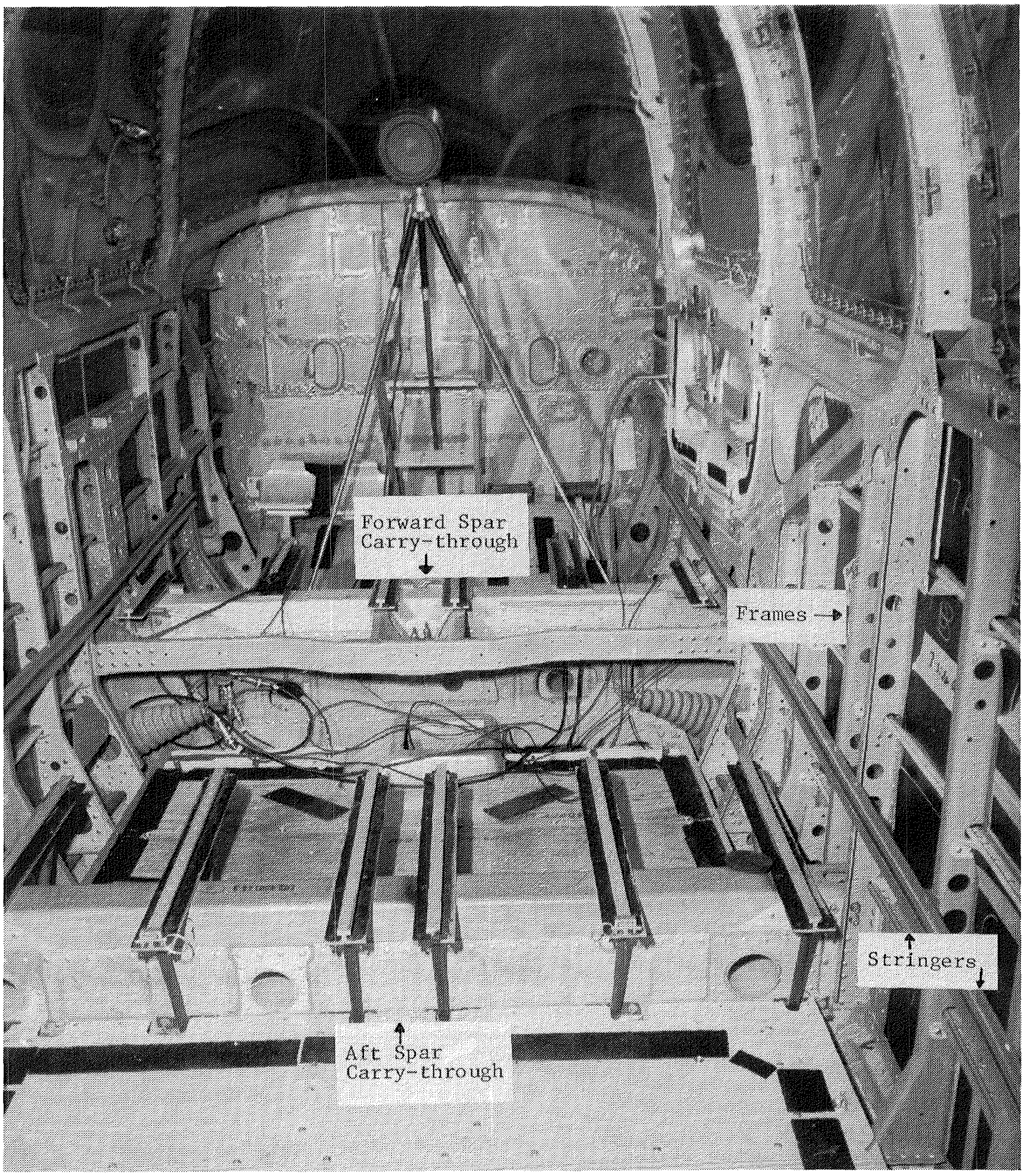

Fig. II.2a View looking forward of the bare cabin of the Beechcraft Baron showing forward (a) and aft (b) wing spar carry-through structures.

Fig. II.2b View looking aft of the fully-trimmed cabin of the Beechcraft Baron.

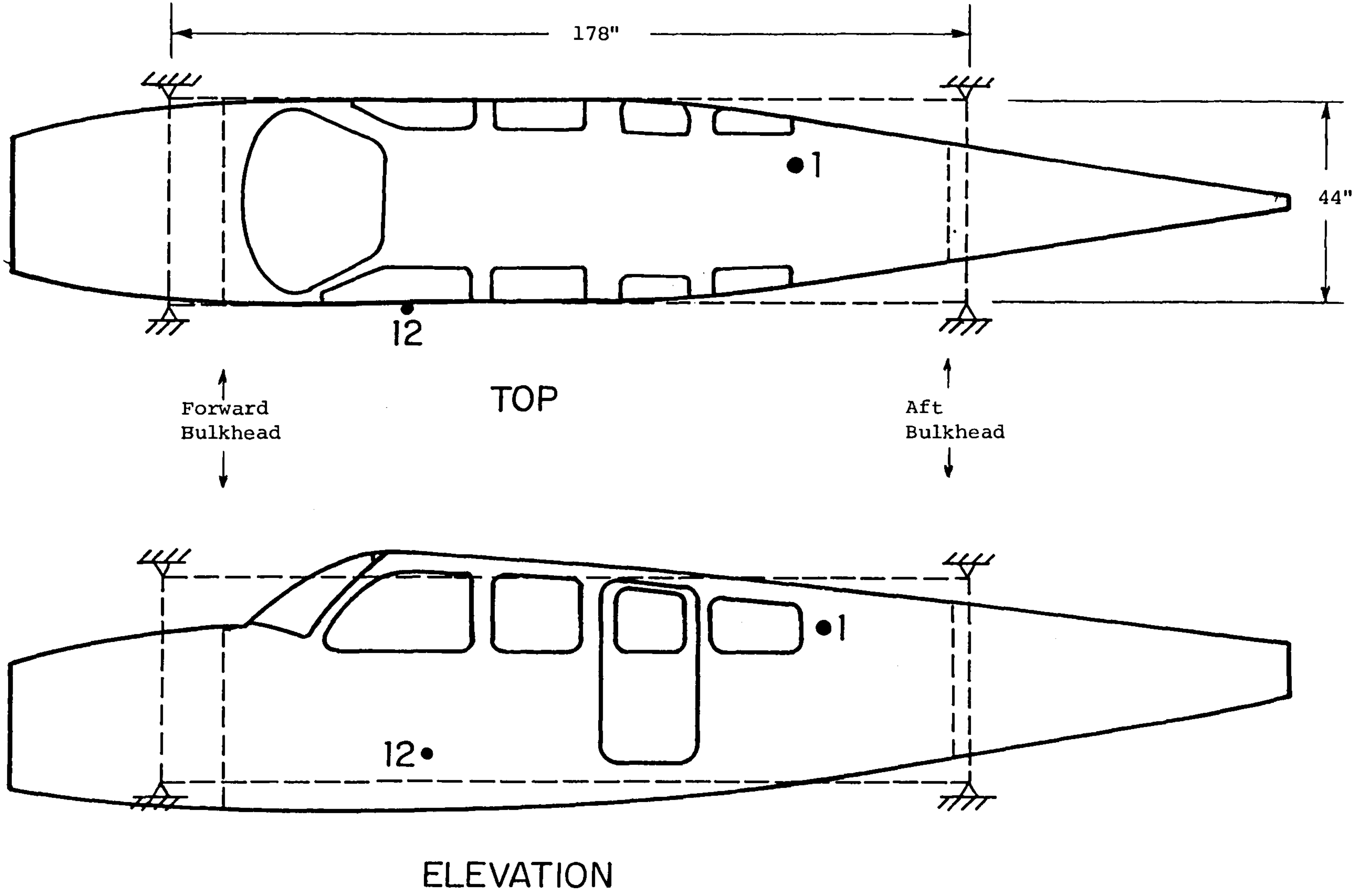

Fig. II.3 Fuselage geometry along with microphone (1) and excitation locations (12) showing equivalent cylindrical shell used in the analytical model.

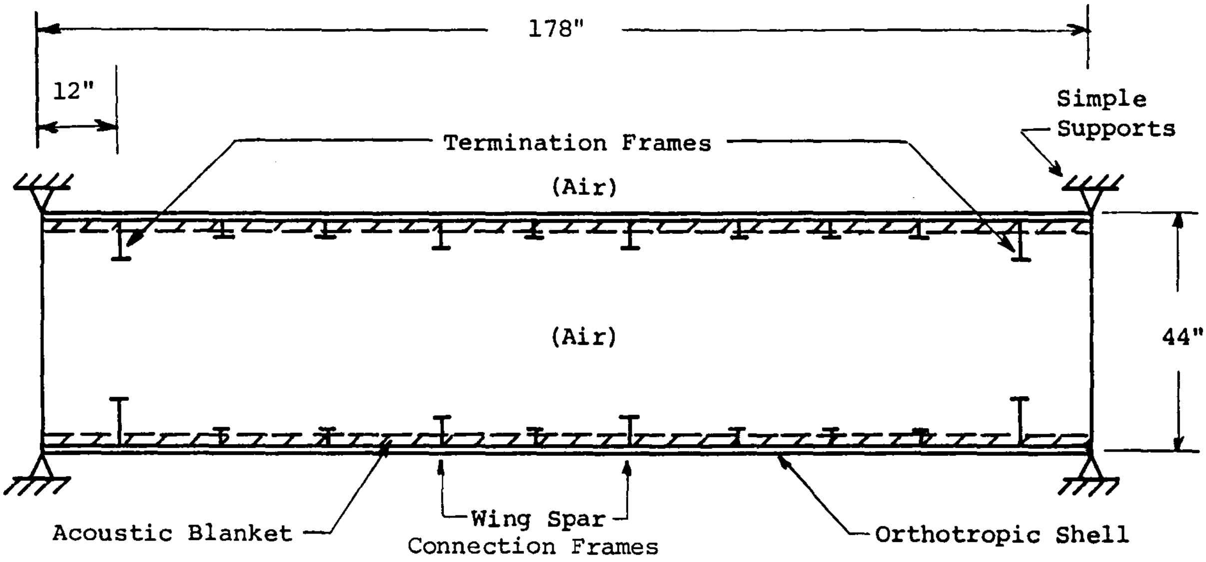

Fig. II.4 Cylindrical shell representation of fuselage and cabin space.

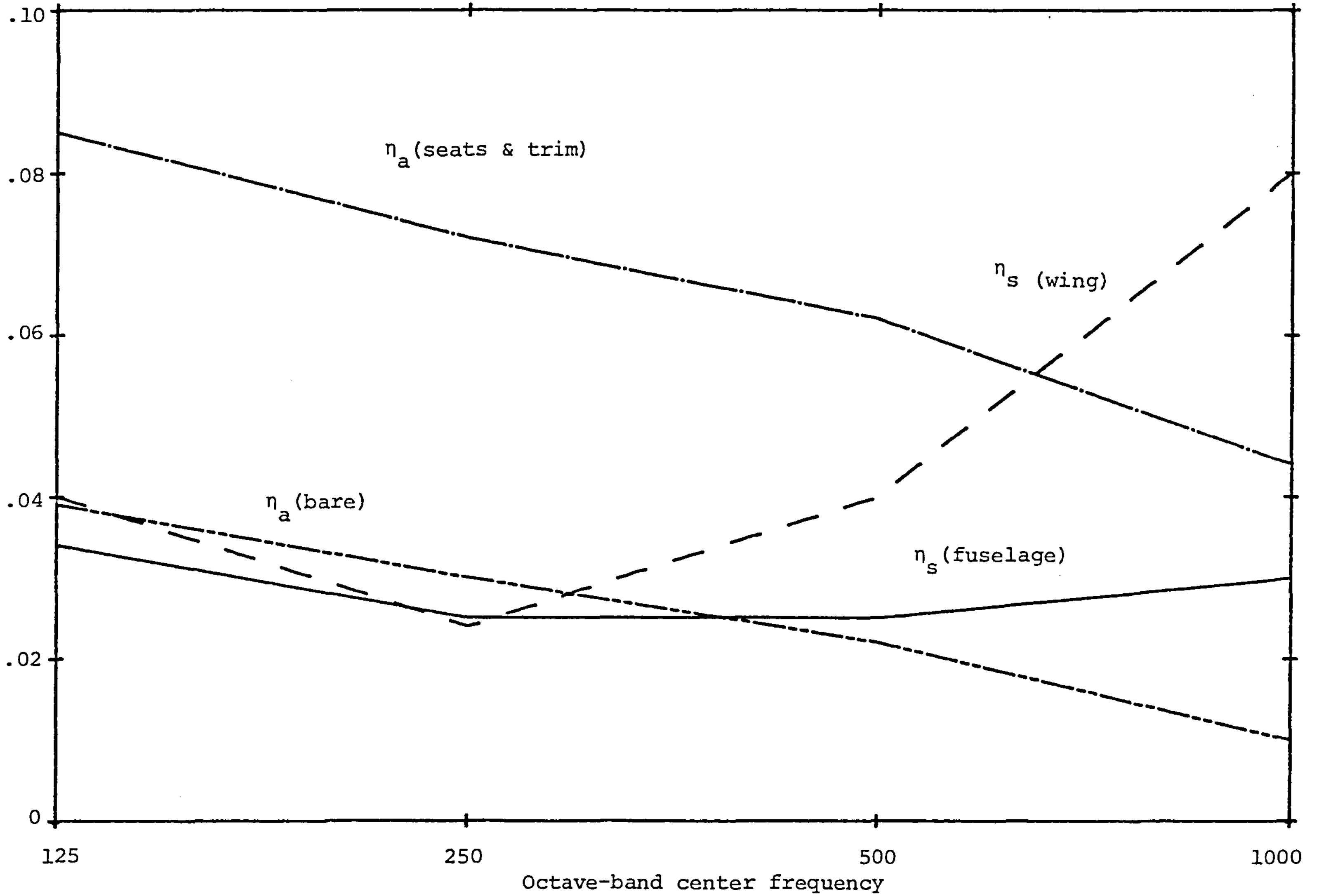

Fig. II.5 Measured structural (η_s) and acoustic (η_a) loss factors on Baron fuselage and wing. (Ref. 2)

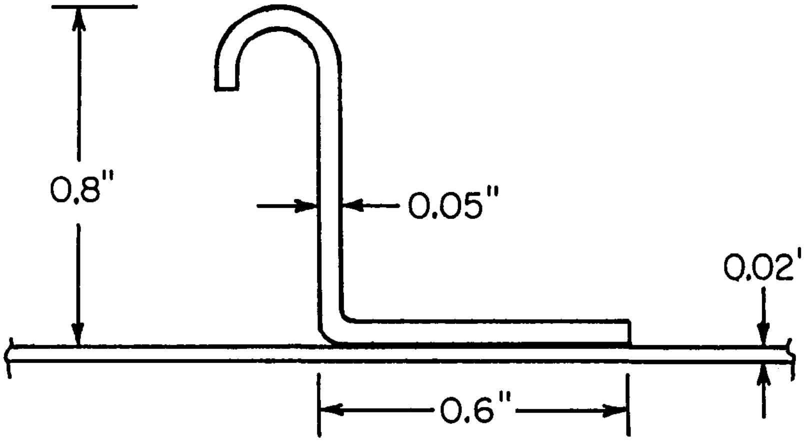

Fig. II.6 Geometry of axial stringers on fuselage skin showing approximate dimensions.

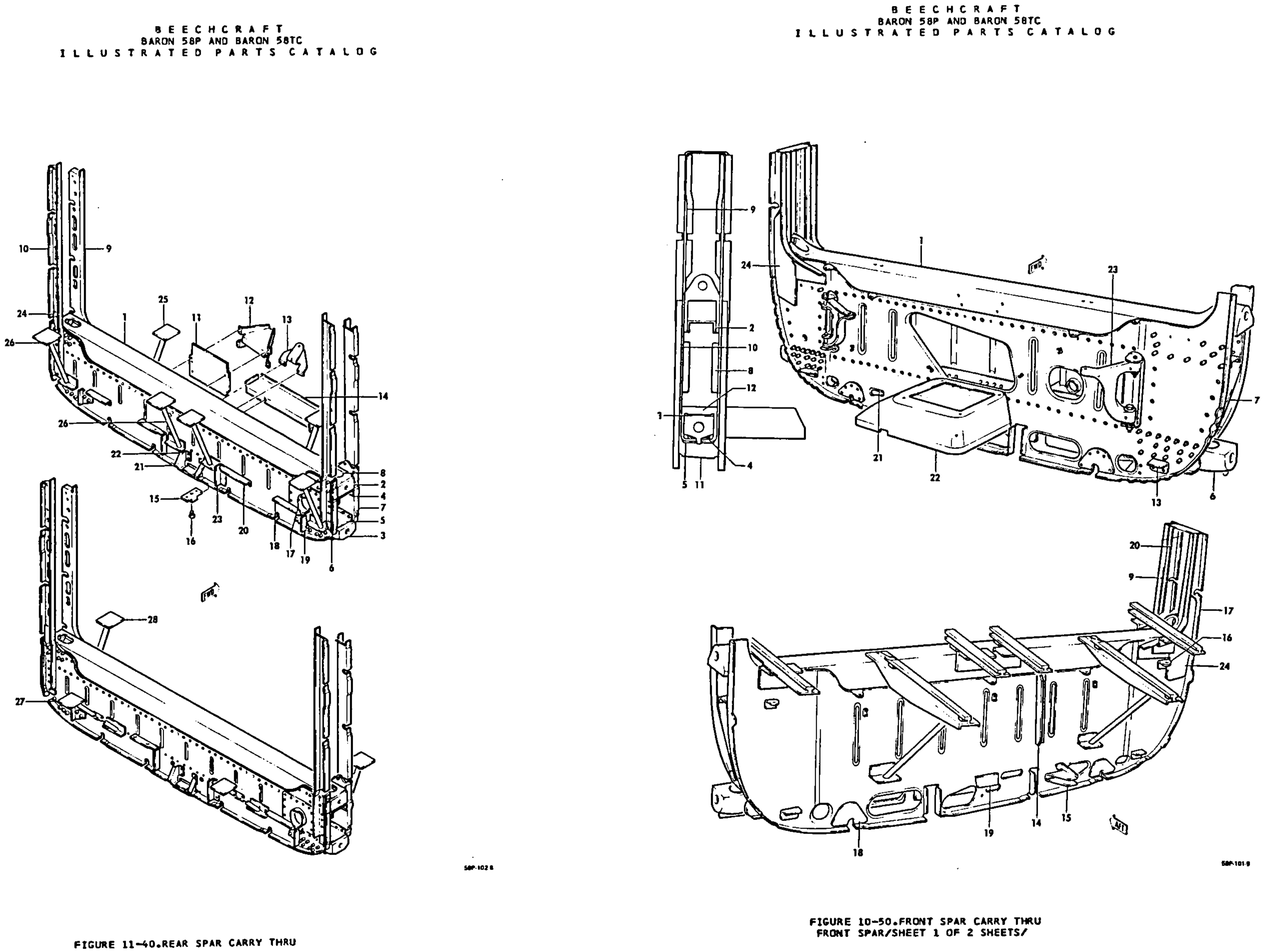
BEECHCRAFT
BARON 58P AND BARON 58TC
ILLUSTRATED PARTS CATALOG

BEECHCRAFT
BARON 58P AND BARON 58TC
ILLUSTRATED PARTS CATALOG

FIGURE 11-40.REAR SPAR CARRY THRU

(a)

FIGURE 10-50.FRONT SPAR CARRY THRU
FRONT SPAR/SHEET 1 OF 2 SHEETS/

(b)

Fig. II.7 Aft (a) and forward (b) fuselage spar carry-through structures (from Ref. 4).

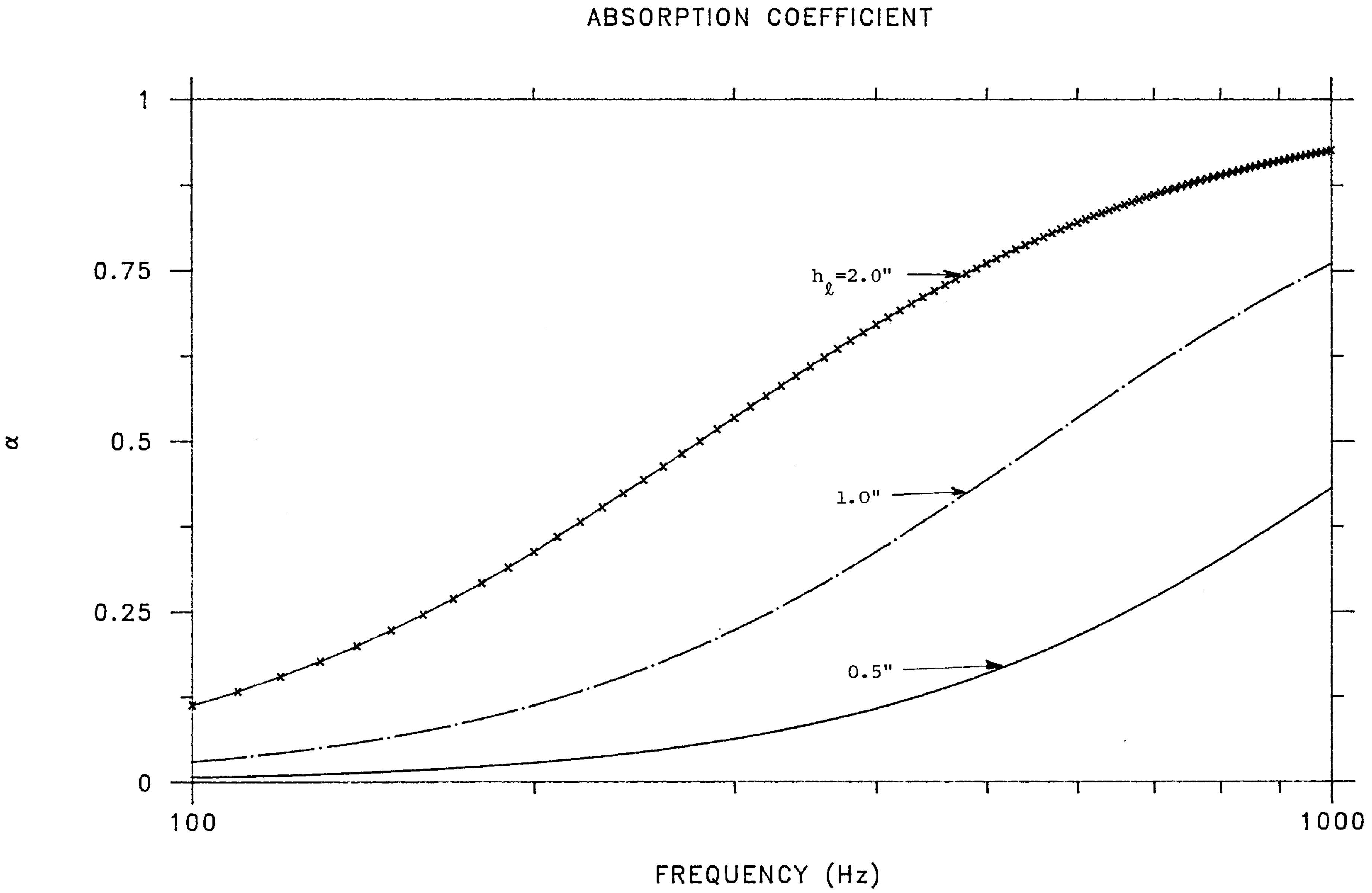

Fig.II.8 Normal incidence absorption coefficient for the rigidly backed acoustic liner as a function of frequency and thickness ($\sigma_\ell=5.5 \times 10^{-3}$ lbf-s/in^4, $\rho_\ell=1.1 \times 10^{-6}$ lbf-s^2/in^4).

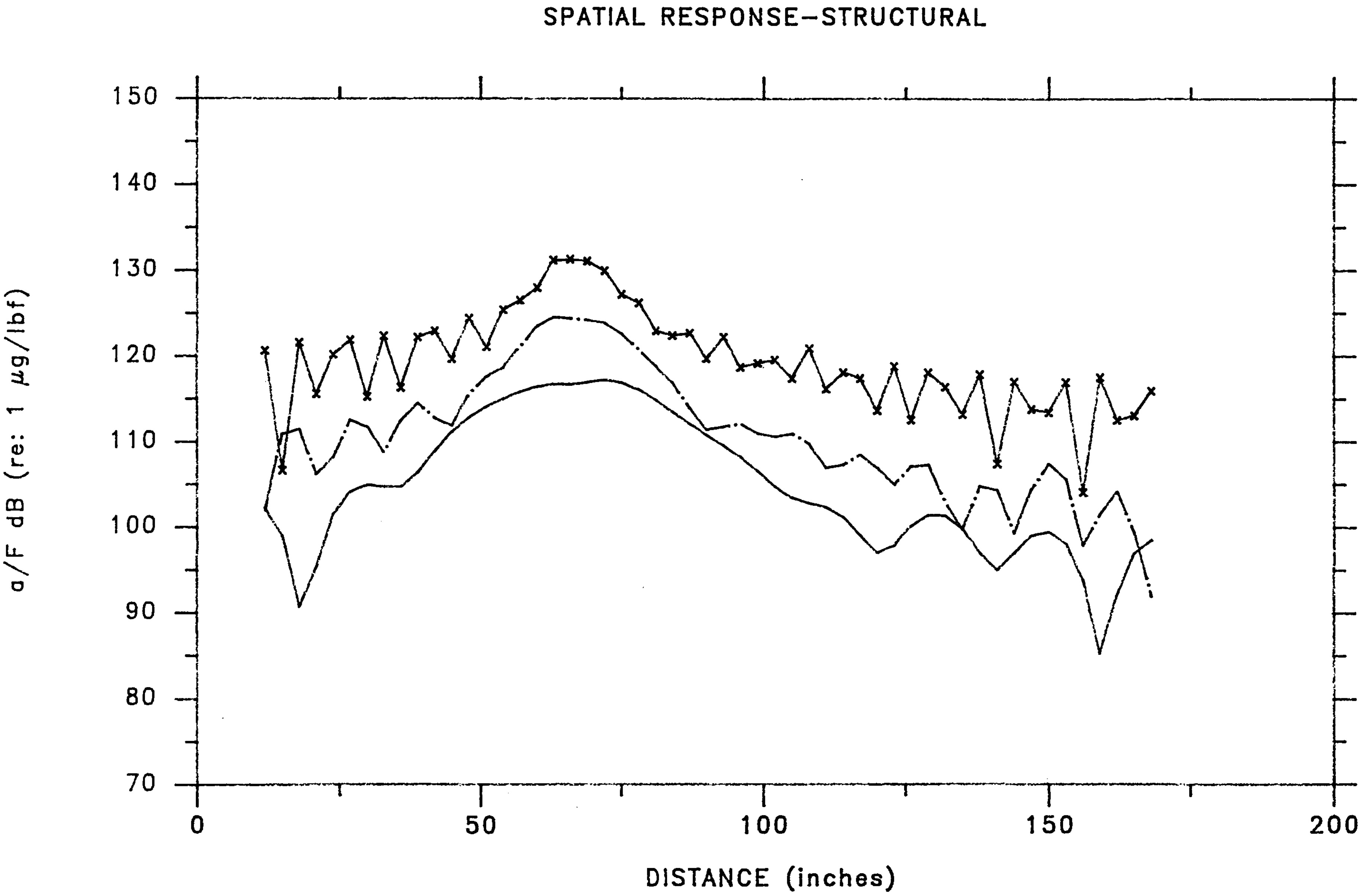

Fig. II.9 Spatial variation for the damped unframed configuration of radial acceleration along the shell generator containing the radial excitation force. (125 Hz, ——; 250 Hz, —·—; 500 Hz, —X—X—).

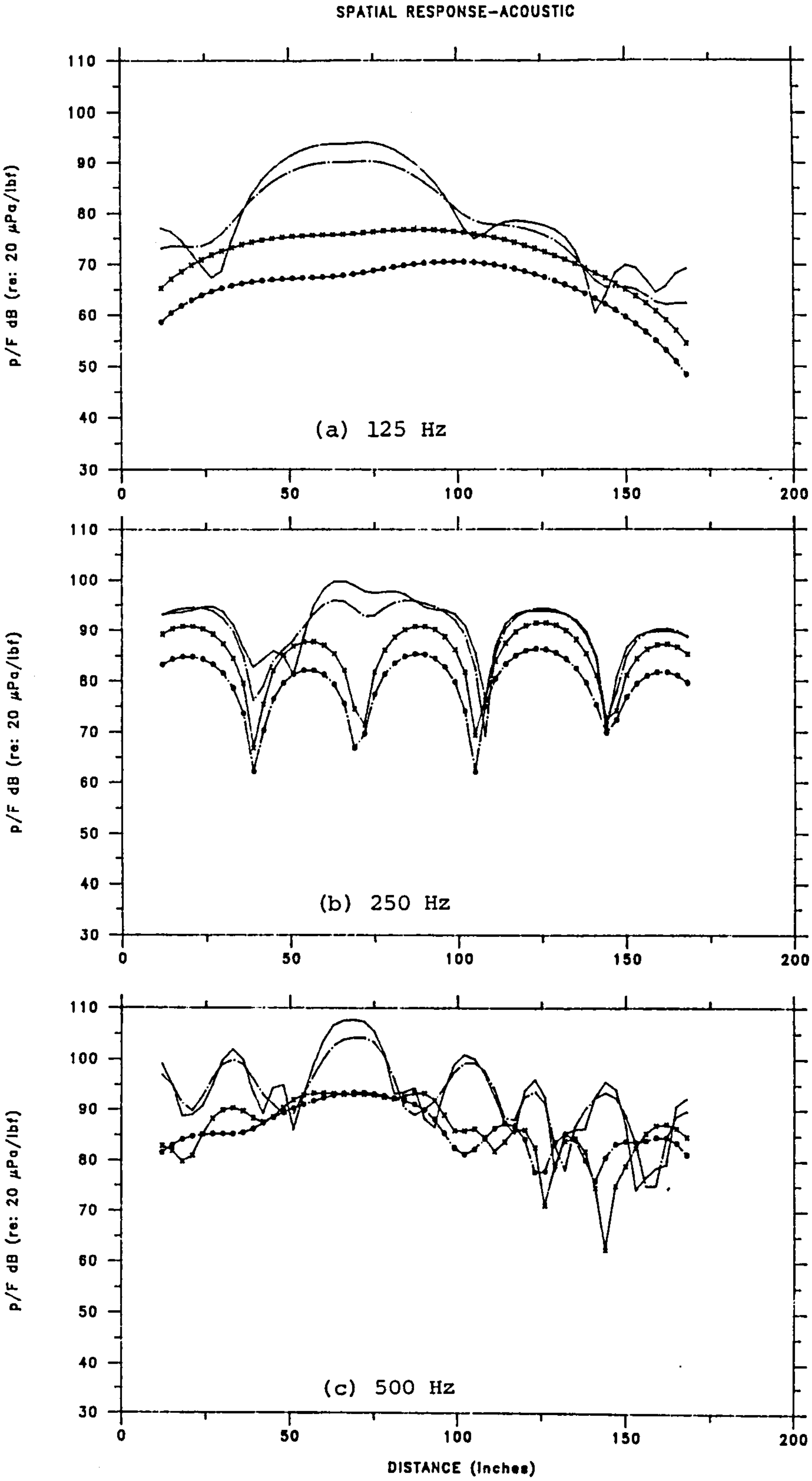

Fig. II.10 Spatial variation for the damped unframed configuration of cabin pressure along the shell generator containing the radial excitation force. (radius=22" (—), 20" (—·—), 10"(—X—X—), 5" (—●—●—)).

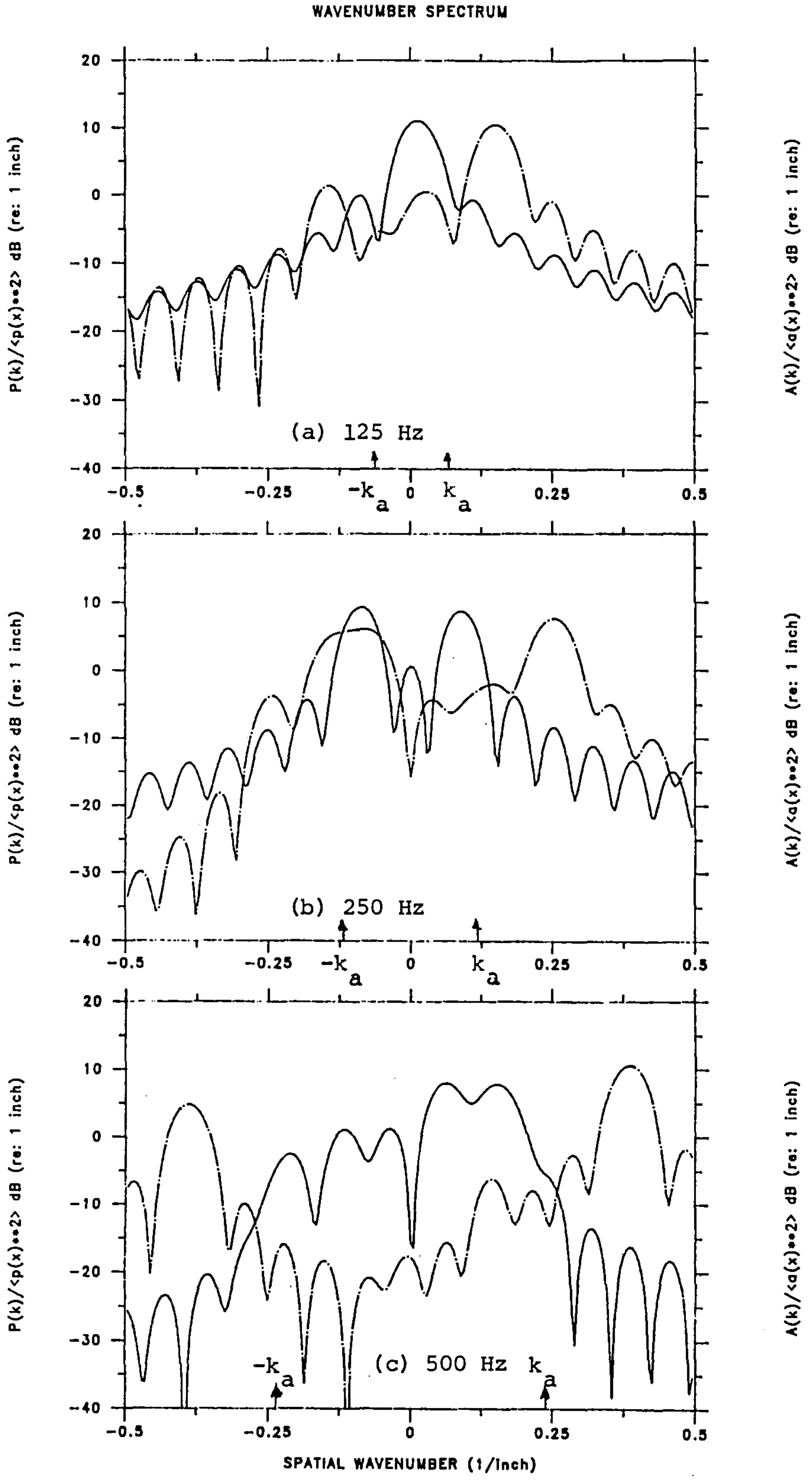

Fig. II.11 Normalized wavenumber spectra for the damped unframed configuration of cabin pressure (———) at a radius of 10" and radial wall acceleration (—·—) along the shell generator containing the radial excitation force. (spatial aperture: 75" ≤ x ≤ 165").

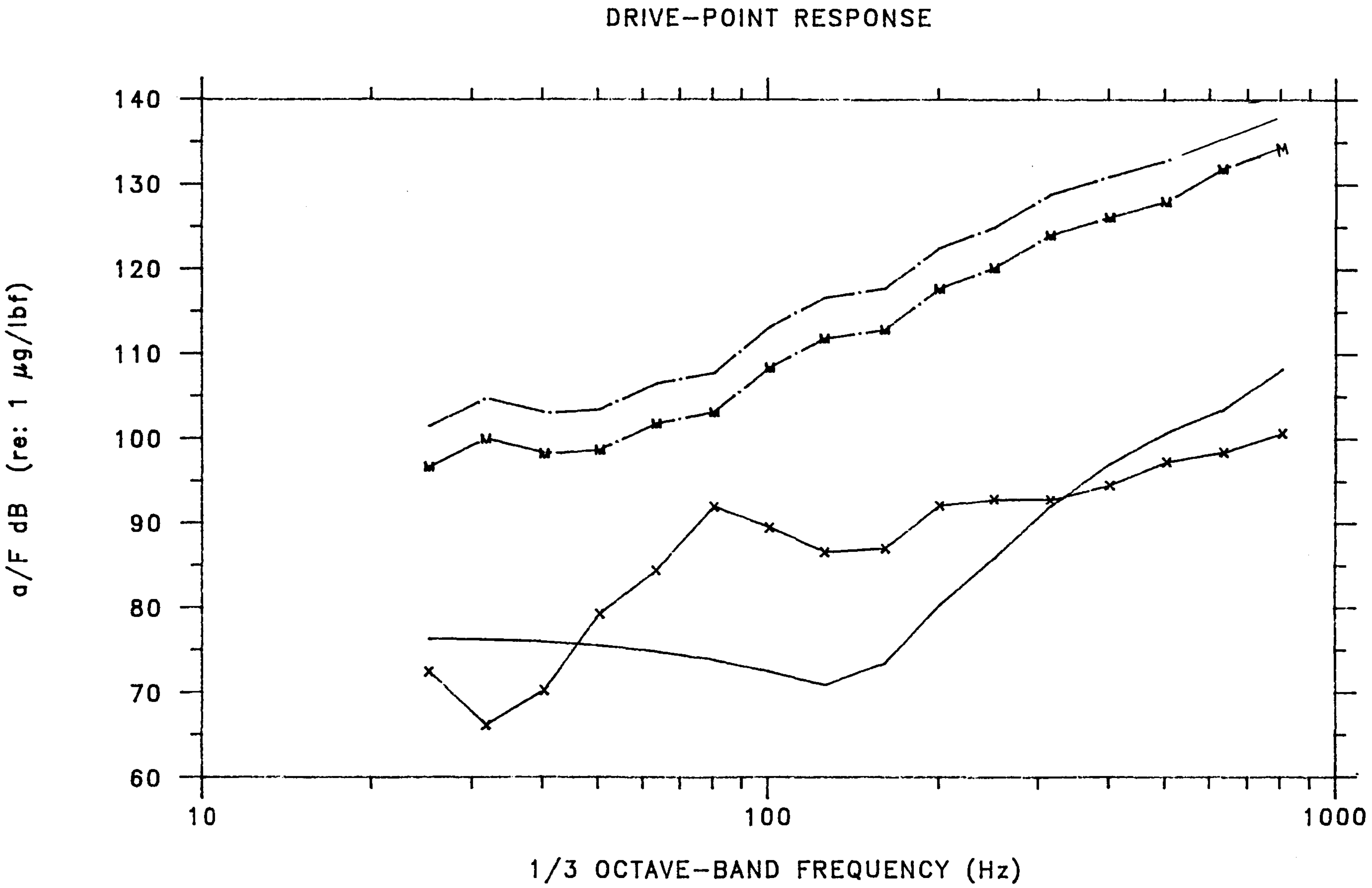

Fig. II.12 Calculated drive-point accelerance for the heavily damped unframed configuration at the bolt location in the radial (—·—), thrust (——), and circumferential (—X—X—) directions. (RMS accelerance, ——·—M—).

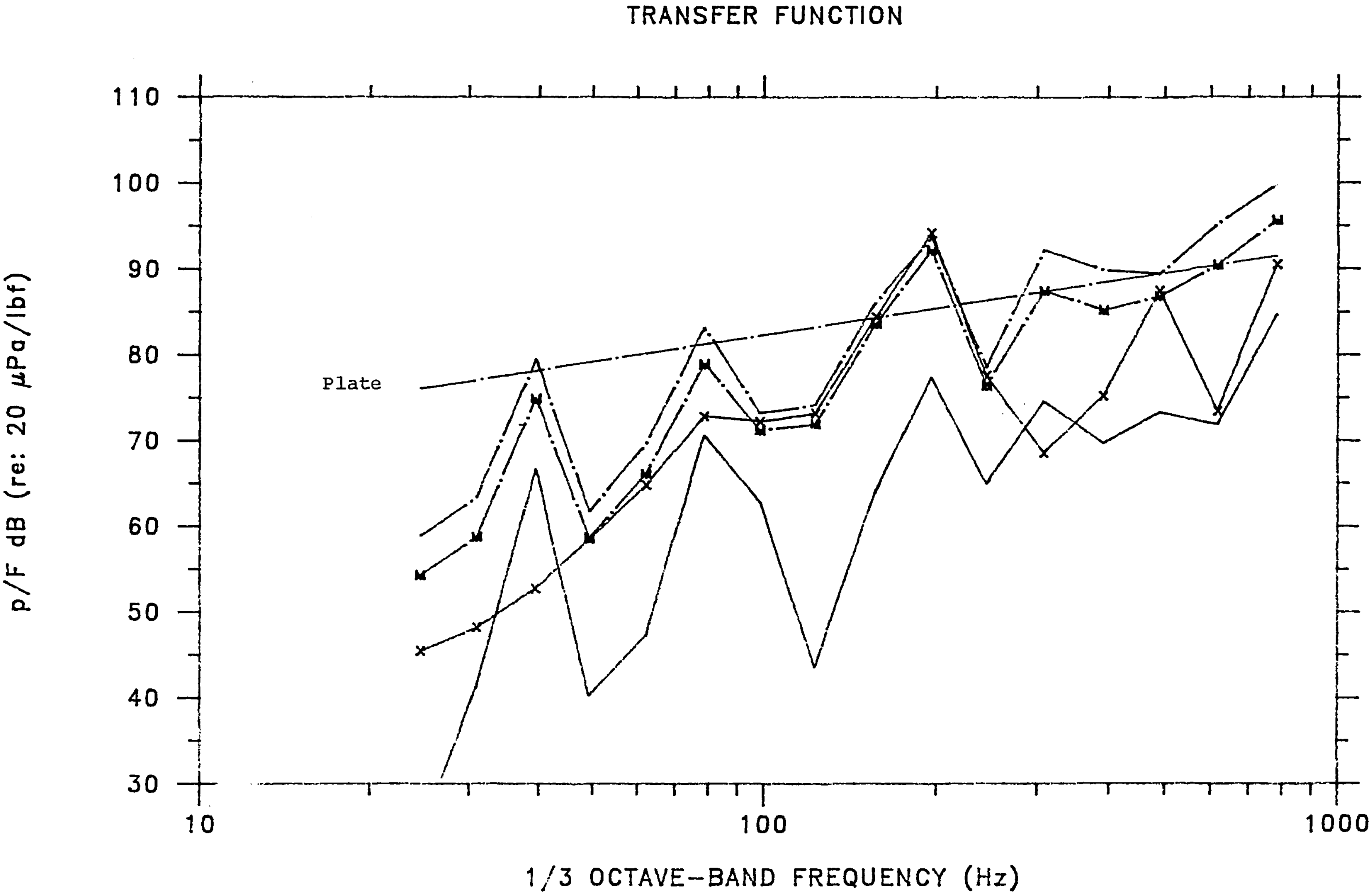

Fig. II.13 Calculated pressure for the heavily damped unframed configuration at cabin location 1 per excitation force at the bolt location in the thrust (——), radial (——·——), and circumferential (——X——) directions. (RMS transfer function, ——·–M–).

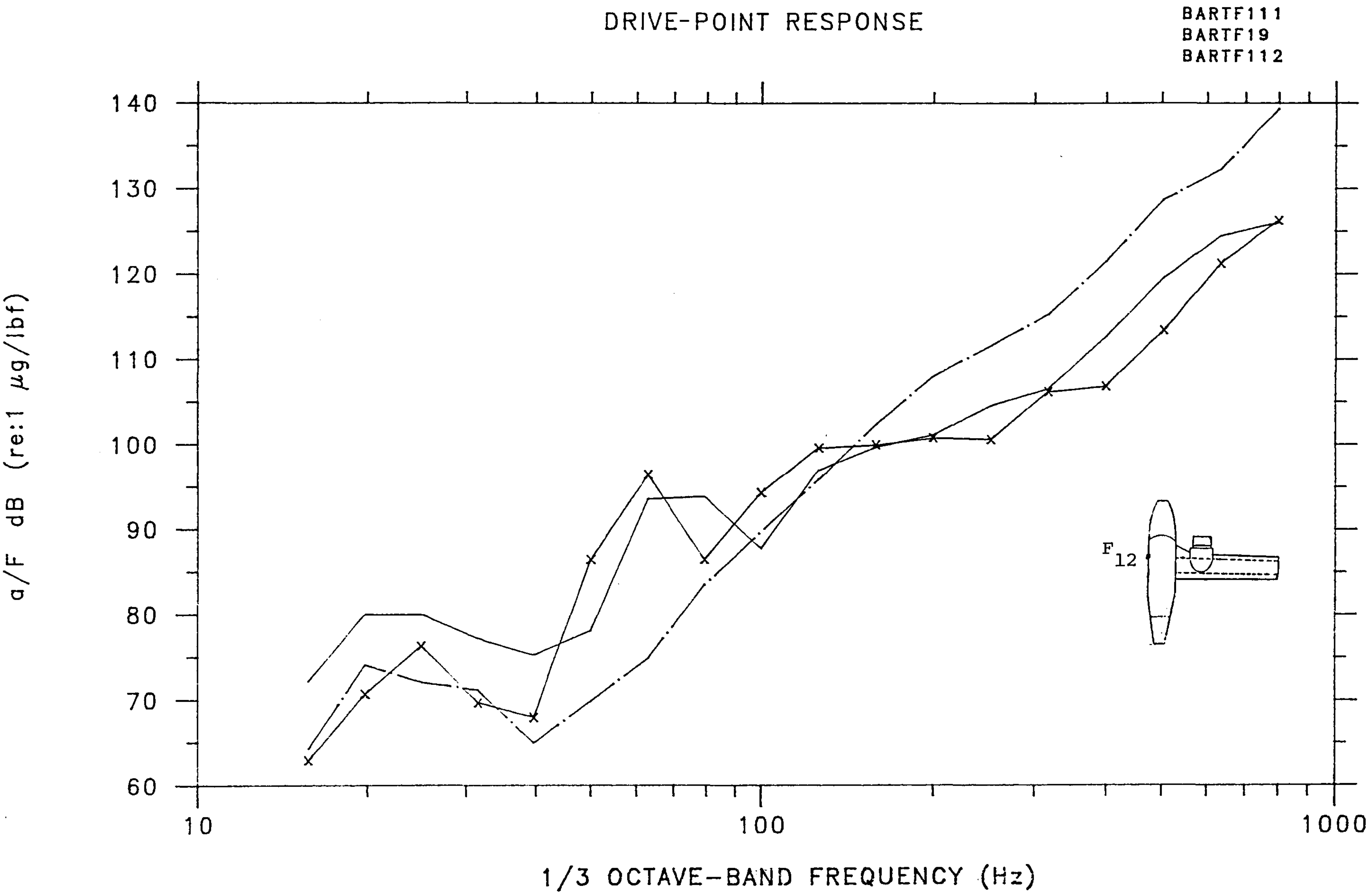

Fig. II.14a Measured drive point accelerance at fuselage location 12 in the spanwise (X—X—), thrust (—·—) and lift (——) directions.

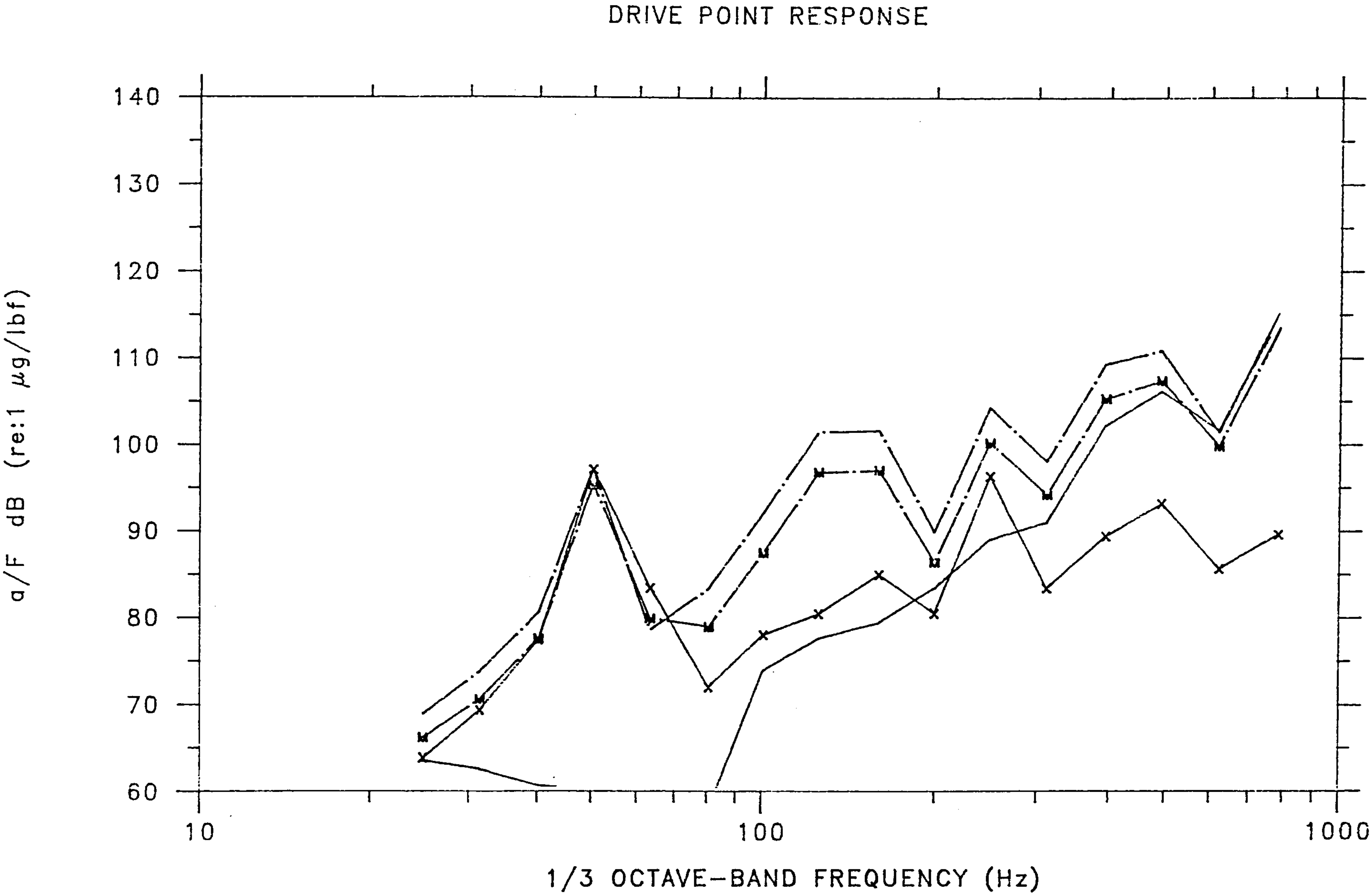

Fig. II.14b Calculated drive-point accelerance for the baseline configuration at the bolt location in the radial (—·—), thrust (—), and circumferential (—X—) directions (RMS accelerance, ——·—M—).

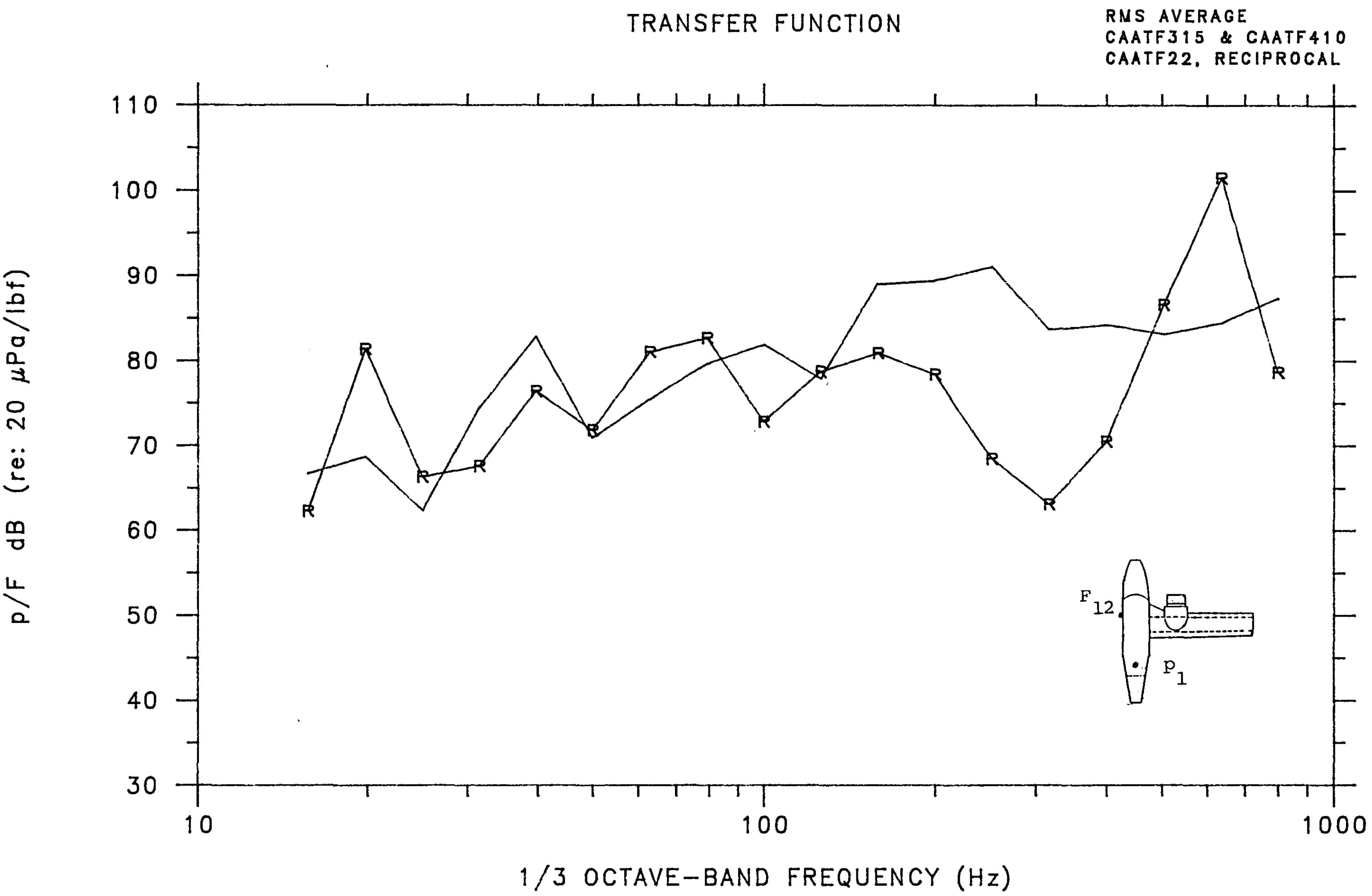

Fig. II.15a Measured pressure at cabin location 1 per spanwise excitation force at the bolt location. (Measurement using direct (——), and reciprocal (—R—) test methods (Ref. 2)).

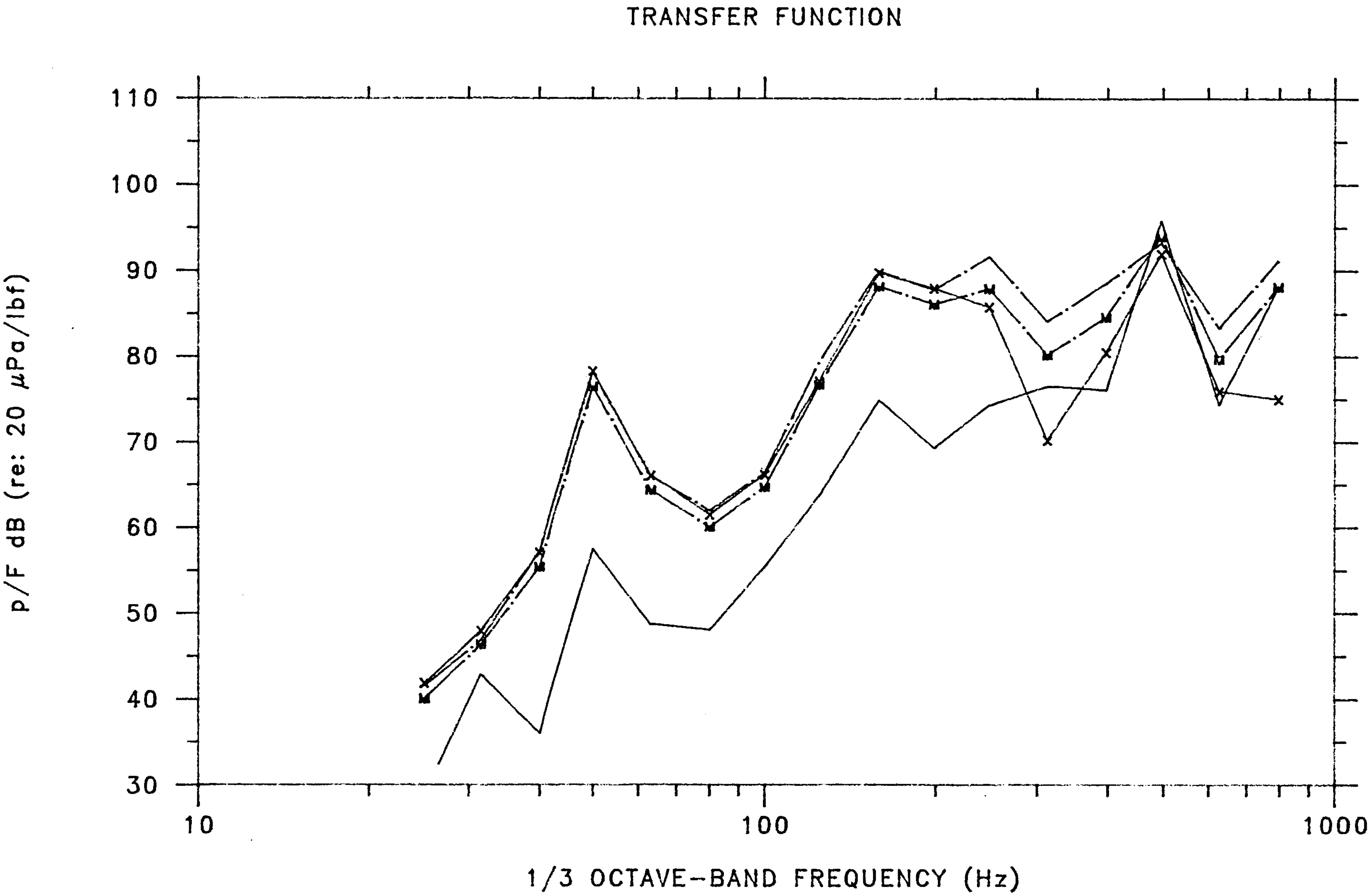

Fig. II.15b Calculated pressure for the baseline configuration at cabin location 1 per spanwise excitation force at the bolt location in the thrust (——), radial (—·—), and circumferential (—X—) directions. (RMS transfer function —·—M—).

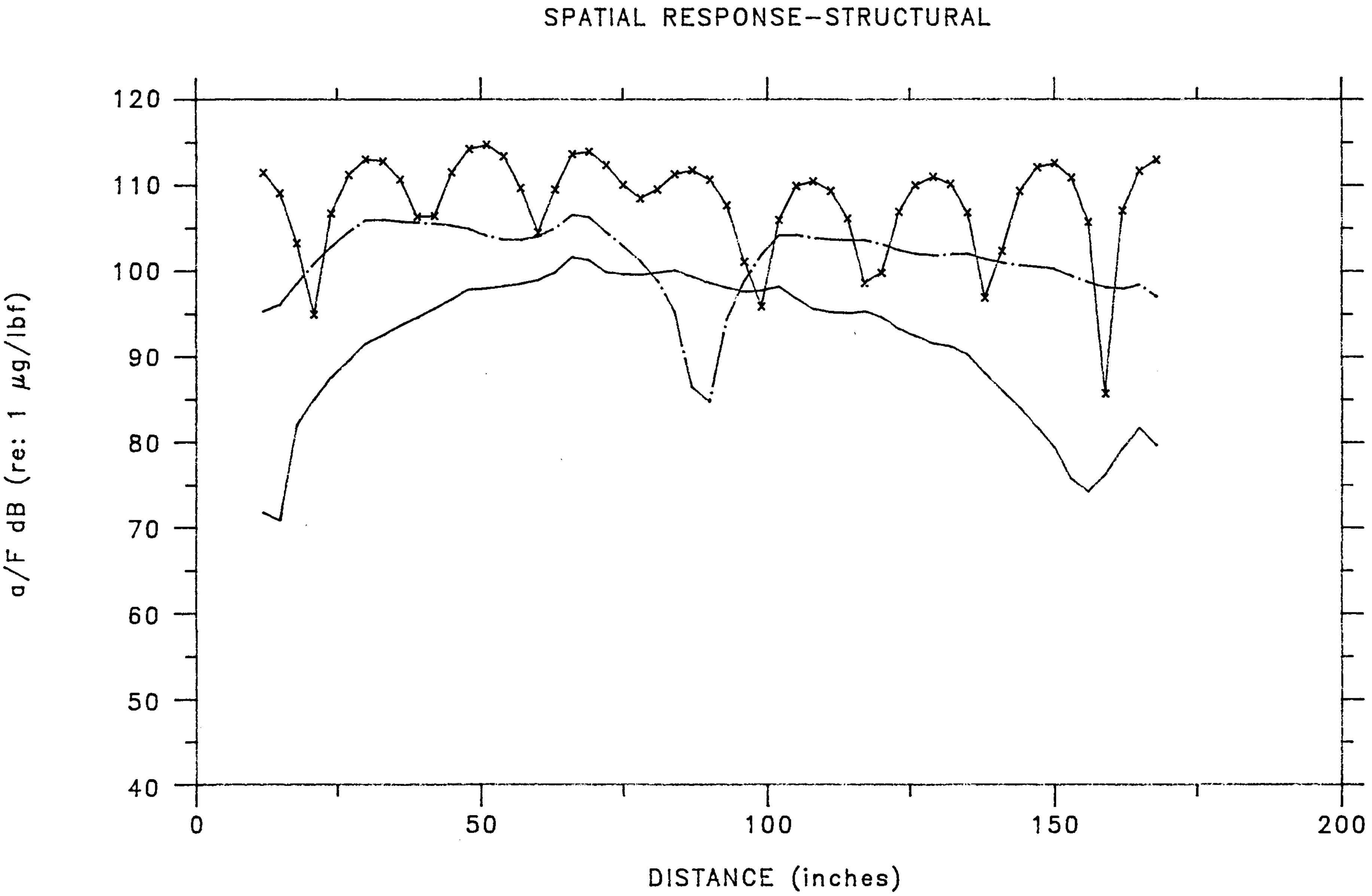

Fig. II.16 Spatial variation for the baseline configuration of radial acceleration along the shell generator containing the radial excitation force (125 Hz, ——; 250 Hz, —·—; and 500 Hz, —X—X—).

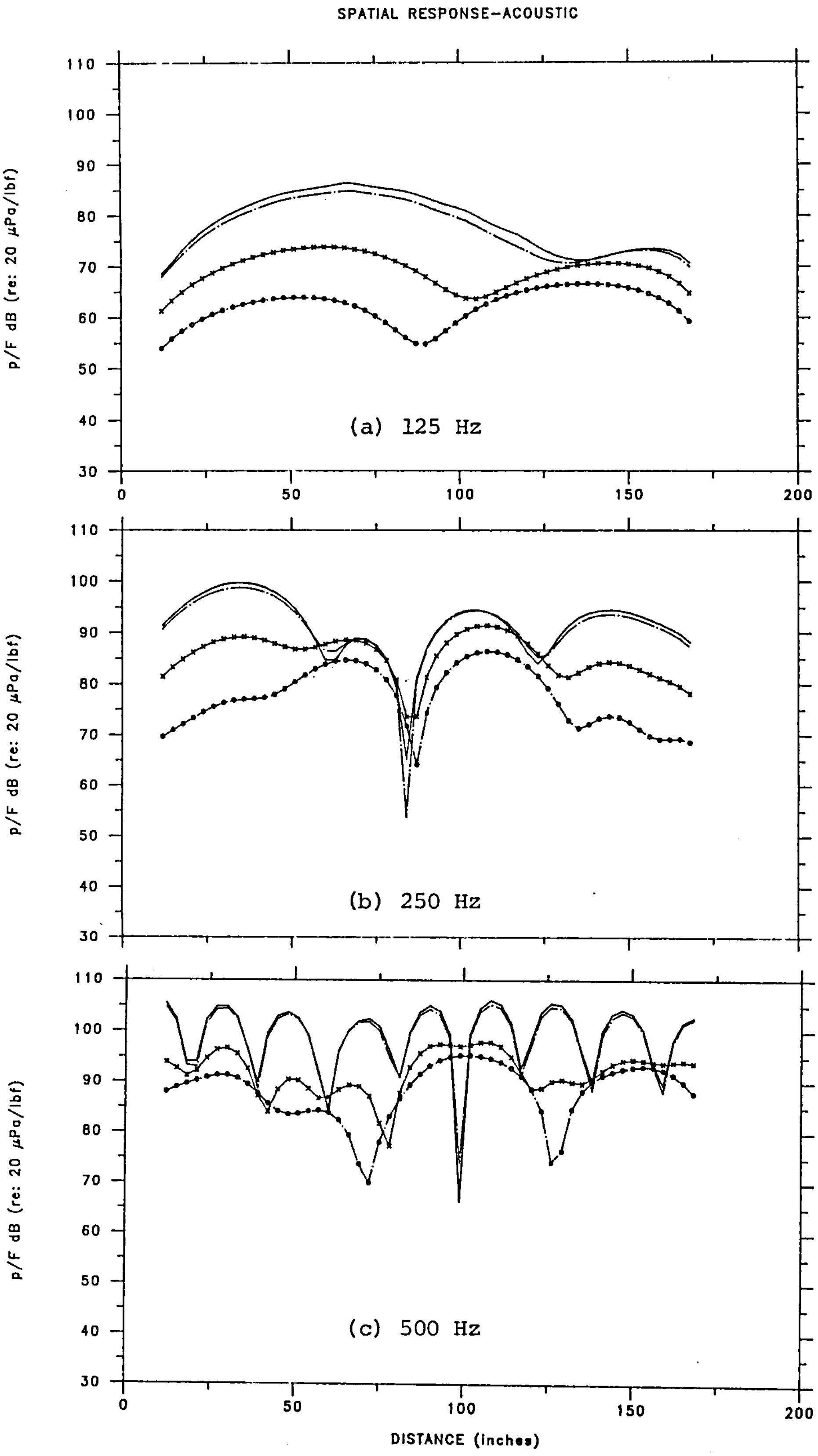

Fig. II.17 Spatial variation for the baseline configuration of cabin pressure along the shell generator containing the radial excitation force. (radius=22" (—), 20" (—·—), 10" (–X—X–), 5" (—●—●—)).

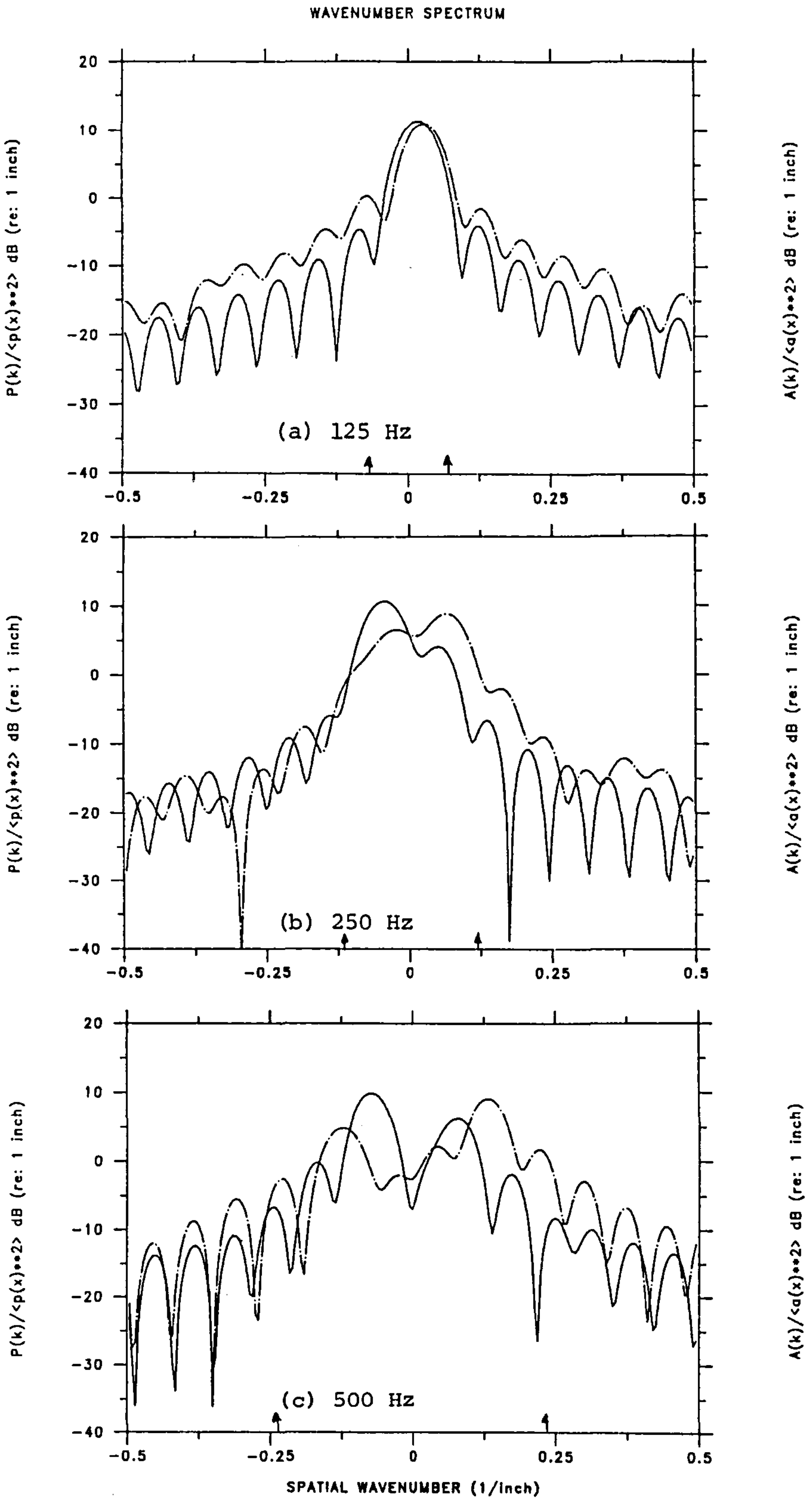

Fig. II.18 Normalized wavenumber spectra for the baseline configuration of cabin pressure (———) at a radius of 10" and radial wall acceleration (—·—) along the shell generator containing the radial excitation force (spatial aperture: 75" $\le$ x $\le$ 165").

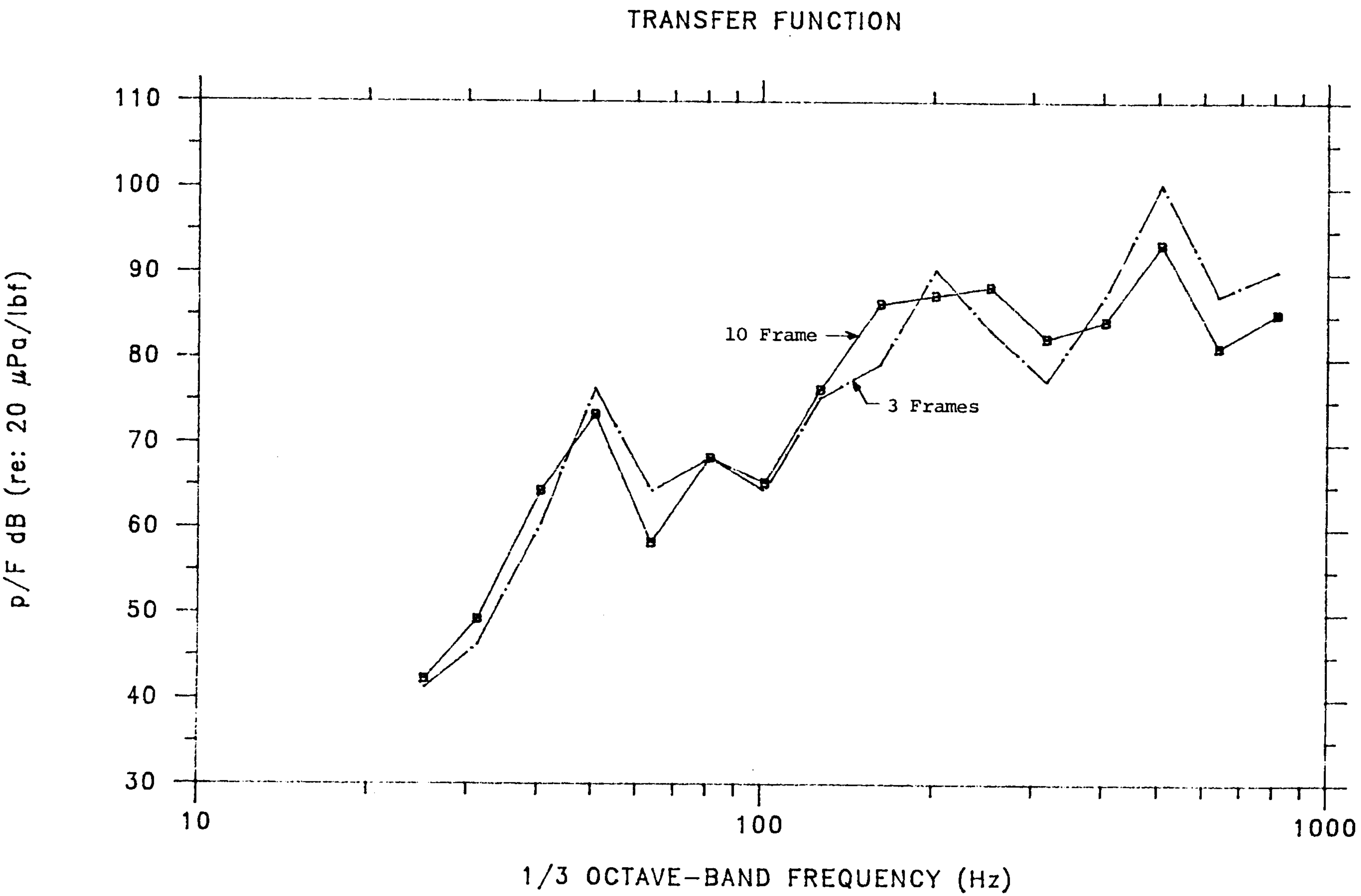

Fig. II.19 RMS average over excitation direction of the one-third octave-band pressure at cabin location 1 per force at the bolt location. (Baseline configuration, —B—; configuration having frames at drive and ends only, —·—).

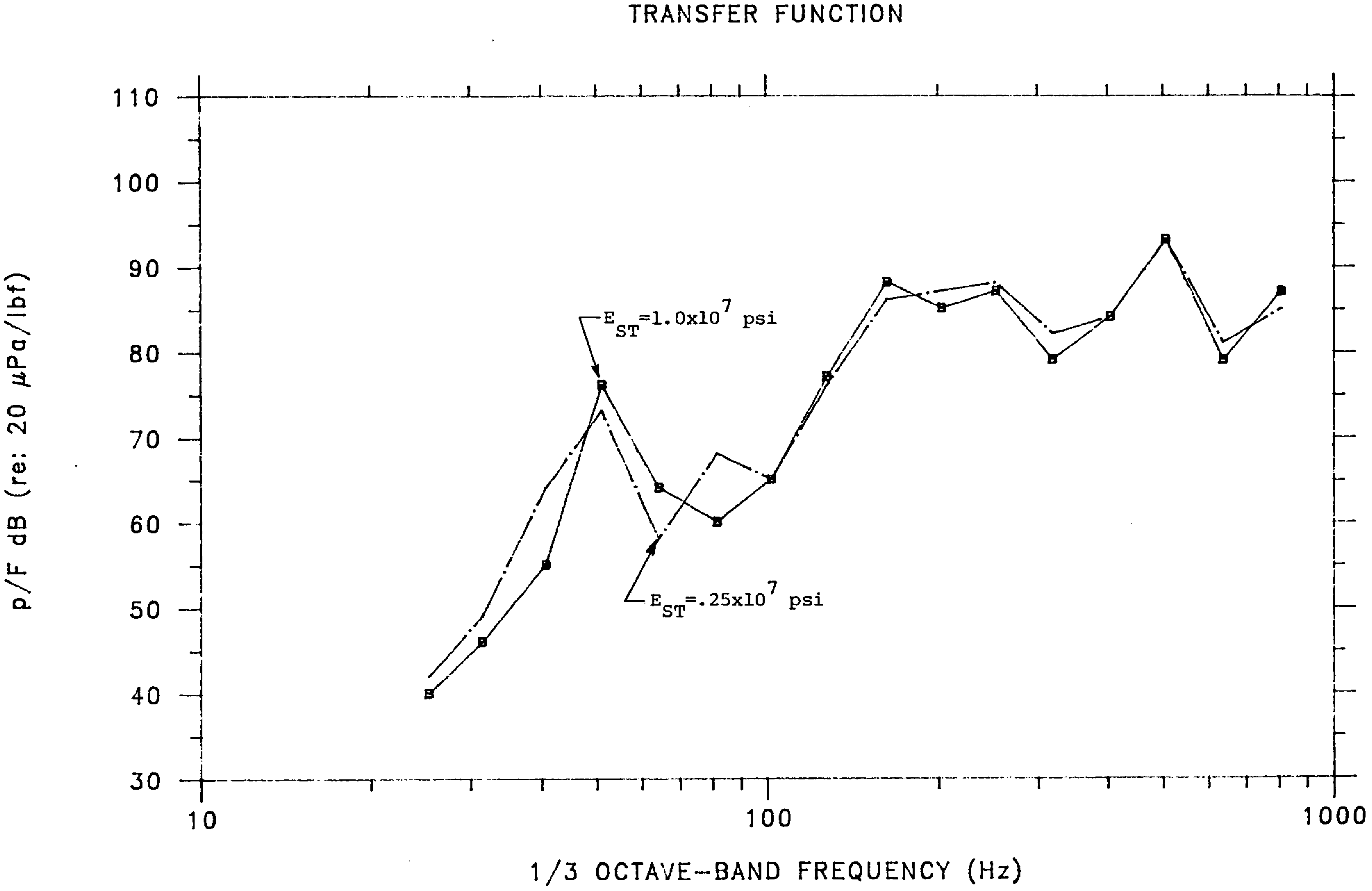

Fig. II.20 RMS average over excitation direction of the one-third octave-band pressure at cabin location 1 per force at the bolt location. (Baseline configuration, —B—; configuration having stringer stiffness reduced by factor of 4, —·—).

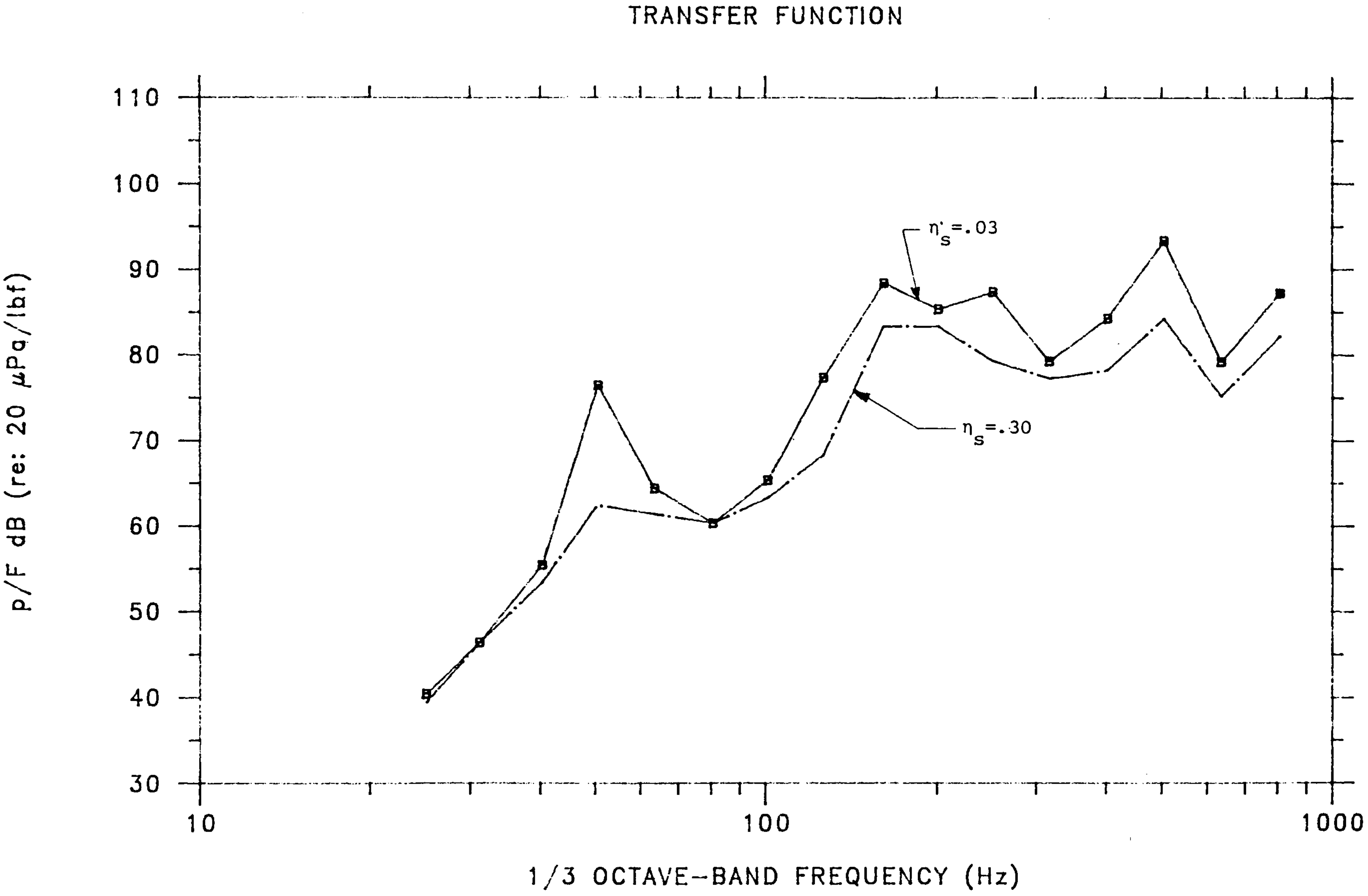

Fig. II.21 RMS average over excitation direction of the one-third octave-band pressure at cabin location 1 per force at the bolt location. (Baseline configuration, —B—; configuration having structural loss factor increased by factor of 10, —·—).

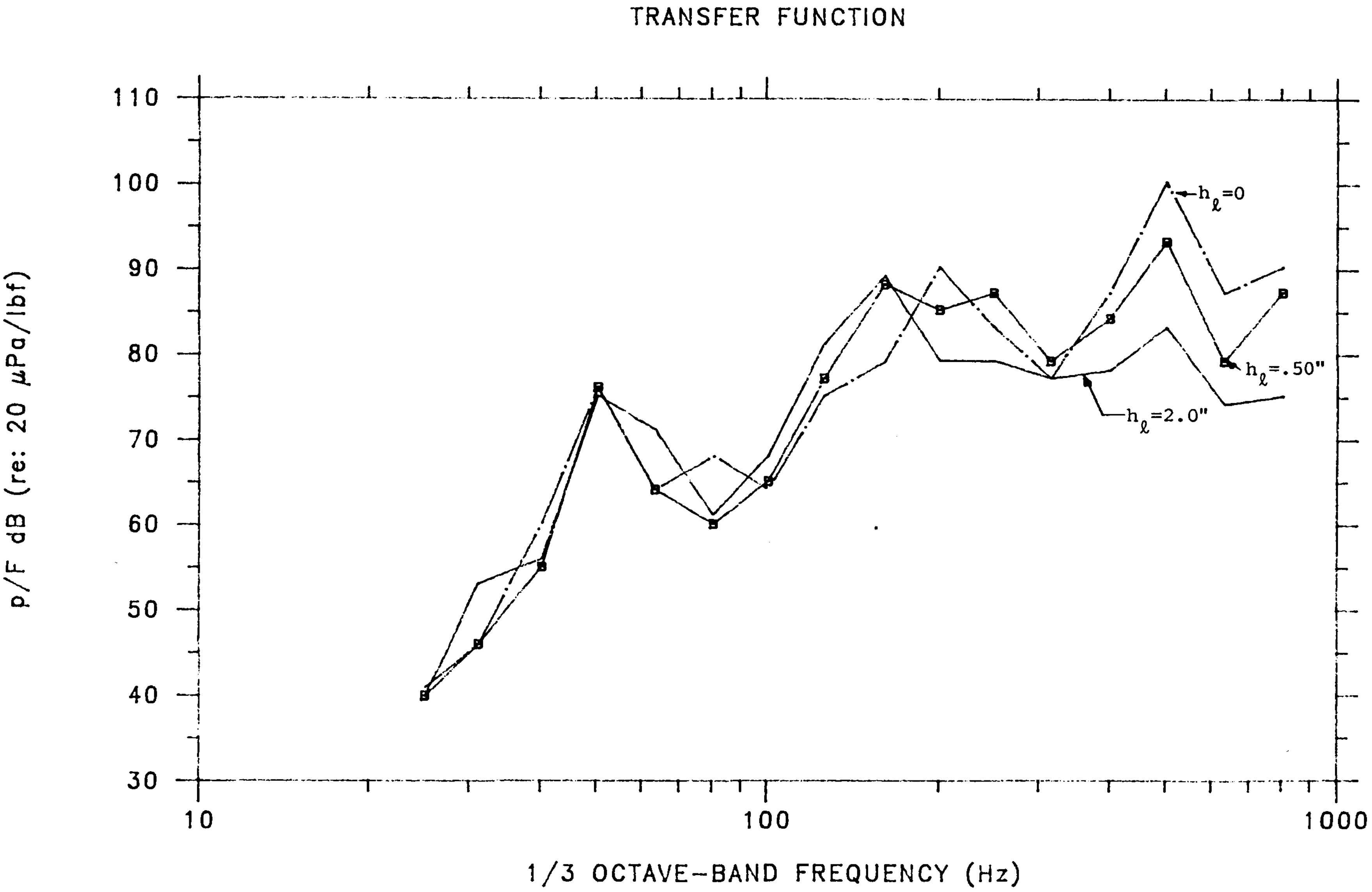

Fig. II.22 RMS average over excitation direction of the one-third octave-band pressure at cabin location 1 per force at the bolt location. (Baseline configuration, —B—; configuration having no acoustic liner, —·—, configuration having a 2 inch thick acoustic liner, ——).

III. MODEL OF WING DYNAMICS

A. Introduction

The wing of the Beechcraft Baron is a riveted structure consisting of 2 main spars running spanwise, ribs providing chordwise stiffness, and external skins with attached stringers for spanwise stiffening. The stiffeners vary from wing tip to root in dimensions and spacing. Internal to the wing are fuel tanks and fuel lines. In the operational wing, flaps are connected along the trailing edge. The engine is supported on a frame connected to the wing at a highly stiffened portion of the structure. The experimentally tested wing is incomplete and somewhat damaged (see Ref.2), and neither engines nor wing flaps are present in the test structure. The damage is in the form of patches of wrinkled skin and loose rivets. The total weight of the test wing is 220 pounds.

To aid investigating the structure-borne noise path, the Beechcraft Baron wing has been modeled using finite elements. Attempts to compare with the experimentally-found fundamental modes and frequency-responses motivated a series of models, ranging from a simple cantilever beam to a 1,200 node, three-dimensional model comprised of skin, stringers, ribs, and spars. Parameter studies of these models have provided insight into the importance of structural elements of the wing to the transfer of propeller force to the fuselage. For frequencies below 200 Hz,. the models act to predict wing response under a variety of loading conditions such as distributed unsteady pressures from the propeller and localized excitation.

B. Modelling Approach

The general-purpose finite element program NASTRAN, distributed by NASA's Computer Software Management and Information Center (COSMIC), is used in this study. Two COSMIC NASTRAN elements define the model's dynamic matrices. The BAR element, containing six degrees of freedom at each of its two nodes, appears throughout the series of models. This element represents bending, shear, torsion, and compression. In the three-dimensional detailed models, the plate bending element QUAD4 combines with the membrane element QDMEM1 to treat shear, compression, and flexure of the skin, spars, and ribs.

Both are 4-node elements which use a linear interpolation scheme to approximate the uncoupled bending and shear differential equations of a plate. In terms of performance of these elements the shear element presents the greatest probable source of error. Although shear can vary between nodes, COSMIC error analysis (Ref. 8) indicates that the element tends to be too stiff in shear.

For all forced responses used to compare the model with experiment, the frequency interval is 2 Hz. The forced responses taken below 200 Hz are calculated from an expansion of modes from 0 to approximately 350 Hz. To account for damping in the structure, the finite element scheme applies a modal damping factor varying from .04 at 1 Hz to .06 at 200 Hz, these values being based on experimental results presented in Ref. 2. The measured drive-point admittance in the lift direction at a bolt location on the forward spar of the freely-supported wing is shown on Fig. III.1. A number of resonances below 200 Hz are found, and these frequencies along with their associated mode shapes are used for comparison with the wing models discussed below. Locations of the measured and calculated responses are shown on Fig. III.2.

C. Results

1. Beam Models

Transfer and drive point responses measured on the wing with effectively free boundary conditions determined the cross-sectional properties for the first finite element model, a cantilevered beam. The frequencies of the first in-plane and out-of-plane bending modes, torsional mode, and span-wise compressional mode, shown in Table III.1, were used as input into fundamental free-free beam equations (e.g., Ref. 9) to calculate the corresponding properties. Compared to measurements, drive-point accelerance at the main spar mount bolts and a transfer mobility from the bolt to an outboard point on the main spar displayed discrepancies in both level and resonance frequencies above the fundamental mode.

In an attempt to bridge these differences, a multi-beam ladder model using exclusively NASTRAN bar elements and including both spars and ribs followed (see Fig. III.3). The initial parameter estimation of each beam was made by lumping statically an adjacent portion of the skin to each member to find the area, bending stiffness, and torsional stiffness for each bar element. Maintenance of the mass and the experimentally-found bending stiffnesses determined the amount of skin to be included along each beam for static calculation of the section properties. The torsional stiffness of each beam, however, did not lend itself to such simple computations, as the skin and the spars form a "torsion box" which relies upon the skin to carry shear. Initially, the torsion-box stiffness was concentrated into the spars of the ladder-like model by a crude distribution of the section's torsion constant, which was calculated from the cross-sectional geometry of an average section of the wing by approximate methods. With a series of finite-element eigenvector extractions, these member constants were fitted to match the frequency of the first bending mode found experimentally. The first 4 mode shapes (Fig. III.4a) from the fitted-parameter model, when compared to the first 6 experimentally-found modes (Fig. III.4b) show strong similarities. The first two modes of both sets match well in both frequency and shape. The third and fourth calculated mode shapes are identical to the fifth and sixth measured mode shapes, although the model frequencies are about 15 Hz higher. Two measured modes at 68 and 74 Hz, however, are not seen in the finite element results. Since this beam model neglects all plate and panel modes in its lumped-parameter formulation, discrepancies would be expected near and above frequencies where the plate-like elements of the structure (e.g., webs of ribs, skin panels) become resonant.

2. Plate Model Development

Inclusion of the plate-like resonances suggested another refinement to the model. Because the natural frequencies of the first plate modes of the webs of the spar are expected to be lowest near the fuselage where the airfoil is thickest, and therefore of greatest concern to this low-frequency analysis, the first two bays of the wing were modelled in detail using both plate and beam elements. The model of the two bays includes skin, stringers, ribs, and spars; the remainder is identical to the previously described multi-beam ladder model. The model, shown in Fig. III.5, produced a mount bolt drive point response, more representative of the measurements above 100 Hz than the ladder model. The calculated transfer response, however, reflects no marked improvement over the previous model. The two measured modes at 68 and 74 Hz, missing in the ladder model, were not captured by the plate elements in the two bays.

The effort to improve the model below 100 Hz resulted in two increasingly complex finite element representations. Using plate elements for the entire wing, the first model imposed symmetry about the top and bottom surfaces of the airfoil. All members of the model varied in thickness or cross section according to data taken from a methodical measurement of the wing. This modelling scheme rendered lumped-parameter estimation of member parameters unnecessary. The 3500 degree-of-freedom model, took advantage of symmetry to reduce computational costs. The resulting modal frequencies, (see Table III.2, entry III.A) imply no clear advantage over the more simple models. The composition of this model, however, facilitates isolation of the various components, including the skin and the spars.

A number of parameter studies were performed on the model to determine its sensitivity to changes in various parts of the structure. The goal of the study, in addition to determining reasons for the model missing modes, was to gain insight into which wing components principally control the modes, and therefore the vibration transmitted structurally to the fuselage. Changes in the model were made to investigate a variety of effects: the skin thickness, localized ineffectiveness of skin in areas observed to be wrinkled (i.e., damaged), mass differences, the connections between ribs, spars, and skin, and the engine mount. Table III.2 presents a summary of the parameter changes. Each model displayed a like set of four low frequency mode shapes; namely, out-of-plane bending, torsion, a second out-of-plane bending, and a composite bending-torsion mode, diagrammed in Fig. III.4a. The frequencies associated with these shapes for each model, included in Table III.2, are used to judge sensitivity to the particular change.

Although none of the changes resulted in analytical modes having frequencies and shapes similar to the measured modes at 68 and 74 Hz, a number of conclusions can be drawn from this study. The addition of approximately 20 pounds of stiffened structure for the engine mount, minimally influenced the modal frequencies (Table III.2 entry III.C). Three changes investigated the effect of the rib-stringer-skin joints, these charges being (a) removing all skin bending stiffness in elements adjacent to ribs and spars (Table III.2 entry III.D), (b) removing all beam elements representing joint stiffeners and chord-wise stringers, (Table III.2 entry III.E), and (c) pinning the junctions of the beams representing hollowed ribs to the spars by releasing all appropriate rotational constraints in the finite element model (Table III.2 entry III.F). The first torsional mode in all cases remained about 15 Hz higher than found experimentally. The pin connection between the ribs and spars causes the reduction of the composite bending-torsion mode about 20 Hz to a level very close to measurements, this change being the only notable effect of this set of variations. Modeling the correct NACA airfoil shape for the entire wing also had very little effect (Table III.2 entry III.B).

Significant changes were affected by changing the modelling of the skin. Wrinkles due to damage observed on certain parts of the skin indicated that the skin in its entirety did not effectively resist shear. To compensate, various methods to reduce the skin shear stiffness evolved. The first arbitrarily reduced the thickness of the skin by 50%, including all lost mass as non-structural mass. Entry III.G in Table III.2 shows that the frequency of the first torsional mode decreased to the value measured experimentally, and the frequency of the second bending and composite modes also were reduced. By removing the shear stiffness from the centers of the bays, and retaining the true structural thickness around the ribs and spars, the first torsional frequency was also reduced to near the measured level (Table III.2 entry III.H). By this modelling the composite mode has a lower frequency than the second bending, and in this sense corresponds to the experimental results.

Some of the sensitivity of the higher order modes to skin stiffness may relate to the cut-off phenomenon associated with waves propagating in the skin between spanwise stringers. If the stringers were to present a significant constraint to the skin motion, wave propagation along the skin would not occur at frequencies below the fundamental resonance of the strip between the stringers.

The effect of fuel on the wing response is simulated by adding 217 pounds of non-structural mass in the area of the leading-edge tanks located inboard of the engine location. The amount of mass added is taken to correspond with that used in the experimental evaluation (Ref. 2). Since the static mass of the wing is 220 pounds in the absence of fuel, a reduction in the translational (i.e., low frequency) response of the wing would be expected.

The influence of the fuel mass on the drive point response in the three directions is shown on Figs. III.6. In the lift direction (Fig. III.6a) the response with the fuel is generally decreased and resonances are shifted to lower frequencies. Because of the resonance shifts, however, there are localized regions in frequency where somewhat higher levels are found. In the vicinity of the 125 Hz blade-passage frequency reductions of 5-10 dB are found. A reasonably constant reduction at low frequency of approximately 10 dB is found in the spanwise direction (Fig. III.6b). Once again the lowering of the resonances results in an increase in level of approximately 10 dB near 150 Hz. In the thrust direction shown on Fig. III.6c, a reasonably uniform reduction of 7 dB is found throughout the frequency range.

3. Final Model

The series of parameter studies described above lead to creation of the final finite element representation of the wing shown on Fig. III.7. Features of this model which include many of those of the previous models are as follows: global use of plate elements; asymmetric airfoil contour; stiffened structure for engine mount.

Results of this model are compared with measurements on Figs. III.8 where narrow-band drive-point and transfer accelerances are presented. Figs. III.8a and b show the comparison for the drive-point response in the lift and thrust directions, respectively. The mean values of the calculated and measured levels are found to be in very good agreement with the measurements. Narrowband differences of 10-15 dB appear in regions near specific resonances and antiresonances of measurements and calculations. Apparent in the drive-point response in the spanwise direction shown on Fig. III.8c is the lack of analytical modes in the frequency range around 75 Hz which would likely alter the results from mass-like to stiffness-like behavior at a lower frequency. The transfer response in the lift direction between bolt excitation and response 83 inches outboard along the main spar is shown on Fig. III.8d. Once again relatively good agreement is obtained between the mean values of the measured and calculated responses.

The fact that the mean response of the model are in good agreement with those measured suggests the ability of using the final model for narrowband calculations given the interpretation of such calculations in terms of band-averaged means and associated variances. Such comparisons using the wing model along with results of the fuselage model are discussed in the section that follows.

TABLE III.1

FUNDAMENTAL MODES MEASURED ON THE BEECHCRAFT BARON

Out-of-plane bending	46 Hz
In-plane bending	134 Hz
Axial compression	572 Hz
Torsional	53 Hz

TABLE III.2

FREELY-SUPPORTED WING RESONANCE FREQUENCIES

Description	Fundamental Bending	Fundamental Torsion	Bending	Composite Bending/Torsion
I. Determined	46	53	103	87
II. Simplified Models				
A. Beam Ladder-type	44	50	117	110
B. Inboard section modeled in detail with plate elements	45	54	108	120
III. Plate Element Models				
A. Symmetric model	44	67	107	114
B. Non-symmetric model using NASA 23016 (root) to 23010 (tip) sections	45	71	106	119
C. Engine mount added to model III.B	45	70	105	118
D. No bending stiffness of skin elements adjacent to rib-stringer joints	45	71	106	119
E. No chordwise stringers or web-skin and spar-skin stiffness	46	70	111	103
F. Pin connections between ribs and spars	44	67	105	93
G. Structural skin thickness reduced by 50%; weight added as non-structural mass	40	53	97	110
H. Removal of membrane (i.e., shear stiffness) of skin from center of bays between stringers and ribs	42	49	101	92

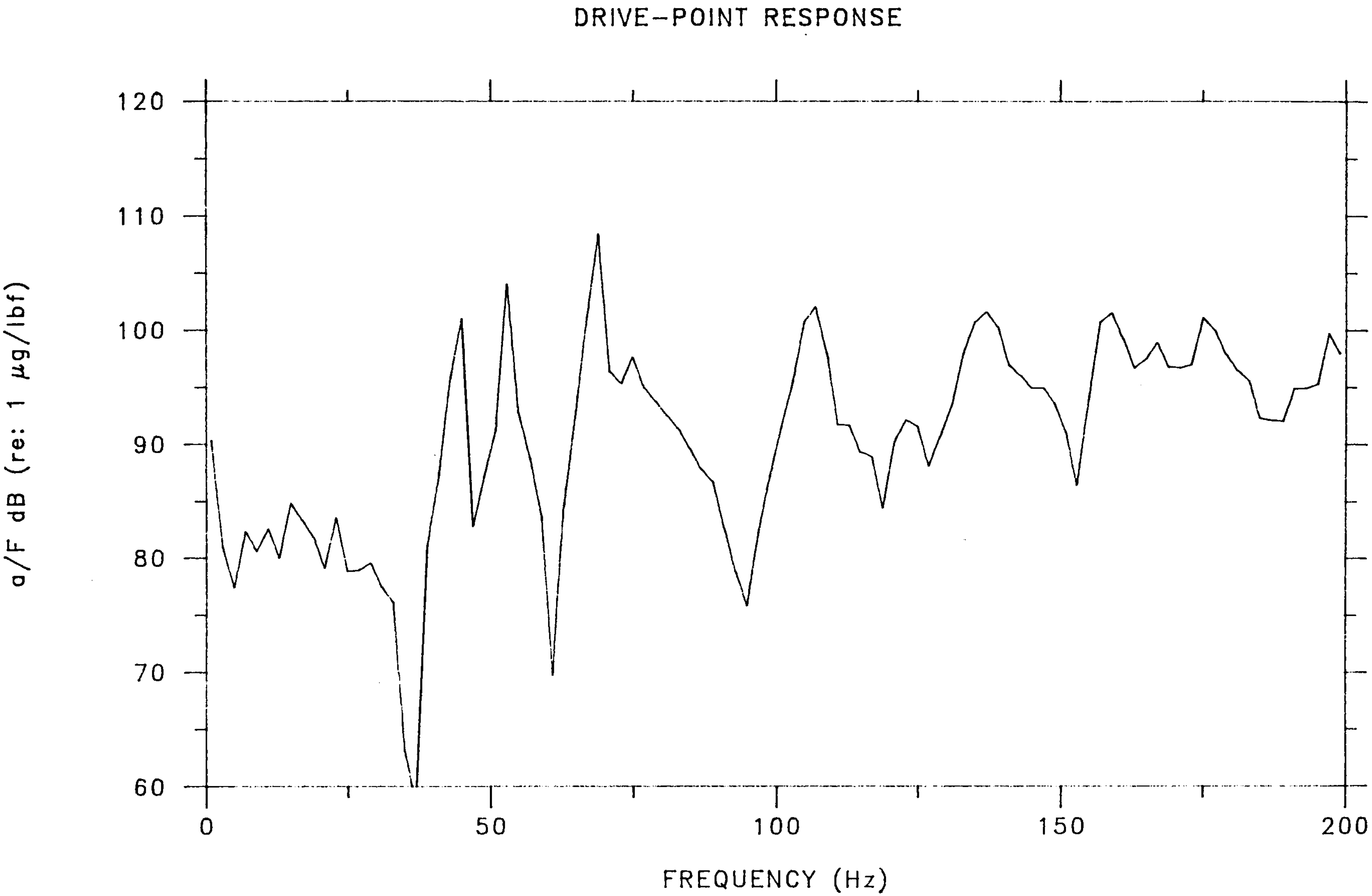

Fig. III.1 Measured drive point accelerance in the lift direction at the forward spar bolt location on the freely suspended wing.

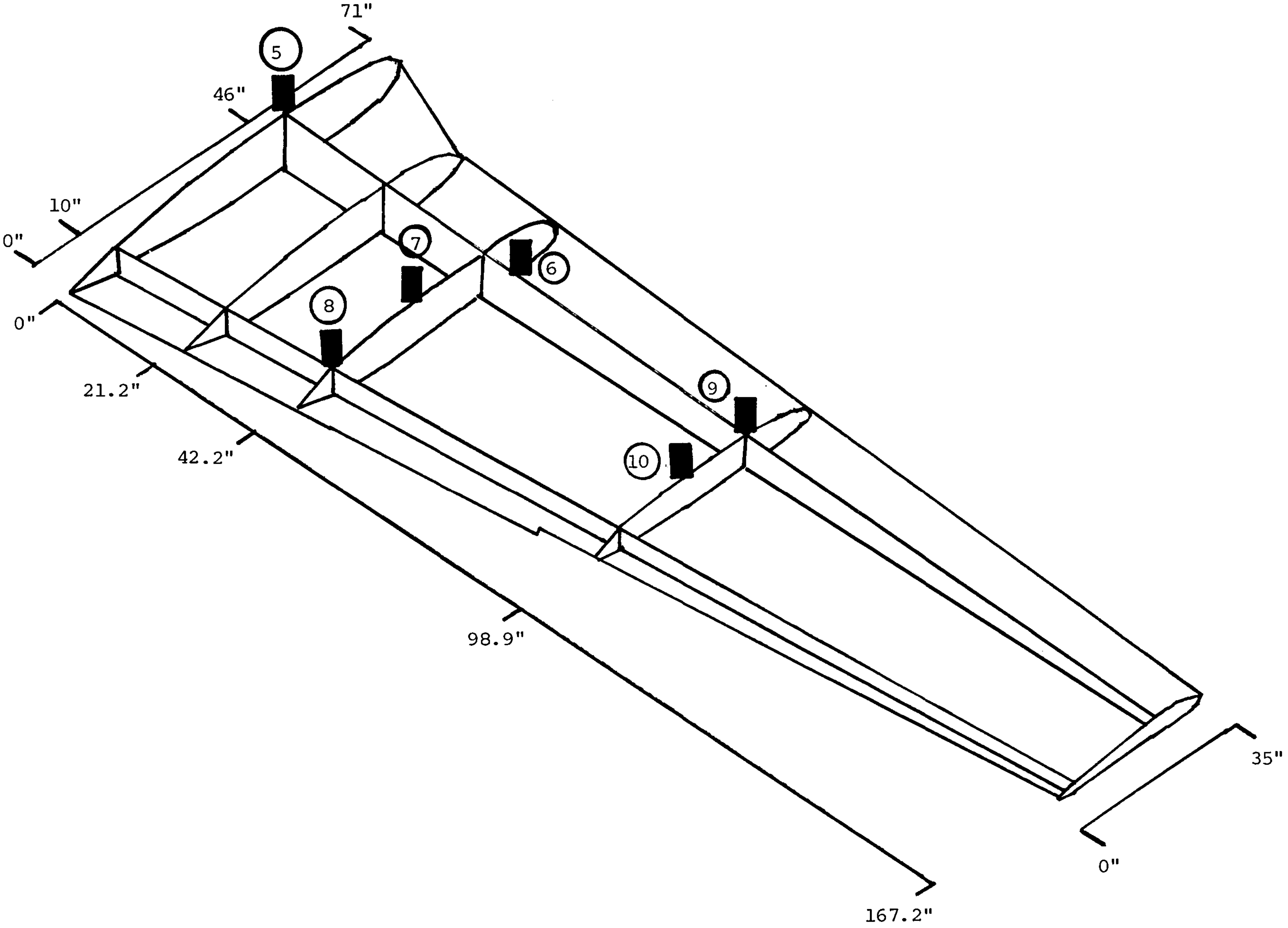

Fig. III.2 Locations for structural transfer measurements on the wing.

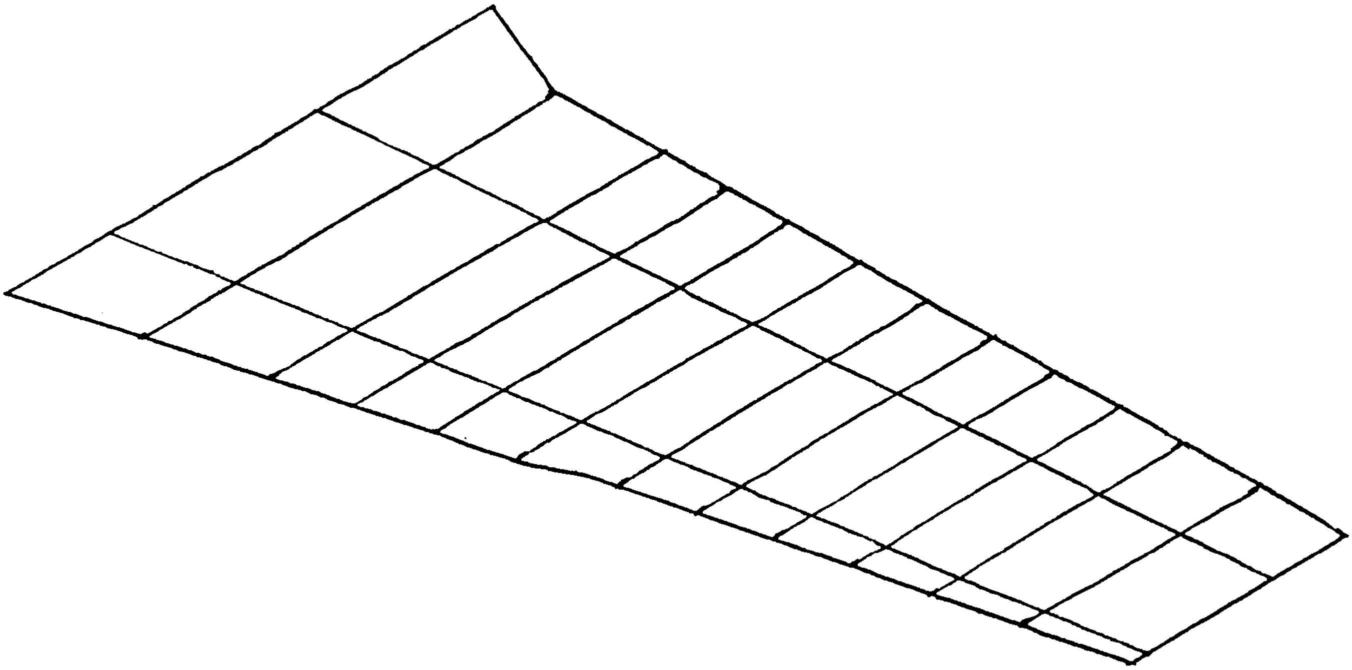

Fig. III.3 Multi-beam ladder model of the wing.

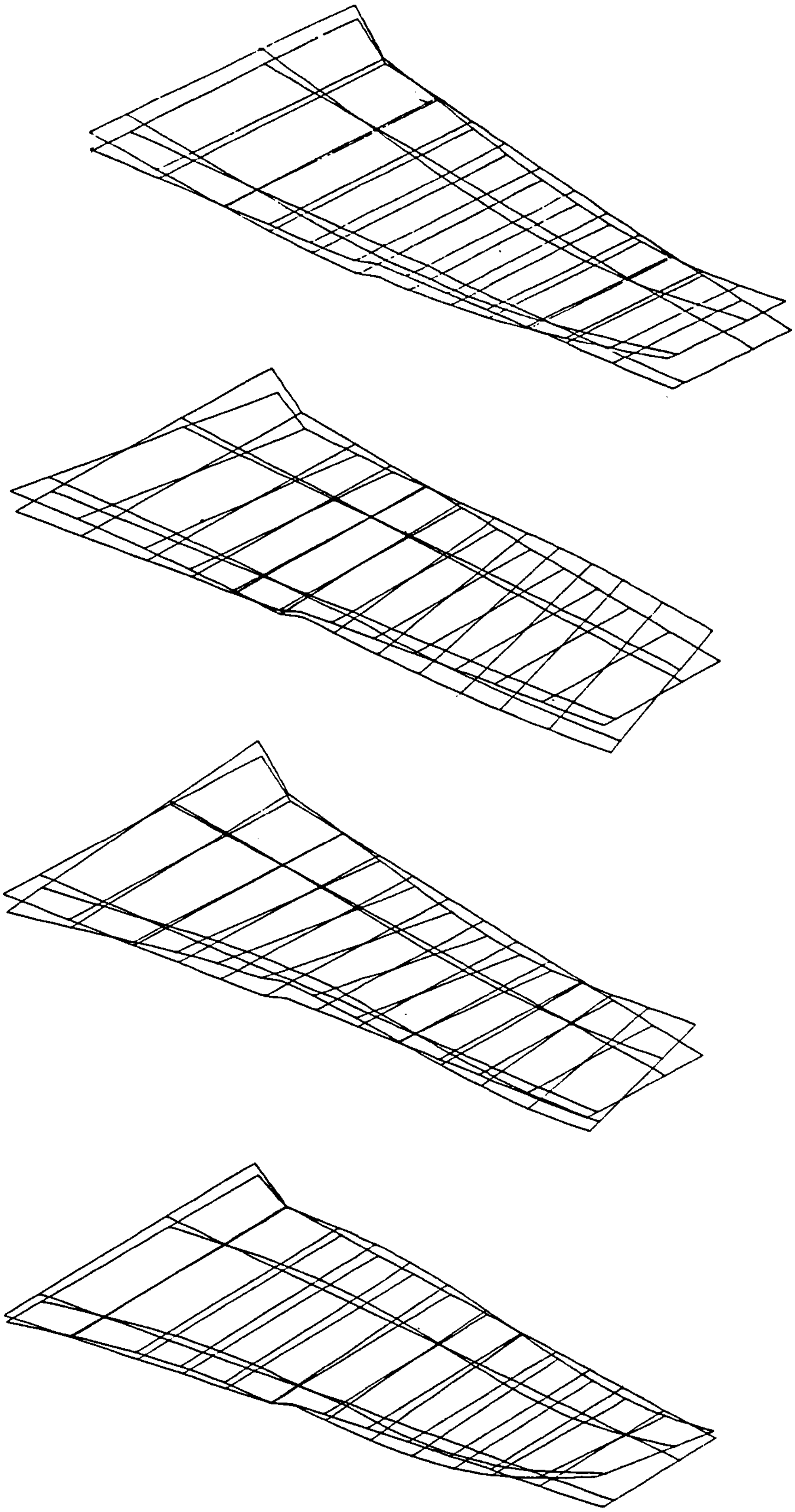

A. First bending
out-of-plane
44 Hz

B. First torsion
50 Hz

C. Composite
bending-
torsion mode
110 Hz

D. Second bending
out-of-plane
117 Hz

Fig. III.4a Mode shapes calculated using ladder model.

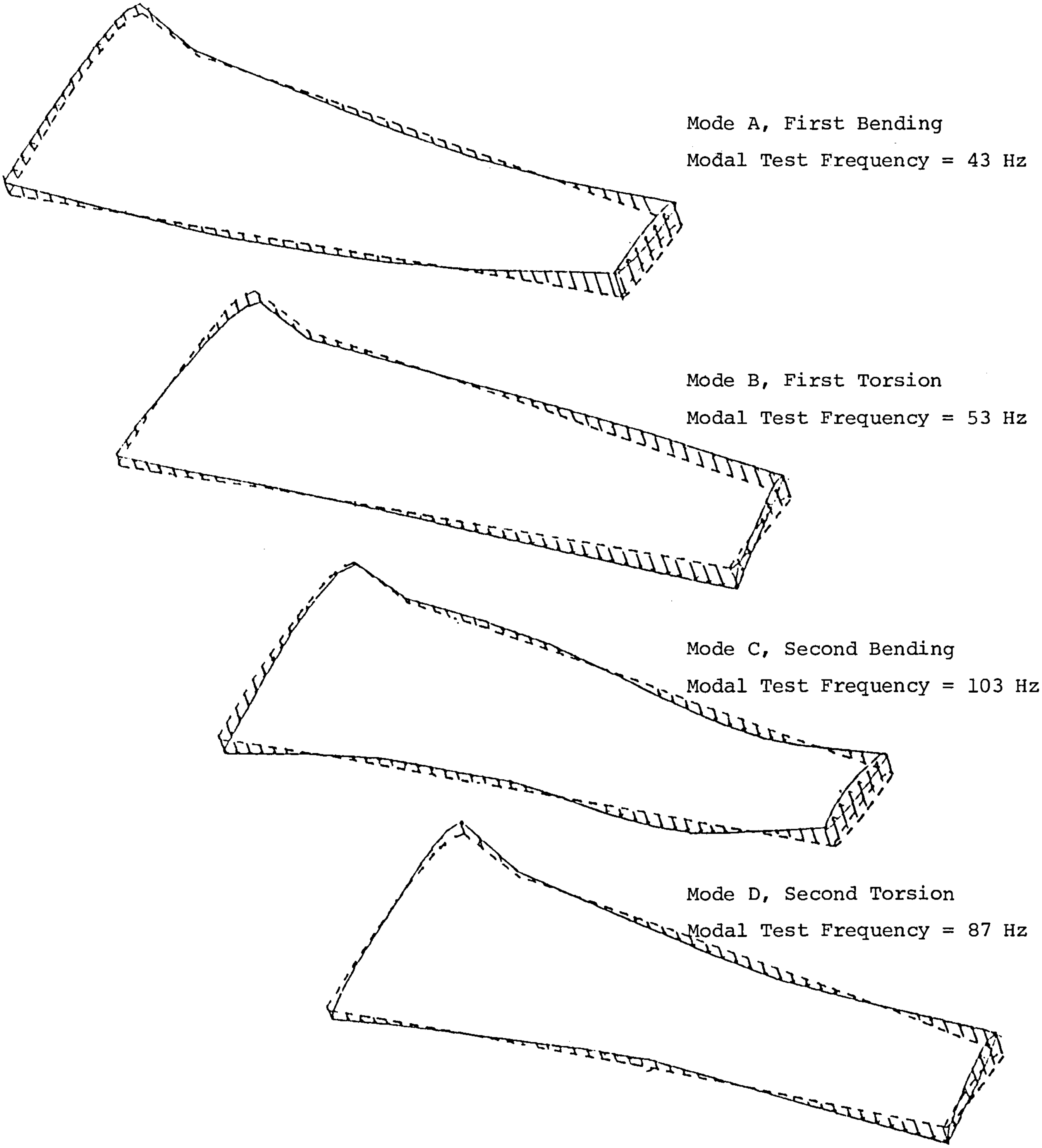

Fig. III.4b Measured mode shapes for freely supported wing.

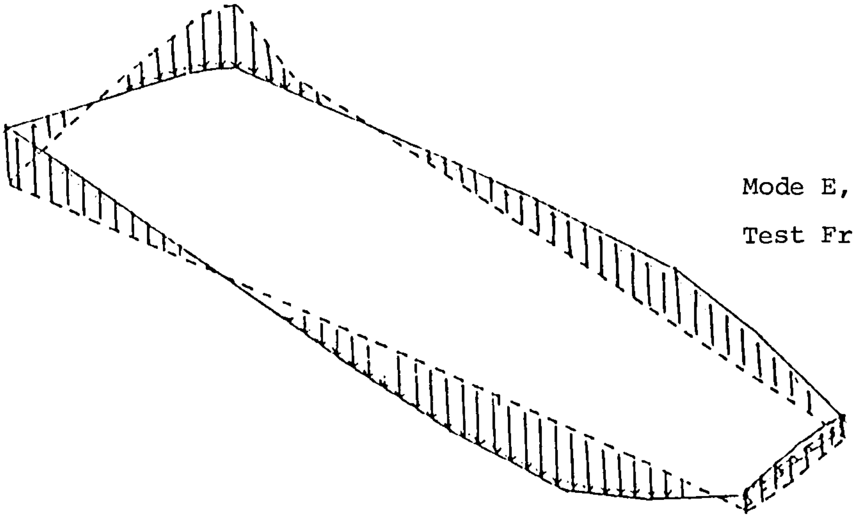

Mode E,

Test Frequency = 74 Hz

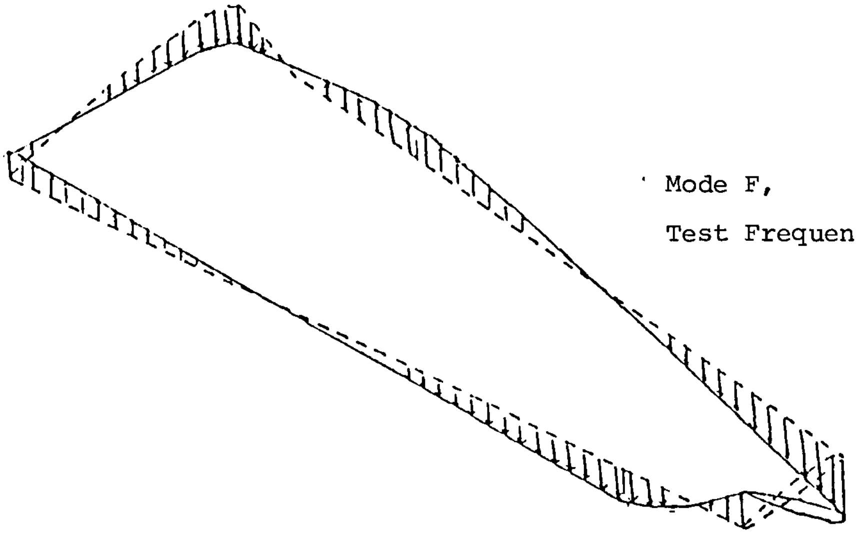

Mode F,

Test Frequency = 68 Hz

Fig. III.4b (Continued)

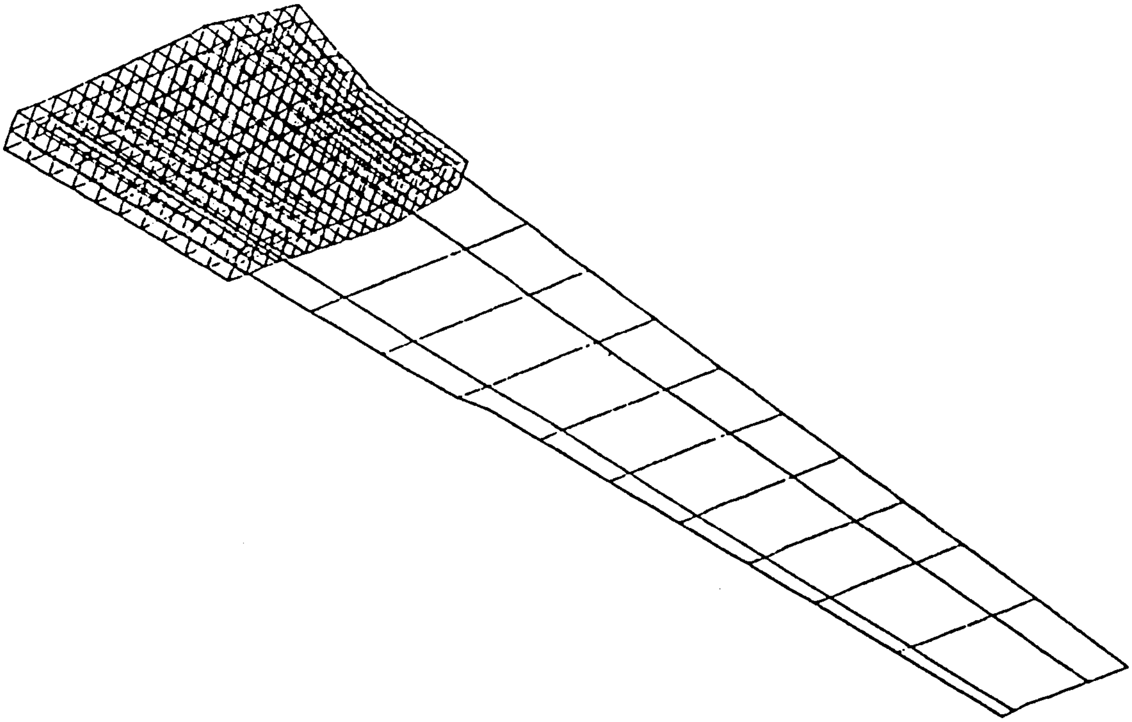

Fig. III.5 Composite model of the wing using a detailed model of the inboard structure of the wing.

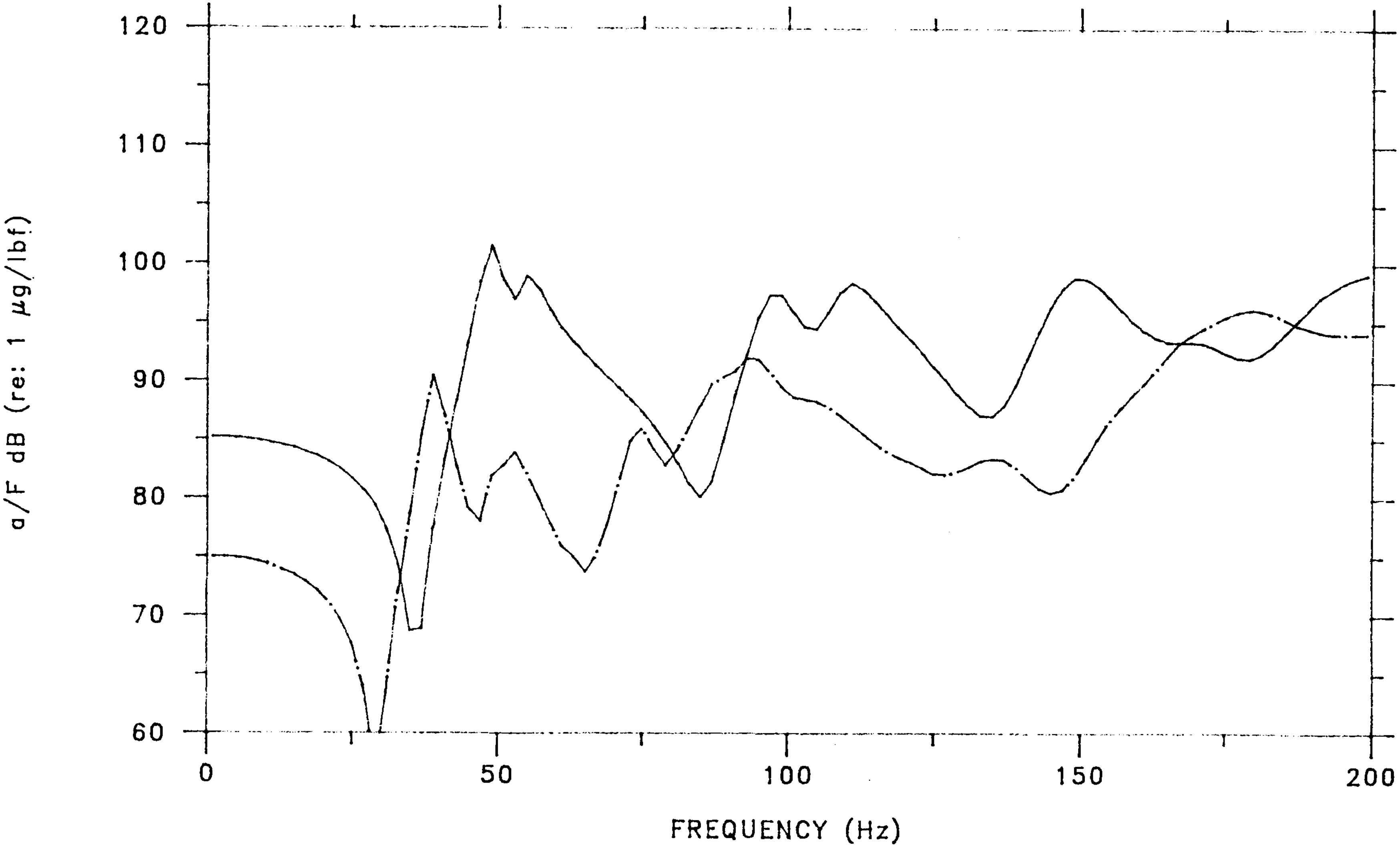

Fig. III.6a Drive-point accelerance of the freely-supported wing in the lift direction with (—·—) and without (——) simulated fuel mass.

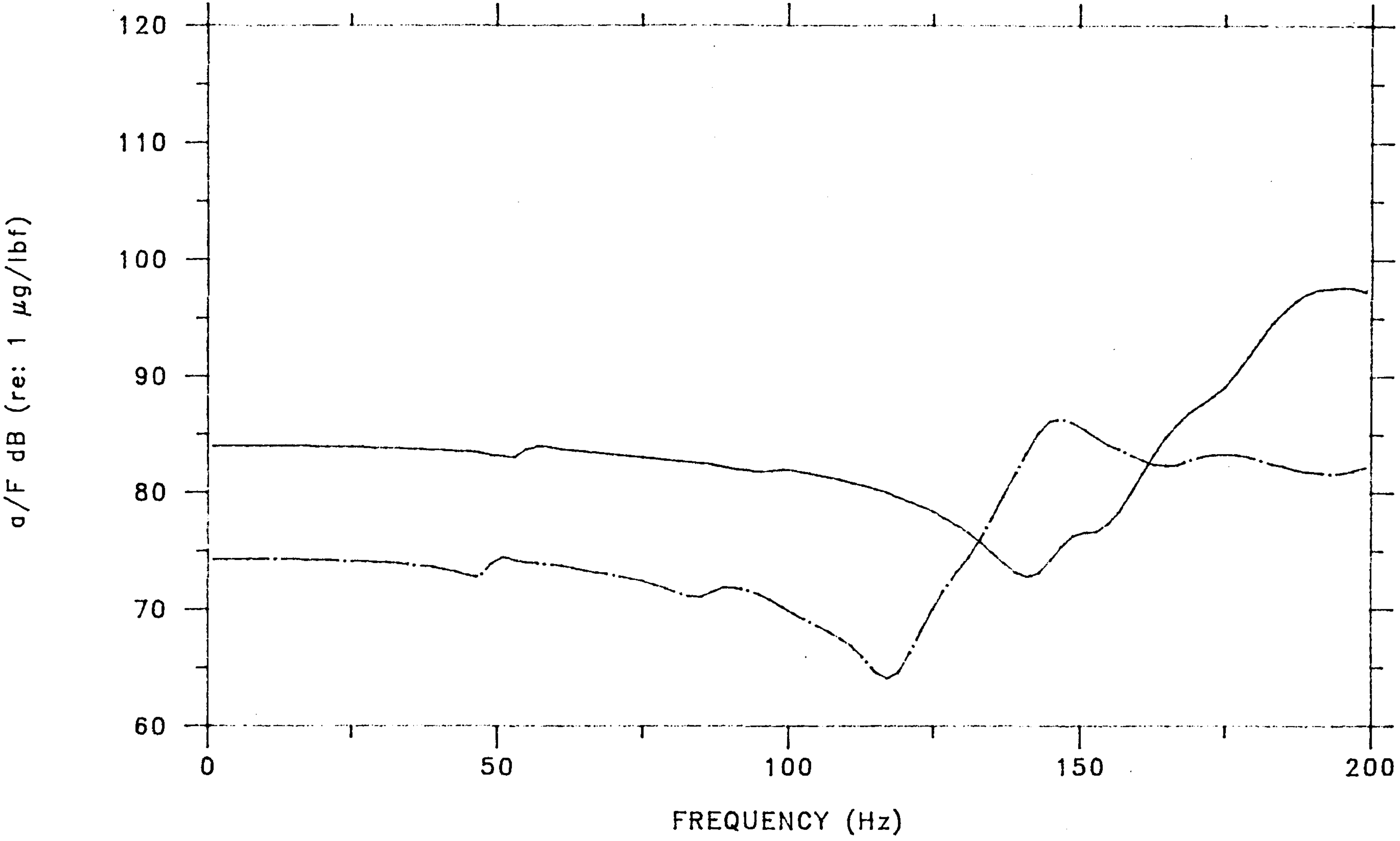

Fig. III.6b Drive-point accelerance of the freely-supported wing in the spanwise direction with (—·—) and without (——) simulated fuel mass.

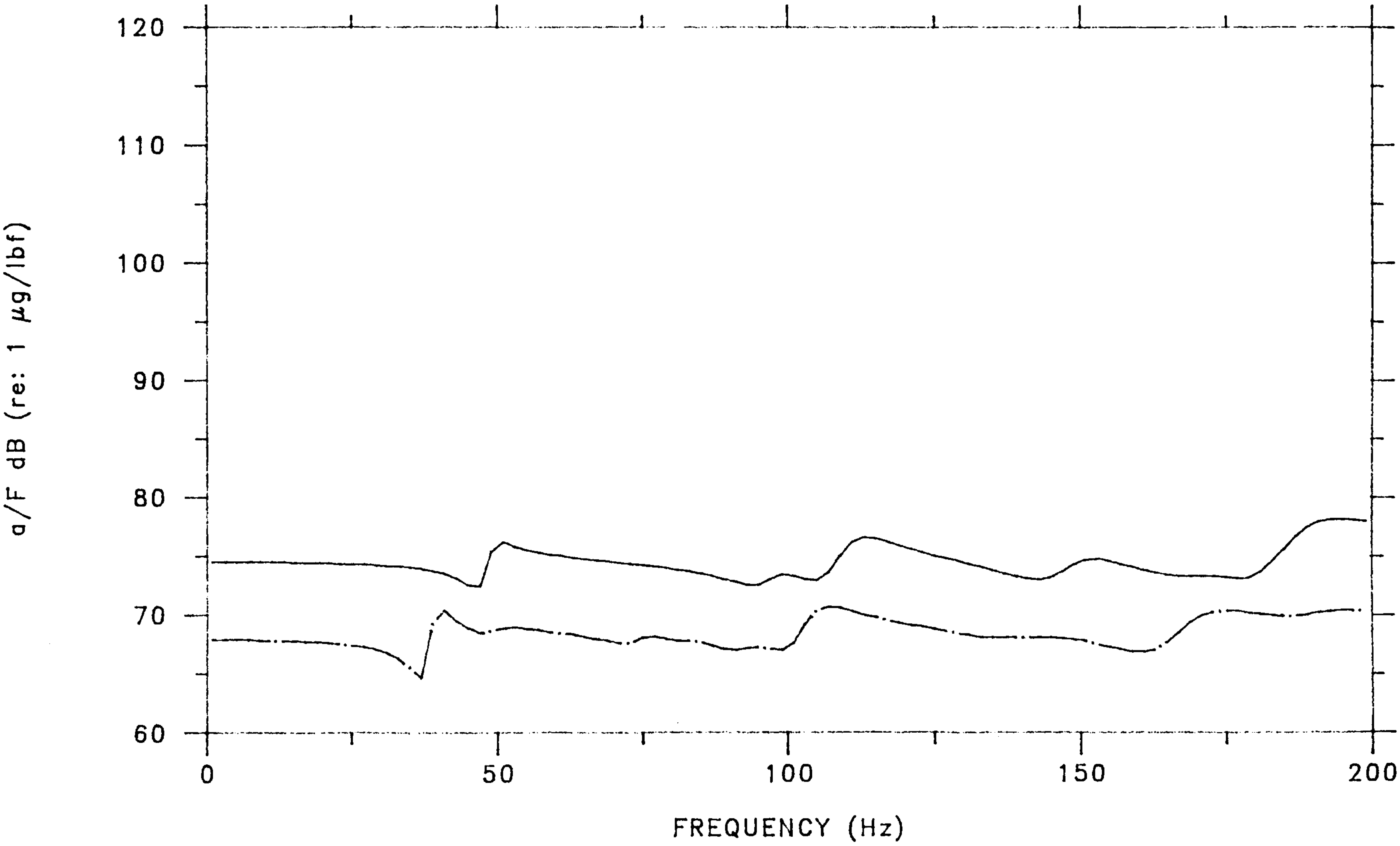

Fig. III.6c Drive-point accelerance of the freely-supported wing in the thrust direction (—·—) and without (——) simulated fuel mass.

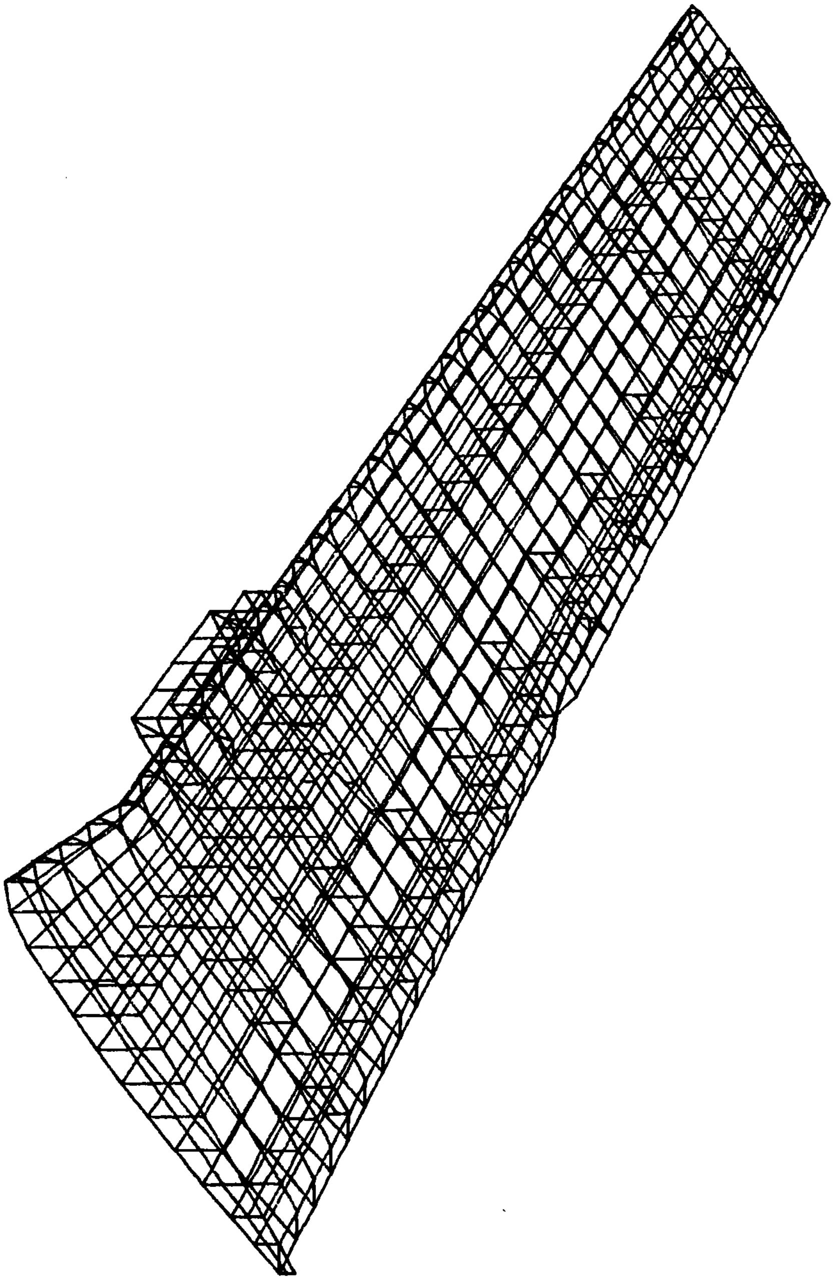

Fig. III.7 Final finite element model of the wing.

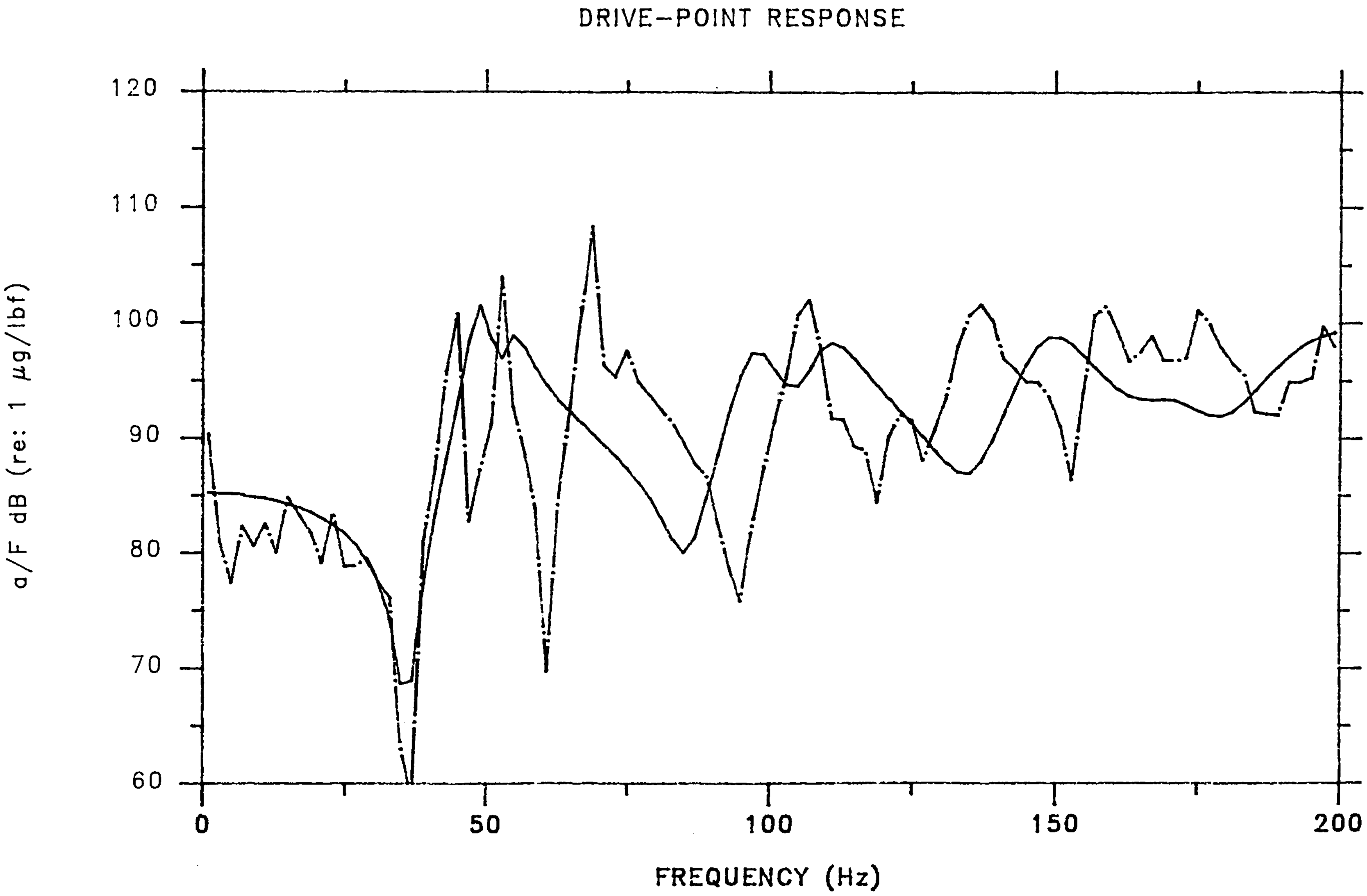

Fig. III.8a Drive-point accelerance at the main spar bolt location in the lift direction.
(—·—, measured; ——, calculated).

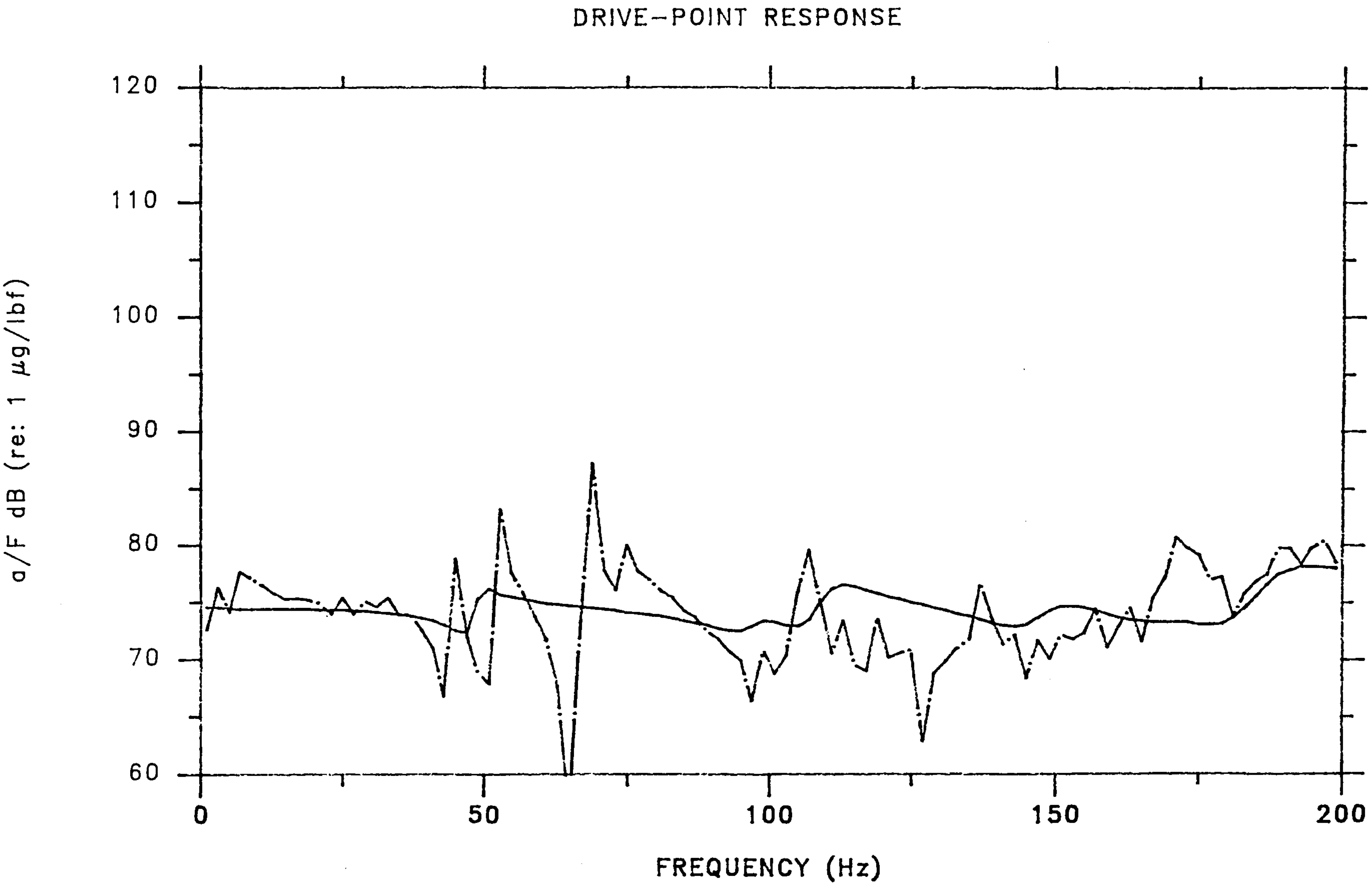

Fig. III.8b Drive-point accelerance at the main spar bolt location in the thrust direction. (—·—, measured; ——, calculated)

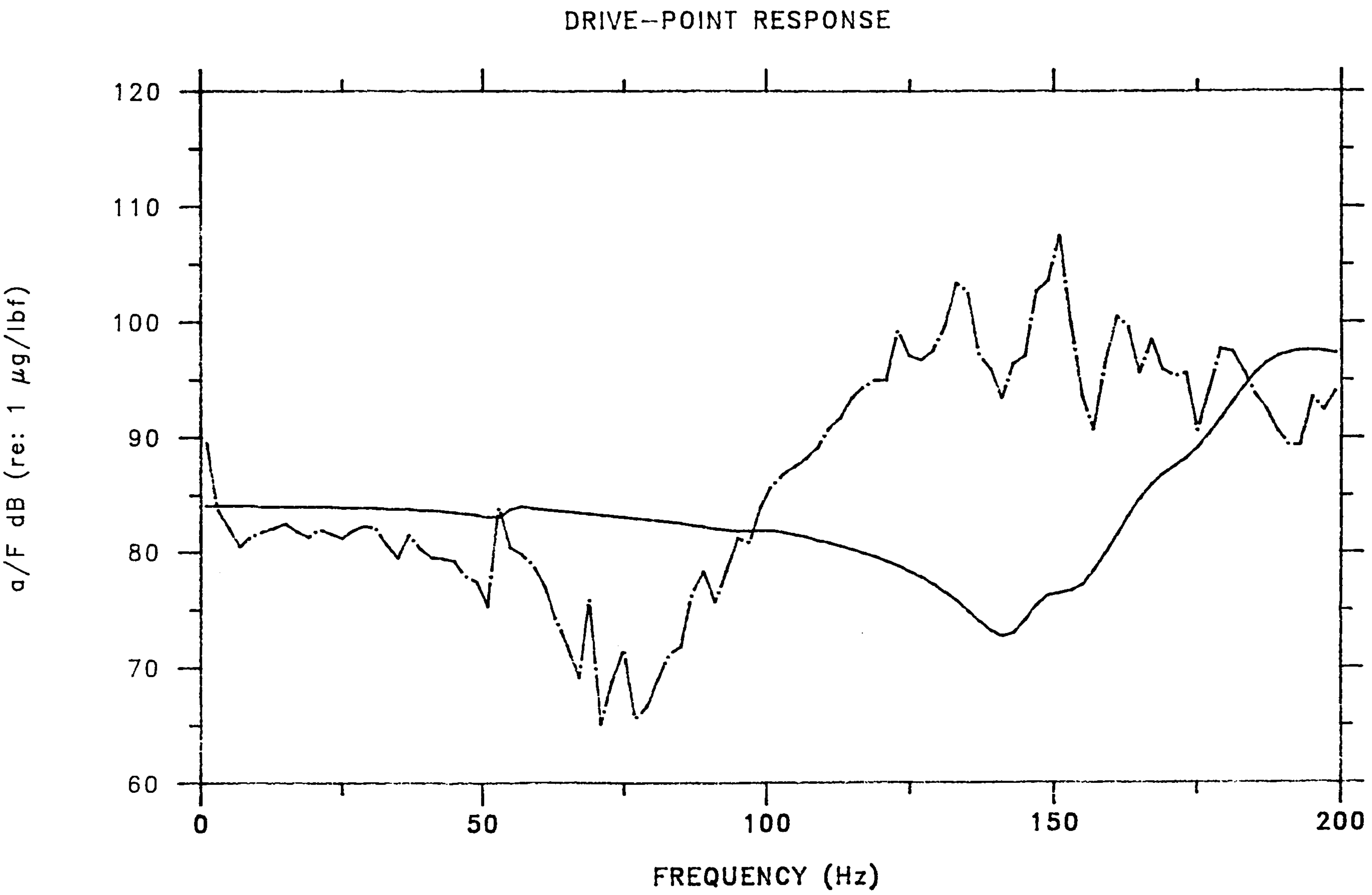

Fig. III.8c Drive-point accelerance at the main spar bolt location in the spanwise direction.
(—·—, measured; ——, calculated)

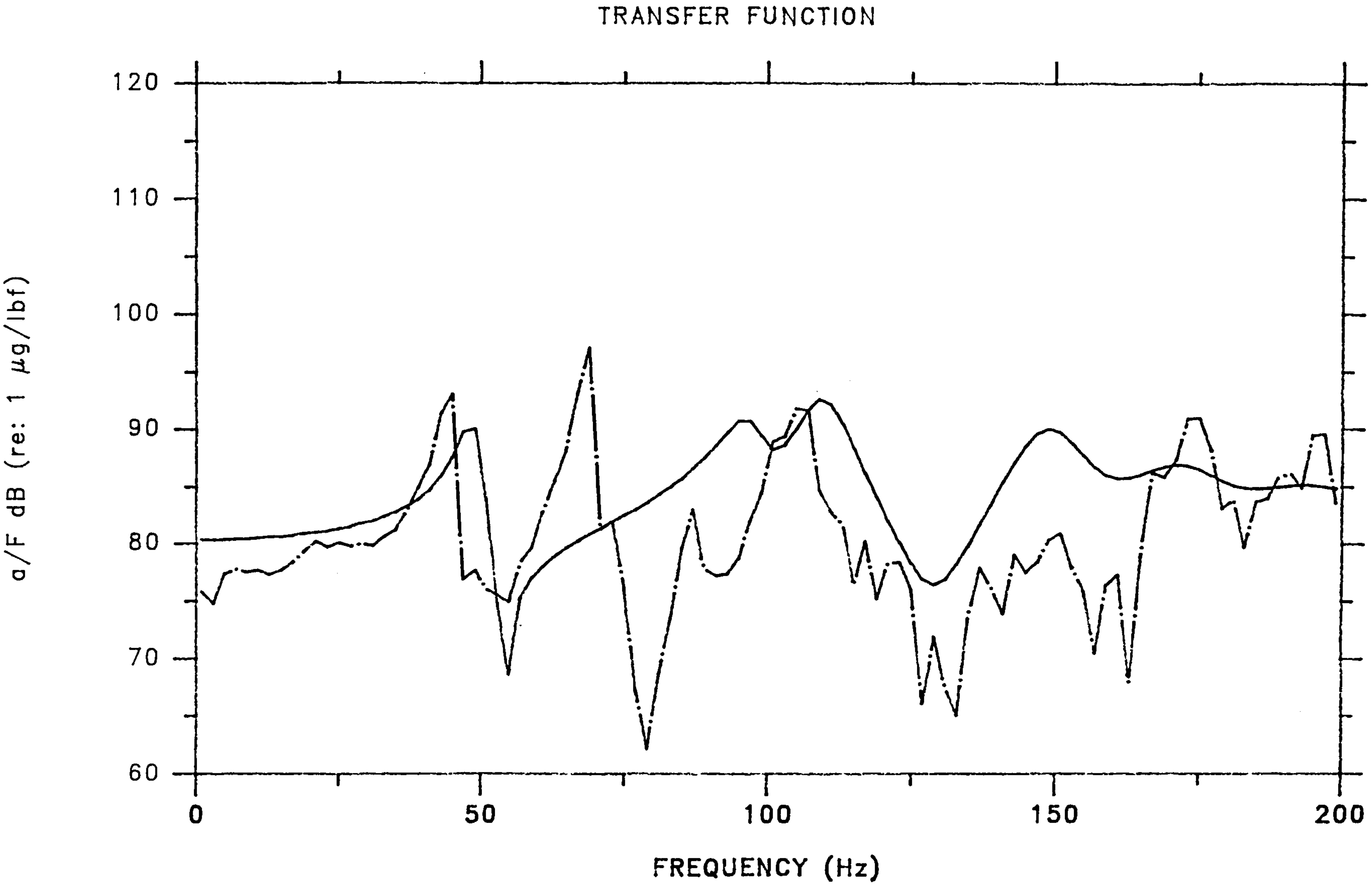

Fig. III.8d Transfer accelerance in the lift direction between the bolt and a location 83 inches outboard along the main spar (—·—, measured; ——, calculated).

IV. INTERFACE OF WING AND FUSELAGE MODELS

A. Introduction

The bolted connection between the wing and the fuselage permits the models of each structure to be interfaced in a straightforward manner to form a global model of the structureborne path from excitation of the wing to acoustic pressure in the cabin. The methodology treats each structure in terms of drive-point and transfer admittances. We assume the bolts to be rigid connectors that constrain displacements between the wing and fuselage and result in equal and opposite internal forces being applied to each structure. Results of this procedure have been calculated to examine sensitivity to assumptions in orientation of the fuselage model and to assess the effects of interface compliance of structureborne noise.

B. Admittance Matrix Formulation

The wing is modeled as having both input and output locations and described by the following mobility relationships:

$$\begin{bmatrix} \dot{w}_1 \\ \dot{w}_2 \end{bmatrix} = \begin{bmatrix} Y_{11} & Y_{12} \\ Y_{21} & Y_{22} \end{bmatrix} \begin{bmatrix} F_1 \\ F_2 \end{bmatrix} \qquad \text{(IV.1)}$$

where locations 1 and 2 designate input and output respectively (see Fig. IV.1). Each of the above mobilities are 12 x 12 matrices containing the information for three orthogonal directions at each of the four bolt locations (Fig.IV.2). These relations can be reformulated to express input in terms of output quantities,

$$\begin{bmatrix} F_1 \\ \dot{w}_1 \end{bmatrix} = \begin{bmatrix} \alpha_{11} & \alpha_{12} \\ \alpha_{21} & \alpha_{22} \end{bmatrix} \begin{bmatrix} F_2 \\ \dot{w}_2 \end{bmatrix} \qquad \text{(IV.2)}$$

where

$$\alpha_{11} = Y_{22}\, Y_{21}^{-1}$$

$$\alpha_{12} = Y_{21}^{-1}$$

$$\alpha_{21} = Y_{12} - Y_{22}\, Y_{11}\, Y_{21}^{-1}$$

$$\alpha_{22} = Y_{11}\, Y_{21}^{-1}$$

The fuselage model describes the structure in terms of its input (i.e., drive-point) mobility,

$$\dot{w}_3 = Y_{33}F_3 \tag{IV.3}$$

At the interface a rigidly bolted connection between the two systems requires equal velocities and equal and opposite internal forces; consequently,

$$\begin{aligned} \dot{w}_2 &= \dot{w}_3 \\ F_2 &= -F_3 \end{aligned} \tag{IV.4}$$

Using these relations in Eq. IV.1, we obtain the following ratio between interface and applied forces:

$$\frac{F_3}{F_1} = \frac{Y_{21}}{Y_{22}+Y_{33}} \tag{IV.5}$$

Furthermore, the cabin pressure can now be obtained by using the transfer function relating acoustic pressure to applied force,

$$\frac{P_4}{F_1} = \frac{F_3}{F_1} T_{43} = \frac{Y_{21}\ T_{43}}{Y_{22}+Y_{33}} \tag{(V.6}$$

The transfer function T_{43} is a 12 x 1 vector relating the pressure to the forces in the three directions at each bolt.

C. Coordinate System Compatibility

The natural coordinate system for the fuselage model is cylindrical in which the three orthogonal components of the shell response are in the radial, circumferential, and longitudinal directions. Calculations from the shell model of the fuselage provide the shell responses that are excited by loads in each of these directions.

While this coordinate system is natural for the cylindrical shell model, it differs from that of the actual aircraft fuselage and wing for which the natural coordinate system is defined by the spanwise, lift, and thrust directions. The thrust direction of the wing is aligned with the longitudinal direction of the shell. At any one point on the shell the radial and circumferential directions can be oriented with the spanwise and lift directions of the wing, however, the connection between the wing and fuselage is made by two bolts separated in the lift direction at both the forward and rear wing spars. In general the fuselage response in the shell coordinate system can be rotated to be compatible with the coordinate system of the wing for any assumed attachment orientation relative to the wing.

Coupling of the wing and fuselage models through the bolts requires drive-point and transfer responses of the structures at the bolt locations. Specifically the drive-point mobilities in all three directions at each bolt are required as well as the transfer mobilities in each direction between forces applied to one bolt and the responses at the other three bolts. Because the structural model of the fuselage is axisymmetric, the drive-point mobilities are independent of circumferential orientation at a specified longitudinal location. Furthermore, structural reciprocity provides equivalences among transfer mobilities between two bolt locations. As a result of these factors, calculations for loads applied to all four bolt locations are not required to determine the full coupling matrix.

Because of the lack of symmetry of the wing, calculations of the input and transfer mobilities at all four bolt locations are required.

D. Propeller Induced Wing Loading

The excitation of the structureborne path of a Beechcraft Baron in flight is the propeller induced downwash that acts on the wing surface. This pressure loading is calculated in Ref. 1 for a general multi-bladed high speed propeller. In order to interface with the finite element of the wing, the surface pressure must be integrated piecewise along the surface to give resultant forces acting at the structural nodes. This integration procedure is described in Ref. 10 where it is applied to the Baron.

E. Results

The models of the wing and fuselage have been coupled in two configurations to examine sensitivity of cabin pressures to interface parameters. In one configuration the wing is effectively attached at the bottom of the fuselage shell while in the other configuration the wing is joined to the shell at the horizontal diameter. As we shall see the acoustic levels in the cabin are substantially higher for the former configuration than for the latter.

The reason for this result is found by examining the input accelerances to both structures. As shown on Fig. II.14b the calculated accelerance of the wing above 70 Hz is substantially higher in the radial direction than in either the circumferential or axial directions. Results from the wing model from Figs. III.8a and c show the accelerance in the lift direction at low frequency to be generally higher than that in the spanwise direction.

When the models are interfaced with the wing near the horizontal diameter of the fuselage, the relatively compliant lift direction of the wing is connected to the relatively stiff circumferential (i.e., in-plane) direction on the fuselage structure. Similarly a mismatch exists between the stiff spanwise response of the wing and the compliant radial (i.e., out-of-plane) response of the shell. Because of this mismatch, relatively small interface forces are calculated and the resulting cabin pressure is low.

A method of attachment that is more consistent with the experimental data and construction of the Baron is to join the wing to the fuselage such that the relatively stiff spanwise response of the wing interfaces with the circumferential response of the shell. Physically, the carry through structure in the fuselage maintains structural compatibilities in the spanwise direction. The improved matching of structural accelerances results in higher interface forces, thereby producing higher pressure levels in the cabin.

Results are shown on Fig. IV.3 for a hammer impact excitation of the wing at a location 83 inches outboard on the main spar. Here the measurements are compared with the analytical model for the two attachment configurations. Although some low frequency peaks of the measurements are also found in the calculations, the analytical predictions underestimate the

the data below 160 Hz. The results of the model when the wing is attached at the horizontal diameter of the fuselage shell are approximately 20-30 dB below the measurements over a broad frequency range. The more compatible attachment configuration results in levels that are 10-15 dB higher above 70 Hz and in somewhat better agreement with the measurements.

In Fig. IV.4 results are presented for the same model when the wing is excited by the distributed loads induced by the propeller downwash. Since the loading is tonal at the blade passage frequency, the cabin pressure is calculated for the loading at this frequency over the adjacent one-third octave band range of frequencies. The results provide a means to assess the sensitivity of the model to frequency and thereby to establish a calculated variance in response levels. Once again the more compatible attachment configuration results in levels approximately 10-15 dB higher than the other configuration. The dip in the calculated results that is found in both structures in this frequency range, the null in the fuselage being particularly severe in the circumferential direction.

Also shown on Fig. IV.4 is the total noise measured in-flight on an ensemble of twin-engine aircraft having 3-bladed propellers (Ref. 11). When averaged over the one-third octave band, the calculated level for the compatible configuration is within 10 dB of the average measured level. This suggests the importance of the structureborne path; however, because of the large variance in the calculated results, care must be exercised in interpreting results based on average levels and in assessing implications for noise control.

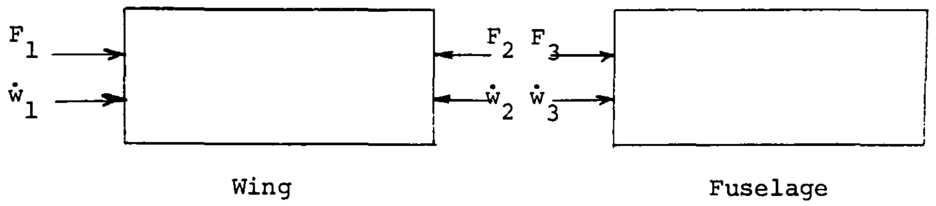

Fig. IV.1 Input and output vectors used in attaching wing and fuselage structures at bolted connection points.

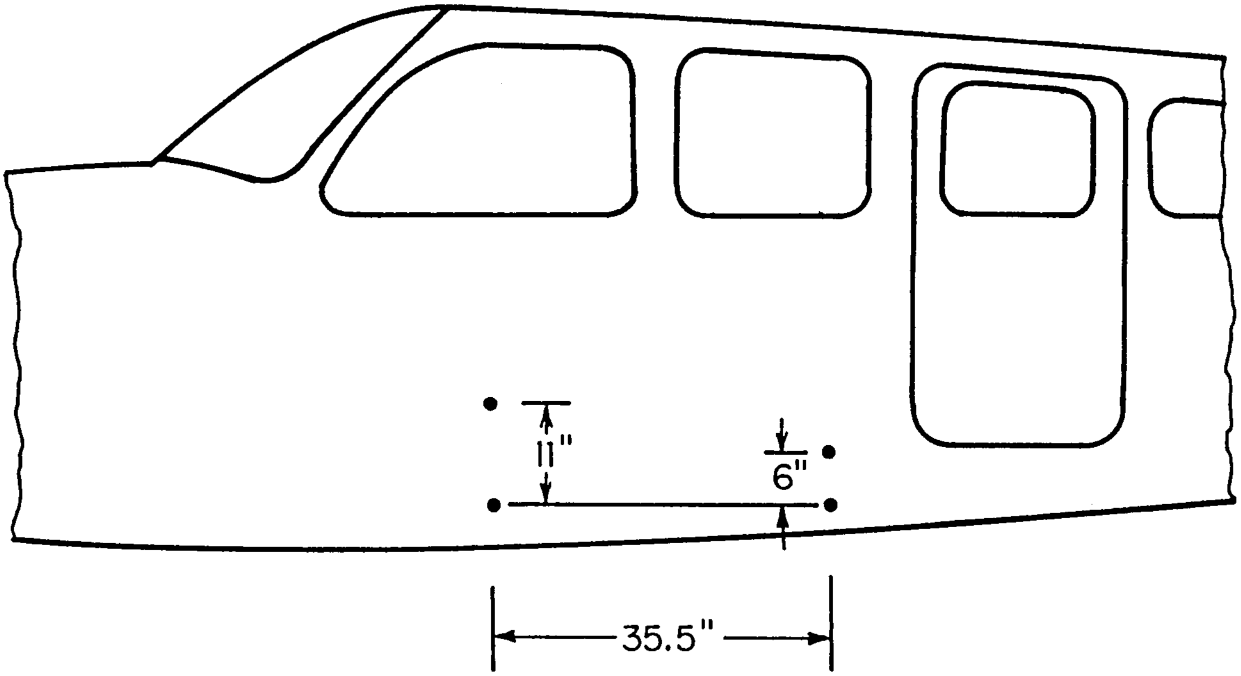

Fig. IV.2 Locations of and distances between wing attachment bolts.

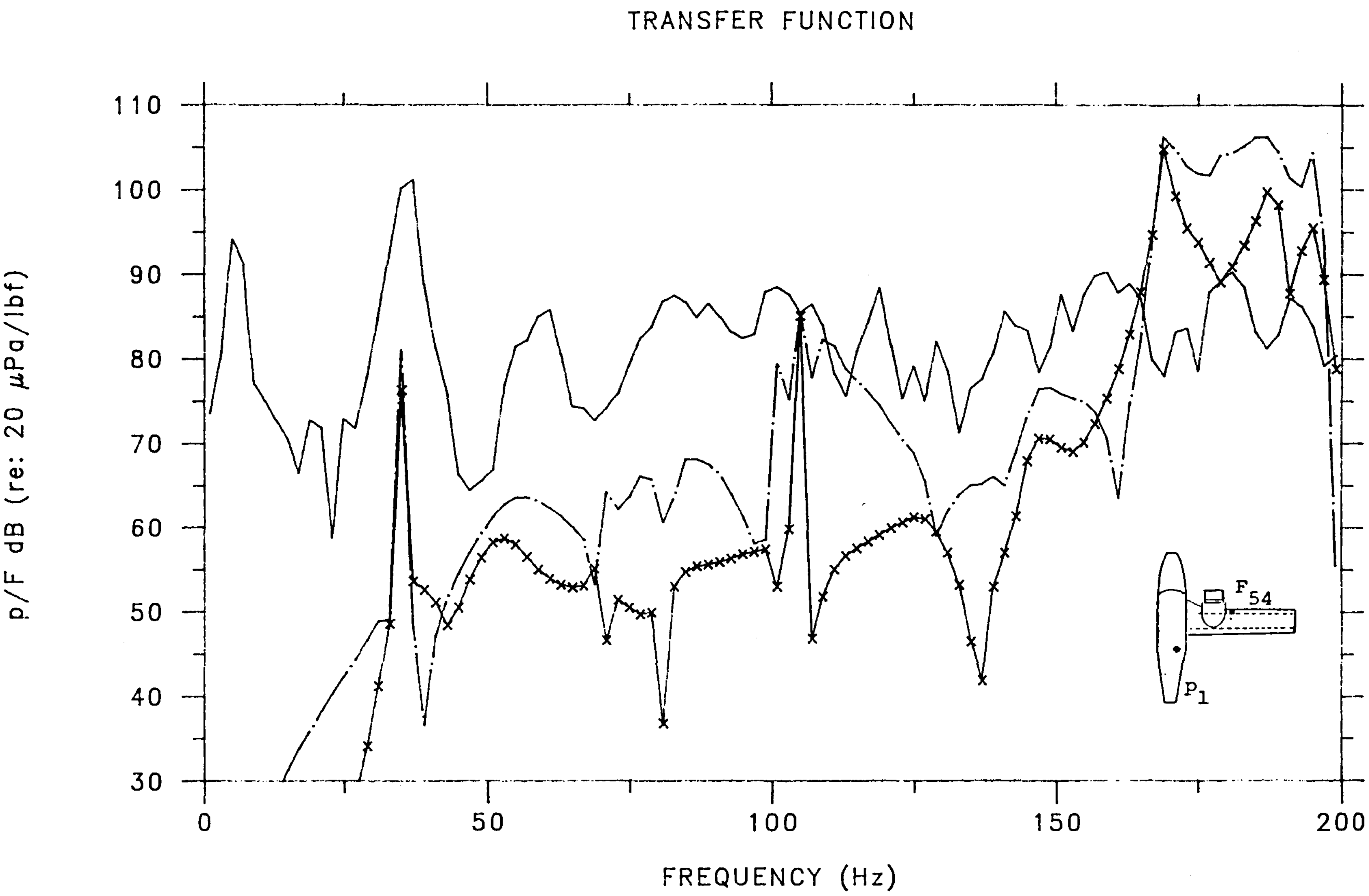

Fig. IV.3 Structureborne cabin pressure level for excitation by hammer impact 83" outboard on main spar (——, measured; —·—, calculated for attachment to shell at 180° from top; —X—X, calculated for shell attachment at 90° from top).

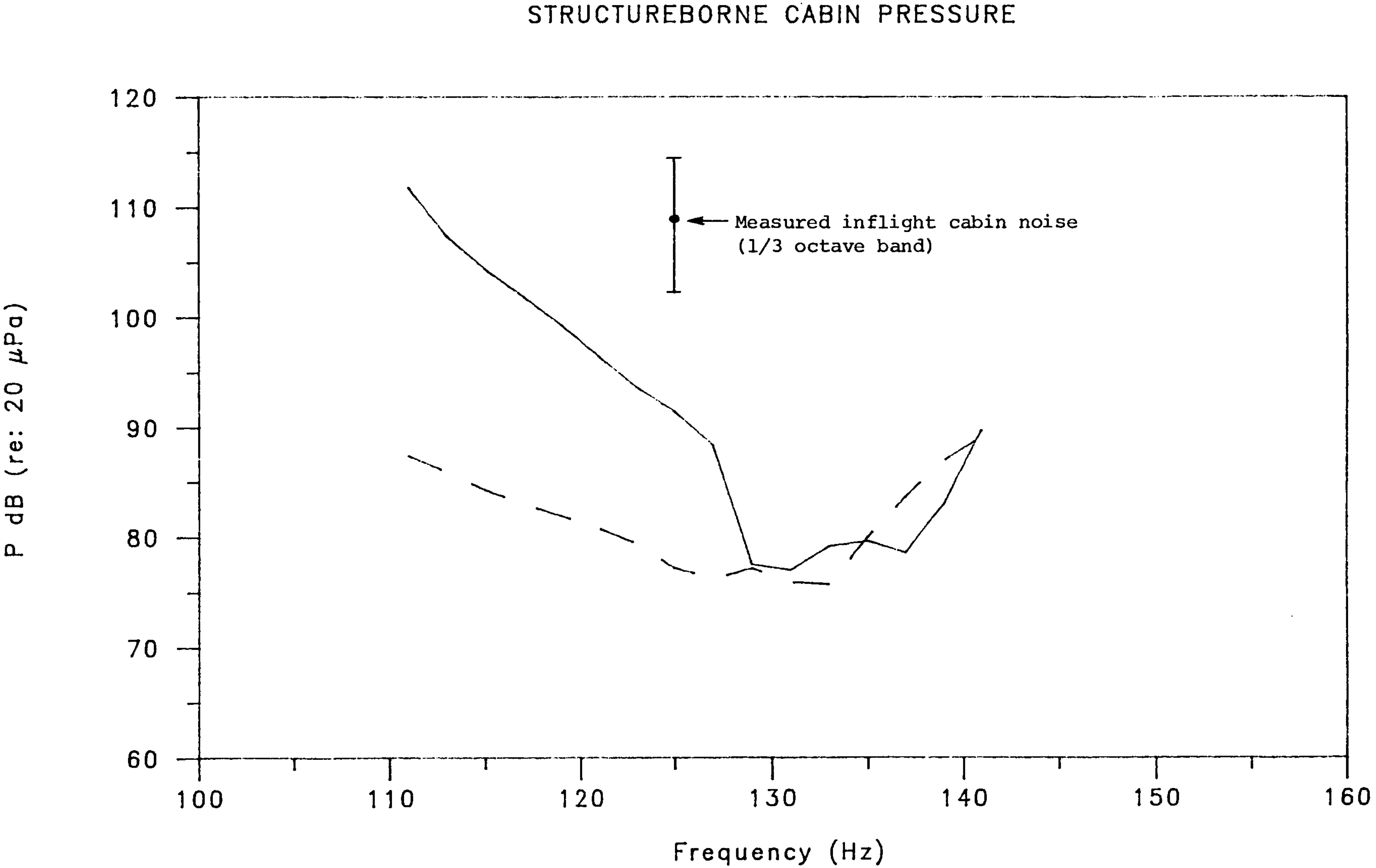

Fig. IV.4 Calculated structureborne cabin pressure level for excitation by propeller loads applied to the wing (attachment to shell at 180° from top (——) and at 90° from top (— — —)).

V. STATISTICAL ENERGY ANALYSIS

A. Introduction

In previous sections analyses are presented of the structural vibrations and cabin pressure levels of a Beechcraft Baron 58P aircraft excited by harmonic forces on the fuselage directly and on the wing mounted engine support structure. The analyses are deterministic with input parameters taken from plans and tables and response functions are computed as a function of frequency for a specified spectral source level.

Although predictions are reported only for wing and fuselage acceleration levels and cabin pressure levels the analyses also determine the flow of power. For example, we may symbolize the steady state analysis of a general (linear) structural-acoustic problem using matrix notation

$$[Z]\vec{U} = \vec{F} \qquad (V.1)$$

where [Z] is an impedance matrix, and $\vec{F}$ and $\vec{U}$ the excitation and response vectors at (circular) frequency ω. The length of the vectors, or the rank of the matrix, may be determined by the mesh size of a discretization process or the point of truncation of a modal formulation. The inversion of the matrix [Z] yields the solution for the vector $\vec{U}$.

Now let us perform some "post-processing"; specifically, we premultiply Eq. V.1 by the diagonal matrix whose elements are the conjugates of the elements in vector $\vec{U}$, diag U^* , and integrate over one cycle,

$$<\mathrm{diag}\{U^*\}[Z]\vec{U}>=<\mathrm{diag}\{U^*\}\vec{F}> . \qquad (V.2)$$

Taking the real part of Eq. V.2 we obtain

$$\mathrm{Re}<\mathrm{diag}\{U^*\}[Z]\vec{U}>=\vec{P} \qquad (V.3)$$

where $\vec{P}$ is, by definition, the input power associated with $\vec{F}$. The i'th equation of matrix Eq. V.3 is of the form

$$\mathrm{Re}\{z_{ii}|U_i|^2 + \sum_{j\neq 1} Z_{ij}<U_i^*U_j>\}=P_i \; . \qquad (V.4)$$

We now define two quantities, E_i such that

$$E_i = m_i |U_i|^2 \tag{V.5}$$

with

$$m_i = \beta_{ii}^{-1} \mathrm{Re}(Z_{ii}) \tag{V.6}$$

and $\beta_{ij} = \omega\eta_{ij}$ such that

$$\mathrm{Re}\{Z_{ij} \langle U_i^* U_j \rangle\} = \beta_{ij} E_i - \beta_{ji} E_j \tag{V.7}$$

We refer to E_i as the (steady-state) stored energy in the "subsystem" denoted by the degree of freedom i, η_{ij} as the coupling loss factor between subsystems i and j for i≠j and dissipation loss factor for i=j, and $\mathrm{Re}\{Z_{ij} \langle U_i^* U_j \rangle\}$ as the power flow from subsystem i to subsystem j. Eqs. V.7 are of a form that may be termed a "deterministical energy analysis", that is, a linear set of equations relating input power to degree of freedom, or subsystem, energy,

$$[\beta]\vec{E} = \vec{P} \tag{V.8}$$

or equivalently

$$\omega[\eta]\vec{E} = \vec{P} \ . \tag{V.9}$$

The rank of the matrix $[\eta]$ in Eq. V.9 is that of [Z] in Eq. V.1 and the two matrices require the same system parameters for their determination. Thus obtaining power flow from the solution to Eq. V.9 is similar in difficulty to obtaining the solution to Eq. V.1.

Statistical energy analysis (SEA) offers an alternate approach to arriving at an energy formulation of the type represented by Eq. V.9. The basis for the approach is that "the systems being studied are presumed to be drawn from statistical populations having known distributions of their dynamical properties (Refs. 7,12). Advantages of SEA are that for structural-acoustic problems amenable to this formulation (i) it is often insightful, (ii) the rank of the resulting matrix $[\eta]$ is reduced considerably and (iii) the determination of the elements in the matrix requires less precise input data than is typically required for a deterministic formulation. A disadvantage of SEA is that, in practice, the reduction in scale (rank) imposes the restriction that the magnitude of the characteristic wavelengths comprising the response of SEA system components, or subsystems, be small relative to their characteristic dimensions. For this reason SEA has been described as a "higher order modal analysis" (Refs. 12, 13).

In this study, as analytical work progressed a judgment was made to emphasize deterministic techniques, with SEA used in a supportive or ancillary role. The reason was as follows (i) by and large the deterministic solutions, although requiring extensive computations, could be exercised over the full frequency range of interest, (ii) the deterministic models revealed significant structure-borne noise propagation mechanisms that do not satisfy the "high mode order" requirements of SEA for the parameters under consideration, in particular compressional wave motion in the fuselage, and (iii) an extensive measurement program for determining loss factors, both dissipation and coupling, required for a detailed SEA could not be justified at this point.

As a result SEA techniques were used to:

1. develop an analysis of the power flow along the spars and ribs of the Beechcraft Baron wing to supplement deterministic models,

2. develop a crude global model of the power flow relationships for a wing-fuselage-cabin system for the purposes of gaining insight into critical parameters and grossly estimating noise levels as a check on both measurements and more detailed analyses, and

3. examine the feasibility of combining SEA and finite element techniques for estimating more accurate coupling loss factors of stiffened skin structures.

Item 1 is presented in Ref. 10 as are some details of item 2. These details are summarized in the section below where additional results regarding item 2 are presented. The importance of compressional waves in fuselage structures to the computation of cabin noise levels is described in Appendix G.

B. A Global SEA for Structureborne Induced Cabin Noise

In Section B of Ref. 14 SEA techniques are used to construct an expression for the noise levels generated in an aircraft cabin for a specified power injected into a wing, assuming a five subsystem model. This expression is

$$\langle\tilde{E}_c\rangle \equiv \langle E_c\rangle/(\Pi^i_{ws}/\omega)$$

$$= \frac{\eta_{f,c}}{(\eta_c+\eta_{c,f})} \cdot \frac{\eta_{w,f}}{(\eta_w+\eta_{w,f})} \cdot \frac{1}{\eta_f+\dfrac{\eta_c\eta_{f,c}}{\eta_c+\eta_{c,f}}+\dfrac{2\eta_w\eta_{f,w}}{\eta_w+\eta_{w,f}}} \qquad (V.10)$$

with

$$\langle P^2_c\rangle = \langle E_c\rangle\rho c^2/V \qquad (V.11)$$

where η_i and η_{ij} are the dissipation and coupling loss factors, subscripts c, f, and w refer to the cabin, fuselage and wing respectively, V is the cabin volume, and ρ and c are the air density and sound speed. Measurements of the dissipation loss factors are presented in Fig. 15.1* and an expression for the structural-acoustic coupling loss factor between the fuselage and cabin is given by Eq. 15.III.2.

For power injected directly into the fuselage in the absence of wings Eq. V.10 reduces to

$$\langle\tilde{E}_c\rangle \simeq \frac{\eta_{f,c}}{(\eta_c+\eta_{c,f})} \cdot \frac{1}{\eta_f+\dfrac{\eta_c\eta_{f,c}}{\eta_c+\eta_{c,f}}} . \qquad (V.12)$$

Assuming high damping,

$$\langle\tilde{E}_c\rangle \simeq \frac{\eta_{f,c}}{\eta_c\eta_f} \quad ; \quad \eta_f \gg \eta_{f,c} , \ \eta_c \gg \eta_{c,f} \qquad (V.13)$$

On the other hand, if we continue to ignore the effects of power coupling back from the cabin to the fuselage ($\eta_{c,f} \ll \eta_c$) but now assume low fuselage damping in Eq. V.12 we obtain

---

[*] Figure and equation numbers preceeded by the number 15 refer to Ref. 15.

$$\langle\tilde{E}_c\rangle \approx 1/\eta_c \quad ; \quad \eta_f \ll \eta_{f,c},\ \eta_c \gg \eta_{c,f} \tag{V.14}$$

An analytical estimate for the coupling loss factor $\eta_{f,c}$ may be obtained by modelling the fuselage as a framed panel vibrating in flexure (Ref. 15)

$$\eta_{f,c} \sim (3.6/\pi^2)\alpha/(\beta k_f d) \tag{V.15}$$

where α and β are the density and sound speed ratios between the surrounding air and the fuselage material (aluminum), k_f is the flexural wavenumber and d the fuselage frame spacing.

For the problem at hand, taking η_f=.03 from Fig. 15.1 and approximating the cabin volume, fuselage skin thickness and frame spacing by 8.6 x 10^5 cm^3, 0.1 cm and 25 cm respectively, we estimate $\eta_f/\eta_{f,c}=2.08 \times 10^2/(f(\text{kHz}))^{1/2}$ and thus Eq. V.13 prevails for all frequencies of interest.

A reasonably good comparison between results computed using Eq. V.13 and corresponding data is shown in Fig. 15.5. Also, noting that predictions using Eq. V.14 turn out to be in excess of 20 dB higher than those predicted by Eq. V.13, it is concluded that the Baron fuselage structure as designed appears to be an inefficient structural-acoustic transducer.

Now let us consider the more general case for which power is injected along the wing. Again ignoring cabin pressure induced fuselage vibrations ($\eta_{c,f} \ll \eta_c$) Eq. V.10 becomes

$$\langle E_c\rangle = \frac{\eta_{f,c}}{\eta_c}\,\frac{\eta_{w,f}}{(\eta_w+\eta_{w,f})}\cdot\frac{1}{\eta_f+\eta_{f,c}+\dfrac{2\eta_w\eta_{f,w}}{\eta_w+\eta_{w,f}}}\ . \tag{V.16}$$

If we further assume heavy damping in the wing and fuselage structures Eq. V.16 reduces to

$$\langle\tilde{E}_c\rangle \approx \frac{\eta_{f,c}\eta_{w,f}}{\eta_c\eta_w\eta_f} \quad ; \quad \eta_w \gg \eta_{w,f}\ ,\ \eta_f \gg \eta_{f,c}, \eta_{f,w} \tag{V.17}$$

Thus, damping of each of the subsystems is equally effective. On the other hand for strong coupling between the wing and fuselage we obtain

$$\langle \tilde{E}_c \rangle \simeq \frac{\eta_{f,c}}{\eta_c} \frac{1}{\eta_f + 2\eta_w(\eta_{f,w}/\eta_{w,f})} \qquad \eta_f >> \eta_{f,c},\ \eta_{w,f} >> \eta_w \qquad \text{(V.18)}$$

As indicated earlier (see Section V.A and Appendix G) detailed analyses of certain coupling loss factors for the Baron aircraft were judged to be infeasible using conventional SEA techniques and assumptions and were not pursued. Specifically this was the case for the coupling between the wings and fuselage. As an alternative for present purposes, these factors were estimated from measurements of wing and fuselage drive point accelerance data taken at the interface bolts. Required are the magnitude and phase of the accelerances (or admittances) and the implied modal density of the subsystems, as shown in Eq. 15.16. These accelerances have been presented earlier in Sections II and III. Based on these data the modal densities, defined by the number of accelerance peaks per frequency bandwidth, have been determined and are tabulated below in Table V.1.

TABLE V.1

FUSELAGE AND WING (INVERSE) MODAL DENSITIES

Frequency Band	Inverse Modal Density (Hz/modes)							
	wing				fuselage			
	x	y	z	avg	x	y	z	avg
500-1000 Hz	16	19	17	17	12	18	12	14
750-1000 Hz	15	18	19	17	17	13	13	14

The resulting coupling loss factors $\eta_{w,f}$ along the x and z axes are graphed in Fig. V.1. (The measured phase of the drive point admittances along the y (i.e., spanwise) axis is unreliable, implying negative input power over wide frequency bands, and therefore only the x and z axes are considered.) Although not required here the loss factor $\eta_{f,w}$ may be estimated from Fig. V.1 and Table V.1 using the reciprocal relationship $\eta_{f,w}/\eta_{w,f}=N_w/N_f$ where N_w and N_f are the wing and fuselage modal densities respectively. It is observed that the loss factors along the two axes tend to come together at the higher frequencies, say above 750 Hz. Also, referring to Fig. 15.1 $\eta_{w,f}<\eta_w$ and therefore the heavy damping assumption upon which Eq. V.17 is based appears appropriate. A comparison between cabin noise predictions using Eq. V.17 and measurements is shown in Fig. V.2. The measurements were taken with a drive located on the engine mount structure as shown in Fig. 7a of Ref. 2. The gaps shown in the data correspond to frequency bands within which the input power measured at the drive was negative. The average of the coupling loss factors in the x and z directions was used to construct the predicted curve. Predictions underestimate the measured levels by roughly 10 dB or less on average. We also note that the measured high frequency noise levels in the cabin normalized to input power for an engine mount drive is, on average, roughly 5-10 dB down from those for a drive directly on the fuselage at a wing connect bolt, while the predicted difference is roughly 15 dB. (One must subtract 84 dB to account for a normalization change from dB re $(20\ \mu\text{Pa})^2/1$ lb-in/sec in Fig. 15.5 to dB re: 1 N-sec/m^5 in Fig. V.2.) Thus we see that accepting 10 dB as a criterion, even the crudest of SEA models may yield useful high frequency estimates. In many instances, improvements in accuracy are clearly possible with more detailed SEA modelling and extensive measurements (Refs. 17, 18). However it may be that, in some cases, favorable comparisons with measurements mask fundamental limitations of this technique to capture all significant structureborne noise mechanisms and in turn to predict the effectiveness of changes in structure or the addition of noise control features.

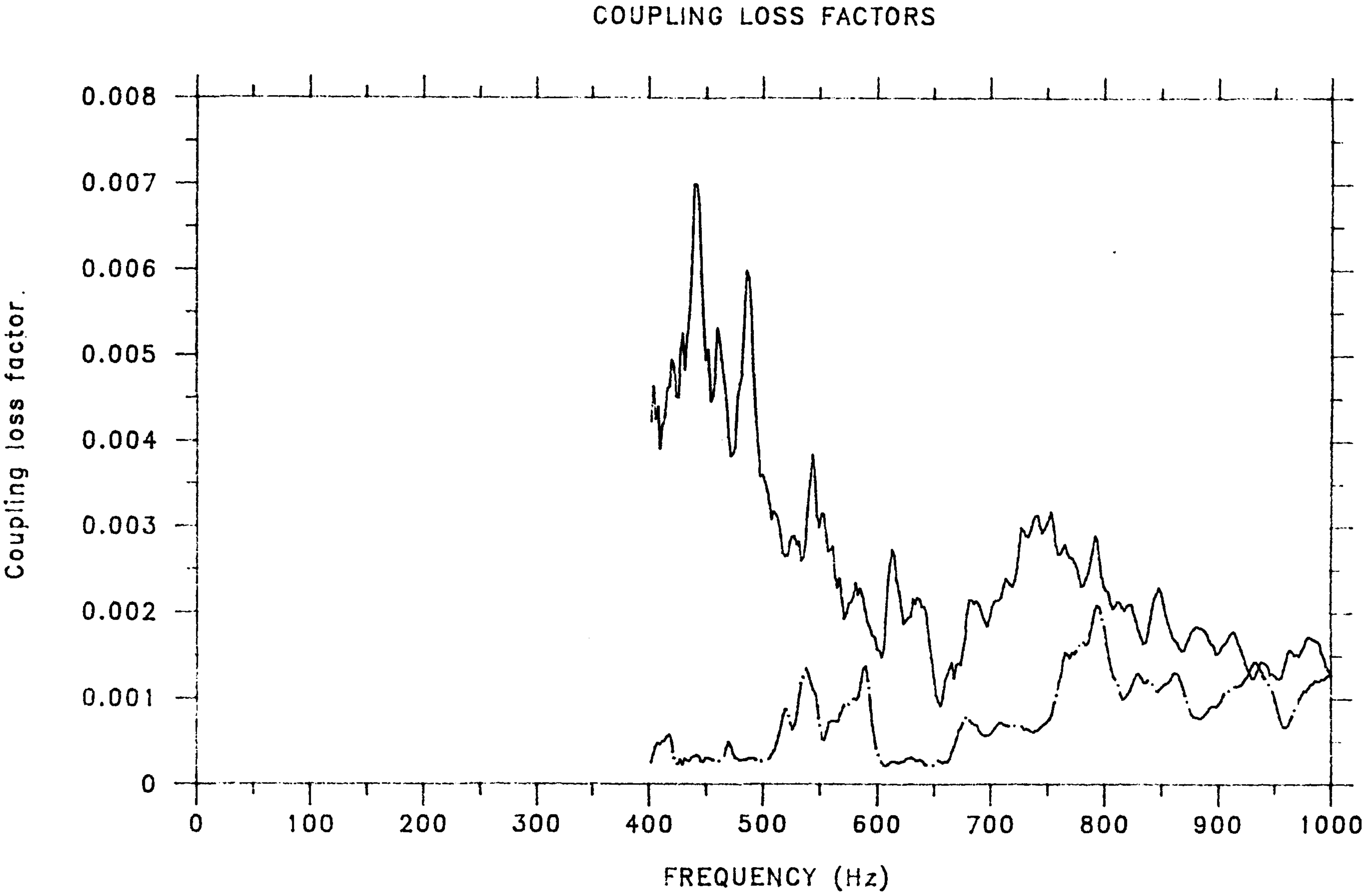

Fig. V.1 Wing to fuselage coupling loss factors ($\eta_{w,f}$) along the z(——) and x (—·—) axes computed from drive point impedance measurements at a wing connect bolt location.

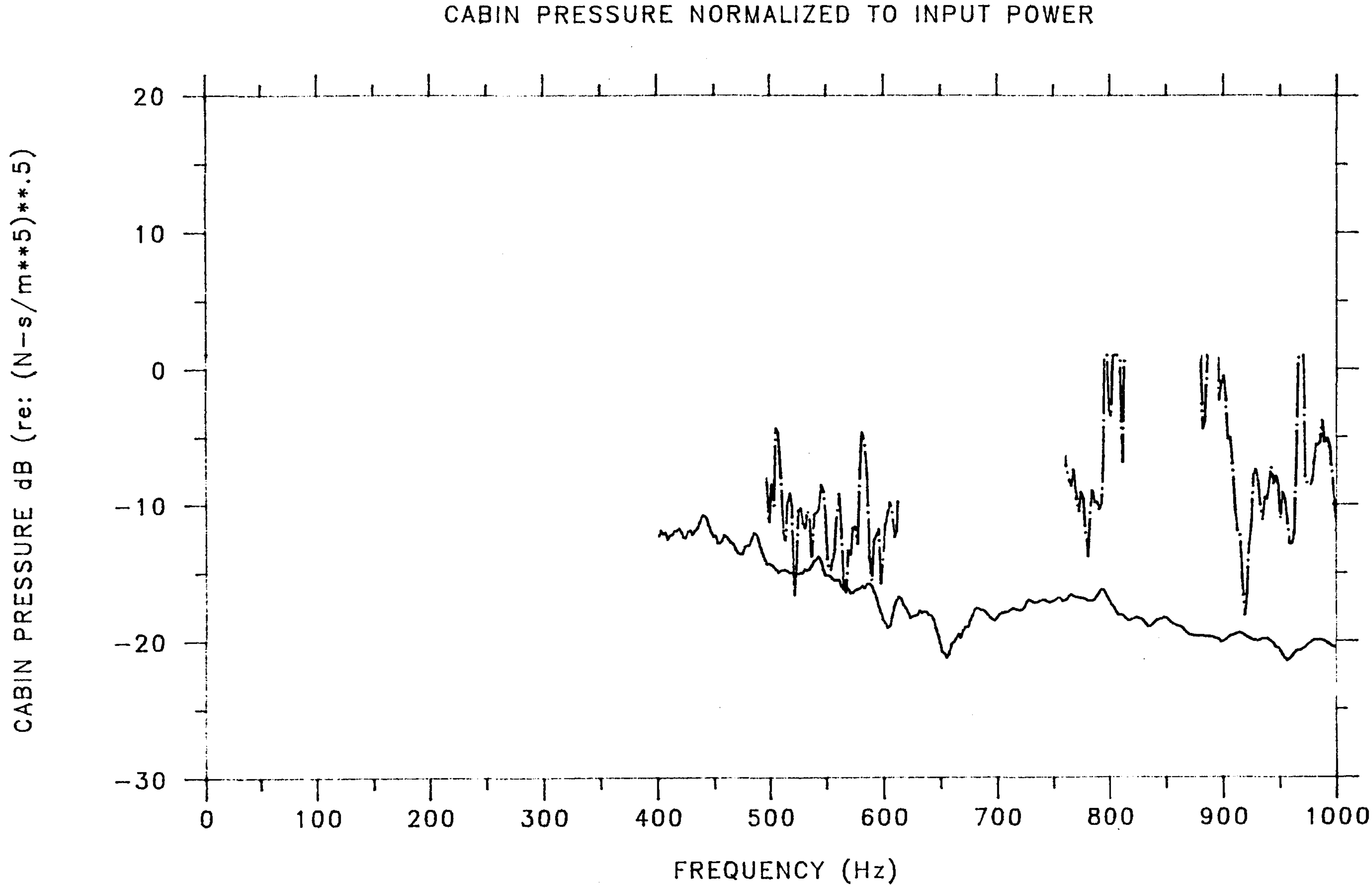

Fig. V.2 SEA predicted (——) and measured (——·——) cabin noise levels normalized to input power for an engine support structure drive location.

VI. CONCLUSIONS

Although modeling approaches used in this analytical study are reasonably general, specific calculations have been made to compare with measurements taken on the Beechcraft Baron which served as a test bed for this study. The establishment of models and parameters that give reasonable agreement with the data has permitted studies to be made to examine the sensitivity of the calculated results to a number of parameters appearing in the models. Based on these results, the following conclusions are drawn:

A. Wing

1. Results of the finite element model of the wing are in good agreement with measurements in terms of mean responses.

    (a) The finite element modeling is robust with respect to achieving the fundamental bending and torsional modes, in the sense that various modeling assumptions give similar fundamental resonance modes.

    (b) Certain features of the measurements are not captured by the modeling; these being wing resonances in the 65-75 Hz range.

2. Drive-point and transfer responses of the freely-supported wing are lowered by 10-15 dB over most of the frequency range (i.e., up to 200 Hz) with the addition of approximately 200 pounds of simulated fuel in the inboard tank locations. This is consistent with measurements (Ref.2) and suggests that fuel can have an important effect on interior noise levels.

3. Results for the wing are found to be sensitive to simulated damage to portions of the wing skin. A decrease in the membrane stiffness of the skin significantly lowers the resonance frequencies of the modes above the fundamental bending and torsion. Although this result primarily relates to the specific wing tested in the laboratory, it suggests a possible sensitivity to static deflection of the wing such as that imposed by steady lift loads in flight.

B. Fuselage and Cabin Space

1. Calculated results averaged over one-third octave bands for both structural and acoustic responses of the fuselage model are found to be in reasonable agreement with measurements.

2. Over most of the frequency range up to 1 kHz, the fuselage and cabin space response are insensitive to a number of structural parameters including stringer stiffness and the presence of non-driven circumferential frames. The likely reason for this result is the relatively small dimensions of the structure in terms of structural and acoustic wavelengths.

3. Reductions of approximately 5 dB in cabin acoustic pressure over frequencies from 50-1000 Hz are obtained when the structural damping is increased by an order-of-magnitude above its nominal measured value. This suggests that the interior acoustic pressure field has a significant contribution from structural vibrations away from the wing-fuselage interface (i.e., from the "propagating" structural field).

4. Reductions of approximately 5 dB in cabin acoustic pressure are also obtained above 200 Hz by increasing the thickness of the acoustically absorptive liner by a factor of four.

C. Interface of Fuselage and Wing Models

1. Results for the cabin acoustic pressure are found to be sensitive to the extent to which there is "impedance" matching between the structural responses of the wing and fuselage in each of the degrees-of-freedom. Differences in cabin pressure of approximately 8 dB on average are found when the wing is attached to rear horizontal diameter of the fuselage compared to an attachment at the bottom of the fuselage. This sensitivity emphasizes the importance of structural attachment details on interior noise (e.g., the role of isolators) and suggests the ability to create structural mismatches over a range of frequencies through careful dynamic structural design.

2. Based on a statistical energy analysis of the global structure, the cabin pressure should be equally altered by changes in the loss factor of any subsystem of the Baron (viz., wing, fuselage, or cabin space).

REFERENCES

1 R. Martinez, "Predictions of Unsteady Wing and Pylon Forces Caused by Propeller Installation," NASA CR-172898 (May 1987).

2 J.E. Cole III and K. Martini, Structureborne Noise Measurements on a Small Twin-Engine Aircraft, NASA CR-4137, 1988.

3 A.D. Pierce, Acoustics, An Introduction to its Physical Principles and Applications, (McGraw-Hill Book Company, NY, 1981) pp. 140-143.

4 Baron Illustrated Parts Catalog, Volume 2 (Beech Aircraft Corp. Wichita,Kansas, 1983).

5 M.C. Junger, "The Sound Field in a Finite Cylindrical Shell," J. Acoust. Soc. Am., 77 (1985) 1610-1612.

6 V.V. Mukzychenko, A.P. Paniklenko, and S.A. Rybak, "Dispersion Curves for Normal Modes in Cylindrical Shell and Conditions for Spatial Coincidence in the Vicinity of the Critical Frequencies," Sov. Phys. Acoust., 30 (1984) 47-51.

7 L. Cremer and M. Heckl, Structure-Borne Sound (E.E. Ungar, Trans. Springer-Verlag, NY, 1973) 260-269.

8 Cosmic NASTRAN Theoretical Manual, (Cosmic, the University of Georgia, Athens, GA) pg. 15.3-1.

9 C.M. Harris and C.E. Crede (Ed), Shock and Vibration Handbook, (McGraw-Hill Book Co., NY, 1961), Chapter 7.

10 R. Martinez, et al, "All-theoretical Prediction of Cabin Noise Due to Impingement of Propeller Vortices on a Wing Surface," (No. AIAA-87-2681, presented at the 11th AIAA Aeroacoustics Specialists Conference, Sunnyvale, CA, October 1987).

11 R.E. Hayden et al, A Study of Interior Noise Levels, Noise Sources and Transmission Paths in Light Aircraft, NASA CR-172152 (July 1983) Appendix A.

References Continued

12 Richard H. Lyon, "Statistical Energy Analysis of Dynamical Systems: Theory and Applications," The MIT Press, Cambridge, 1975.

13 P.W. Smith, Jr., "Concepts and Applications of SEA," 97th Meeting of the Acoust. Soc. Am., Cambridge, MA, June 1979.

14 J.M. Garrelick, et al, "Structureborne Noise Investigations of a Twin Engine Aircraft," (No. AIAA-86-1905 presented at the 10th AIAA Aeroacoustics Specialists Conference, Seattle, WA, July 1986.)

15 G. Madanik, "Response of Ribbed Panels to Reverberant Acoustic Fields," J. Acoust. Soc. Am. 34, 807-826, 1962.

16 C.A. Yoerkie et al, "Development of Rotorcraft Interior Noise Control Concepts, Phase I: Definition Study," NASA-CR-166101, May 1983.

17 C.A. Yoerkie et al, "Development of Rotorcraft Interior Noise Control Concepts, Phase II: Full Scale Testing," NASA CR 172594, February 1986.

18 A.W. Leissa, Vibrations of Shells, (National Aeronautics and Space Administration, NASA SP-288, 1983) 185-191.

19 A. Harari, "Wave Propagation in Cylindrical Shells with Finite Regions of Structural Discontinuity," J. Acoust. Soc. Am., 62 (1977) 1196-1205.

20 M.C. Junger and D. Feit, Sound, Structures, and Their Interaction, 2nd Ed. (MIT Press, Cambridge, MA, 1986) 168-173.

21 M.E. Delany and E.N. Bazley, "Acoustical Properties of Fibrous Absorbent Materials," Applied Acoustics, 2 (1970) 105-116.

22 A. Papoulis, The Fourier Integral and Its Applications, (McGraw-Hill Book Co., NY, 1962) 27-28.

APPENDIX A

ANALYSIS OF FRAME-STIFFENED ORTHOTROPIC CYLINDRICAL SHELL CONTAINING FLUID

APPENDIX A

ANALYSIS OF FRAME-STIFFENED ORTHOTROPIC CYLINDRICAL SHELL CONTAINING FLUID

The vibrations of a cylindrical shell of length L, radius a, and thickness h are governed by three coupled linear equations, each equation describing the dynamics in one of the principal directions (viz., radial, circumferential, axial). This set of equations may be expressed

$$L_1u+L_2v+L_3w = \frac{a^2(1-\nu^2)}{Eh}\,p_x$$

$$L_4u+L_5v+L_6w = \frac{a^2(1-\nu^2)}{Eh}\,p_\phi$$

$$L_7u+L_8v+L_9w = \frac{a^2(1-\nu^2)}{Eh}\,p_r \qquad (A.1)$$

where L_i are the linear shell operators derived by the appropriate shell theory, ν is the Poisson ratio for the material and all loads acting on the shell appear on the right-hand side. Loading on the shell due to the surrounding fluid which is assumed to occur in the radial direction only (i.e., viscous effects are neglected) can be represented as a separate load

$$p_r\Big|_{\text{fluid}}=p_f(x,a,\phi) \qquad (A.2)$$

For the purposes of modeling the fuselage we choose to incorporate circumferential stiffeners as discrete frames and to add the stiffening effect of the axial stringers as an equivalent orthotropic material property. The effect of the stringers is included by using the orthotropic shell equations of Mikulas and McElman given in Ref. 18, these equations being written in terms of stringer parameters and spacing. The circumferential stiffeners are modeled as structural rings that are assumed to impart loads in all three directions along a circumferential line around the shell. These loads are expressed as follows:

$$p_x = \sum_{i=1}^{N_f} p_x^i(\phi)\,\delta(x-x_i)$$

$$p_\phi = \sum_{i=1}^{N_f} p_\phi^i(\phi)\,\delta(x-x_i)$$

$$p_r = \sum_{i=1}^{N_f} \left(p_r^i(\phi) - \frac{\partial M_\phi^i}{\partial x}\right)\delta(x-x_i) \qquad \text{(A.3)}$$

where p_j^i is the load per unit area in the jth direction located at x_i, N_f is the number of frames, M_ϕ is the twisting moment per unit area with axis in the circumferential direction (see Fig. A.1), and δ is the Dirac delta function.

Under the assumption of shear diaphragm boundary conditions for the shell, the shell displacements and loads are expanded in the following Fourier series:

$$u(x,\phi) = \sum_n \sum_m u_{nm} \cos n\phi \cos k_m x$$

$$v(x,\phi) = \sum_n \sum_m v_{nm} \sin n\phi \sin k_m x$$

$$w(x,\phi) = \sum_n \sum_m w_{nm} \cos n\phi \sin k_m x$$

$$p_x^i(\phi)\,\delta(x-x_i) = \sum_n \sum_m p_{xnm}^i \cos n\phi \cos k_m x$$

$$p^i(\phi)\,\delta(x-x_i) = \sum_n \sum_m p_{\phi nm}^i \sin n\phi \sin k_m x$$

$$p_r^i(\phi)\,\delta(x-x_i) = \sum_n \sum_m p_{rnm}^i \cos n\phi \sin k_m x$$

$$M^i(\phi)\,\delta(x-x_i) = \sum_n \sum_m M_{\phi nm}^i \cos n\phi \cos k_m x \qquad \text{(A.4)}$$

where $k_m = m\pi/L$. Substitution of these expansions into Eq. A.1 and use of orthogonality of the modal functions results in the following set of modal equations:

$$\begin{bmatrix} A_1 & A_2 & A_3 \\ A_4 & A_5 & A_6 \\ A_7 & A_8 & A_9 \end{bmatrix} \begin{bmatrix} u_{nm} \\ v_{nm} \\ w_{nm} \end{bmatrix} = \frac{a^2(1-\nu^2)}{Eh} \begin{bmatrix} \sum_i p^i_{xnm} \\ \sum_i p^i_{\phi nm} \\ \sum_i (p^i_{rnm}+k_m M^i_{\phi nm}) \end{bmatrix} \tag{A.5}$$

where A_i's are the modal shell coefficients. The fluid loading given in Appendix B has the same modal form as (and is proportional to) the radial shell displacement. Consequently it is incorporated into coefficient A_9.

Eq. A.5 can be inverted to express the shell displacements in terms of the applied loads,

$$u_{nm} = \frac{a^2(1-\nu^2)}{Eh} \sum_i \{B_1 p^i_{xnm} + B_2 p^i_{\phi nm} + B_3 (p^i_{rnm} + k_m M^i_{\phi nm})\}$$

$$v_{nm} = \frac{a^2(1-\nu^2)}{Eh} \sum_i \{B_4 p^i_{xnm} + B_5 p^i_{\phi nm} + B_6 (p^i_{rnm} + k_m M^i_{\phi nm})\}$$

$$w_{nm} = \frac{a^2(1-\nu^2)}{Eh} \sum_i \{B_7 p^i_{xnm} + B_8 p^i_{\phi nm} + B_9 (p^i_{rnm} + k_m M^i_{\phi nm})\} \tag{A.6}$$

where B_i are the matrix entries of the inverse of matrix A. Because the discrete stiffeners only couple to circumferential modes of the shell, the shell amplitudes in Eq. A.6 are summed over all axial modes,

$$u_n(x) = \frac{2a^2(1-\nu^2)}{EhL} \sum_{i=1}^{N_f} \{p^i_{xn} \sum_m B_1 \cos k_m x_i \cos k_m x + p^i_{\phi n} \sum_m B_2 \sin k_m x_i \cos k_m x$$

$$+ p^i_{rn} \sum_m B_3 \sin k_m x_i \cos k_m x + M^i_{\phi n} \sum_m B_3 k_m \cos k_m x_i \cos k_m x\}$$

$$v_n(x) = \frac{2a^2(1-\nu^2)}{EhL} \sum_{i=1}^{N_f} \{p^i_{xn} \sum_m B_4 \cos k_m x_i \sin k_m x + p^i_{\phi n} \sum_m B_5 \sin k_m x_i \sin k_m x$$

$$+ p^i_{rn} \sum_m B_6 \sin k_m x_i \sin k_m x + M^i_{\phi n} \sum_m B_6 k_m \cos k_m x_i \sin k_m x\}$$

$$w_n(x) = \frac{2a^2(1-\nu^2)}{EhL} \sum_{i=1}^{N_f} \{p^i_{xn} \sum_m B_7 \cos k_m x_i \sin k_m x + p^i_{\phi n} \sum_m B_8 \sin k_m x_i \sin k_m x$$

$$+ p^i_{rn} \sum_m B_9 \sin k_m x_i \sin k_m x + M^i_{\phi n} \sum_m B_9 k_m \cos k_m x_i \sin k_m x\}$$

$$M^i_{\phi nm} = \frac{2}{L\varepsilon_m} M^i_{\phi n} \cos k_m x_i \qquad \text{(A.7)}$$

In this form the relationship between modal loading coefficients is given as follows:

$$p^i_{xnm} = \frac{2p^i_{xn} \cos k_m x_i}{L\varepsilon_m}$$

$$p^i_{\phi nm} = \frac{2p^i_{\phi n}}{L} \sin k_m x_i$$

$$p^i_{rnm} = \frac{2}{L} p^i_{rn} \sin k_m x_i$$

$$M^i_{\phi nm} = \frac{2}{L\varepsilon_m} M^i_{\phi n} \cos k_m x_i \qquad \text{(A.8)}$$

where

$$p^i_{xn} = \frac{1}{\pi\varepsilon_n} \int_0^{2\pi} p^i_x(\phi) \cos n\phi \, d\phi$$

$$p^i_{\phi n} = \frac{1}{\pi} \int_0^{2\pi} p^i_\phi(\phi) \sin n\phi \, d\phi$$

$$p^i_{rn} = \frac{1}{\pi\varepsilon_n} \int_0^{2\pi} p^i_r(\phi) \cos n\phi \, d\phi$$

$$M^i_{\phi n} = \frac{1}{\pi\varepsilon_n} \int_0^{2\pi} M^i(\phi) \cos n\phi \, d\phi$$

where

$$\varepsilon_k = \begin{cases} 2 & ; \quad k=0 \\ 1 & ; \quad k>0 \end{cases}$$

In this form the shell coefficients in each circumferential mode are expressed in terms of the unknown loadings applied to the shell at locations x_i. The nature of the loadings depends on the structural characteristics of the frame stiffener. A simple model of a circumferential stiffener is that of a uniform ring (see Ref. 19). In this model radial and circumferential motions are coupled and are independent of coupled axial and twisting rotational motions. The impedances for a ring from Ref. 19 are given in Appendix D. Because the cross-section of the frame rotates as a rigid body in this model, a modification for "tee" frames has been made to reduce the rotational stiffness by permitting flexural motion of the web. This modification has been used in the present model.

At the interface between shell and frame, conditions of displacement continuity and force equality are imposed. This permits the net loads acting on the ring to be expressed in terms of the frame compliances and the shell displacements.

$$p_{rn} = Z^I_{11} w_n + Z^I_{13} v_n$$

$$p_{xn} = Z^I_{22} u_n - aZ^I_{24} w_{xn}$$

$$p_{\phi n} = Z^I_{31} w_n + Z^I_{33} v_n$$

$$M_{\phi n}/a = Z^I_{42} u_n - aZ^I_{44} w_{xn} \qquad \text{(A.9)}$$

where $w_x \equiv \partial w/\partial x$, and the superscript I denotes a specific frame. The net loads can then be expressed as frame reaction and applied loads (superscript a) as follows:

$$\left.\begin{aligned} p_{rn} &= p_{rn}^{a} - p_{rn}^{I} \\ p_{xn} &= p_{xn}^{a} - p_{xn}^{I} \\ p_{\phi n} &= p_{\phi n}^{a} - p_{\phi n}^{I} \\ M_{\phi n} &= M_{\phi n}^{a} - M_{\phi n}^{I} \end{aligned}\right\} \quad x = x_I \tag{A.10}$$

For rings that are not directly excited the applied loads are zero.

Substitution of the shell displacements from Eq. A.7 into the boundary conditions at each frame location (Eqs. A.9, A.10) leads to a set of simultaneous equations for the frame reaction loads. This set of equations can be expressed compactly as

$$\sum_{i=1}^{N_f} \{\alpha_{iI}^{j} p_{xn}^{i} + \beta_{iI}^{j} p_{\phi n}^{i} + \gamma_{iI}^{j} p_{rn}^{i} + \xi_{iI}^{j} M_{\phi n}^{i}\} + \zeta(p_{rn}^{I}\delta_{j1} + p_{xn}^{I}\delta_{j2} + p_{\phi n}^{I}\delta_{j3} - M_{\phi n}^{I}\delta_{j4}/a) = f_{jI} \quad ; \quad j = 1,4 \tag{A.11}$$

at $x = x_I$ where

$$\delta_{k\ell} = \begin{cases} 0 & ; \quad k \neq \ell \\ 1 & ; \quad k = \ell \end{cases}$$

The coefficients of this set of equations are given in Appendix C.

Since there are four ring reactions for each ring, the order of the coefficient matrix is $4N_f$. The response for each value of n at any point is obtained by substitution of the calculated reactions into Eqs. A.7, and the total response is obtained by multiplying by

$$\left\{\begin{matrix} \cos n\phi \\ \sin n\phi \end{matrix}\right\}$$

and summing over index n.

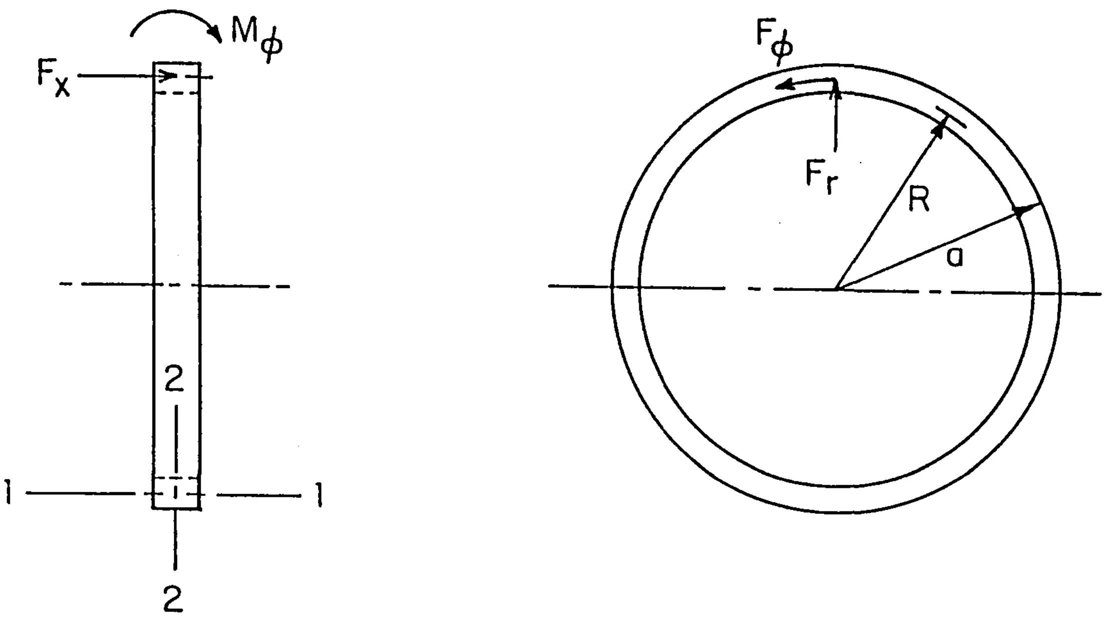

Fig. A.1 Geometry of circumferential frame.

APPENDIX B

FLUID LOADING ON SHELL

APPENDIX B

FLUID LOADING ON SHELL

The pressure generated on the internal surface of a cylindrical shell having simple supports at x=0 and L in response to a radial mode (i.e., $\sin k_m x \cos n\phi$) is given by

$$p^i_{nm}(x,a,\phi) = -i\omega w^i_{nm} Z^i_{nm} \sin k_m x \cos n\phi \qquad \text{(B.1)}$$

where

$$Z^i_{nm} = \begin{cases} -i\rho^i\omega \dfrac{J_n(\alpha_m a)}{\alpha_m J'_n(\alpha_m a)} \; ; \; \alpha_m (\equiv \sqrt{k_i^2 - k_m^2 a}) \text{ real} \\ \\ -i\rho^i\omega \dfrac{I_n(|\alpha_m| a)}{|\alpha_m| I'_n(|\alpha_m| a)} \; ; \; \alpha_m = \text{imaginary} \end{cases}$$

where $k_i=\omega/c_i$ is the acoustic wavenumber of the internal fluid, c_i is the second speed of the internal fluid, w^i_{mn} is the fluid modal amplitude, and J_n and I_n are the Bessel functions or order n of the first and second kinds, respectively. The sign convention adopted is positive outward displacement. Because these Bessel functions are real-valued, the internal fluid reacts as either a mass or a stiffness. The acoustic pressure for each mode vanishes at the axial locations of the simple supports.

The pressure field at any internal radial position is obtained by replacing the shell radius in the argument of the function in the numerator of Z^i_{nm} by r ($r \le a$), multiplying by $\sin k_m x \cos n\phi$, and summing over indices m and n. For subsonic structural wavenumbers (i.e., $k_m > k_i$) the pressure field decays away from the cylindrical surface for all modes.

The modal pressure acting on the exterior surface of the shell is given by

$$p^e_{nm}(x,a,\phi) = i\omega w^e_{nm} Z^e_{nm} \sin k_m x \cos n\phi$$

where

$$z^e_{nm} = \begin{cases} -i\rho^e\omega \dfrac{H_n(\alpha_m a)}{\alpha_m H'_n(\alpha_m a)}; & \alpha_m (\equiv\sqrt{k_e^2-k_m^2}a) \text{ - real} \\ -i\rho^e\omega \dfrac{K_n(|\alpha_m| a)}{|\alpha_m| K'_n(|\alpha_m| a)}; & \alpha_m = \text{imaginary} \end{cases} \quad \text{(B.2)}$$

where H_n and K_n are Hankel functions of the first and second kinds, $k_e=\omega/c_e$, c_e is the sound speed in the external fluid, and w^e_{nm} is the modal amplitude of the exterior fluid. Mass-like loading on the shell is obtained for subsonic structural wavelengths (i.e., $k_m>k_e$). The Hankel functions of the first kind are complex-valued and give rise to loadings behaving as both mass and resistance when the structural wavelengths are supersonic (see Ref. 20). Once again the modal pressure at any radial location outside the shell is obtained by replacing a by r ($r \geq a$) in the function in the numerator. The summation over modes described above is used to evaluate the total pressure at any location given the shell modal amplitudes.

When the surface of the shell is directly in contact with the fluid (i.e., a bare shell), the modal amplitude of the shell is that of the fluid, that is,

$$w_{mn} = w^i_{mn} = w^e_{mn} \quad \text{(B.3)}$$

This compatability is not maintained in the presence of an acoustic liner. As discussed in Appendix E, the interior of the fuselage shell is assumed to be lined with a locally reacting acoustic layer. The ratio of displacements across the layer given by Eq. E.4 is

$$\frac{w^i_{nm}}{w_{nm}} \equiv \frac{v_f}{v_b} = \frac{1-i\dfrac{\omega}{K_\ell}Z_b}{1+\dfrac{i\omega}{K_\ell}Z_f} \quad \text{(B.4)}$$

APPENDIX C

COEFFICIENTS OF EQUATIONS RESULTING FROM BOUNDARY CONDITIONS

APPENDIX C

COEFFICIENTS OF EQUATIONS RESULTING FROM BOUNDARY CONDITIONS

The coefficients appearing in Eqs. A.11 for the ring located at $x = x_I$ are given as follows:

$$\alpha^1_{iI} = \frac{2}{L} \sum_m (B_7 Z^I_{11} + B_4 Z^I_{13}) \cos k_m x_i \sin k_m x_I / \varepsilon_m$$

$$\alpha^2_{iI} = \frac{2}{L} \sum_m (B_1 Z^I_{22} - a k_m B_7 Z^I_{24}) \cos k_m x_i \cos k_m x_I / \varepsilon_m$$

$$\alpha^3_{iI} = \frac{2}{L} \sum_m (B_7 Z^I_{31} + B_4 Z^I_{33}) \cos k_m x_i \sin k_m x_I / \varepsilon_m$$

$$\alpha^4_{iI} = \frac{2}{L} \sum_m (B_1 Z^I_{42} - a k_m B_7 Z^I_{44}) \cos k_m x_i \cos k_m x_I / \varepsilon_m$$

$$\beta^1_{iI} = \frac{2}{L} \sum_m (B_8 Z^I_{11} + B_5 Z^I_{13}) \sin k_m x_i \sin k_m x_I$$

$$\beta^2_{iI} = \frac{2}{L} \sum_m (B_2 Z^I_{22} - a k_m Z^I_{24} B_8) \sin k_m x_i \cos k_m x_I$$

$$\beta^3_{iI} = \frac{2}{L} \sum_m (B_8 Z^I_{31} + B_5 Z^I_{33}) \sin k_m x_i \sin k_m x_I$$

$$\beta^4_{iI} = \frac{2}{L} \sum_m (B_2 Z^I_{42} - a k_m Z^I_{44} B_8) \sin k_m x_i \cos k_m x_I$$

$$\gamma^1_{iI} = \frac{2}{L} \sum_m (B_9 Z^I_{11} + B_6 Z^I_{13}) \sin k_m x_i \sin k_m x_I$$

$$\gamma^2_{iI} = \frac{2}{L} \sum_m (B_3 Z^I_{22} - a k_m B_9 Z^I_{24}) \sin k_m x_i \cos k_m x_I$$

$$\gamma^3_{iI} = \frac{2}{L} \sum_m (B_9 Z^I_{31} + B_6 Z^I_{33}) \sin k_m x_i \sin k_m x_I$$

$$\gamma^4_{iI} = \frac{2}{L} \sum_m (B_3 Z^I_{42} - a k_m B_9 Z^I_{44}) \sin k_m x_i \cos k_m x_I$$

$$\xi^1_{iI} = \frac{2}{L} \sum_m (B_9 Z^I_{11} + B_6 Z^I_{13}) k_m \cos k_m x_i \sin k_m x_I / \varepsilon_m$$

$$\xi^2_{iI} = \frac{2}{L} \sum_m (B_3 Z^I_{22} - a k_m B_9 Z^I_{24}) k_m \cos k_m x_i \cos k_m x_I / \varepsilon_m$$

$$\xi^3_{iI} = \frac{2}{L} \sum_m (B_9 Z^I_{31} + B_6 Z^I_{33}) k_m \cos k_m x_i \sin k_m x_I / \varepsilon_m$$

$$\xi^4_{iI} = \frac{2}{L} \sum_m (B_3 Z^I_{42} - a k_m B_9 Z^I_{44}) k_m \cos k_m x_i \cos k_m x_I / \varepsilon_m$$

$$\left.\begin{aligned} f_{1I} &= \zeta\, p^a_{rn} \\ f_{2I} &= \zeta\, p^a_{xn} \\ f_{3I} &= \zeta\, p^a_{\phi n} \\ f_{4I} &= \zeta\, M^a_{xn}/a \end{aligned}\right\} \quad ; \quad x = x_a$$

$$f_{1I} = f_{2I} = f_{3I} = f_{4I} = 0 \quad ; \quad x = x_I \neq x_a$$

$$\zeta = Eh/a^2(1-\nu^2)$$

APPENDIX D

IMPEDANCES OF A RING FRAME

APPENDIX D

IMPEDANCES OF A RING FRAME

The relationship between the forces and velocities acting at the outer surface of a ring are given by Harari (Ref. 19) who considers a right-hand coordinate system that is directed radially inwards and a time dependence proportional to $e^{i\omega t}$. If we orient the coordinate system so that the positive radial direction is outwards, and assume a time dependence proportional to $e^{-i\omega t}$, then the impedance matrix is given by $Z_{ij}=i\tilde{Z}_{ij}/\omega$ where

$$\tilde{Z}_{11} = \bar{E}\,\frac{R}{a}\left[n^4\,\frac{R}{a}\,\frac{I_1}{R^4} - n^2\,\frac{\Lambda}{R^2}\,\frac{d}{a} + \frac{\Lambda}{R^2} - \frac{\bar{\rho}}{\bar{E}}\,A\omega^2\right] \quad n\,\frac{d}{R}\,\tilde{Z}_{31}\;,$$

$$\tilde{Z}_{13} = \bar{E}\left(\frac{R}{a}\right)^2\left[n^3\,\frac{I_1}{R^4} + n\,\frac{\Lambda}{R^2}\right] \quad n\,\frac{d}{R}\,\tilde{Z}_{33}\;,$$

$$\tilde{Z}_{22} = \bar{E}\,\frac{R}{a}\left[\frac{I_2}{R^4}\,n^4 + n^2\,\frac{J}{R^4}\,\frac{\bar{G}}{\bar{E}} - \frac{\bar{\rho}}{\bar{E}}\,A\omega^2\right]\;,$$

$$\tilde{Z}_{24} = \bar{E}\,\frac{R}{a}\left[-n^4\,\frac{I_2}{R^4}\,\frac{d}{a} - n^2\left(\frac{I_2}{R^4}\,\frac{R}{a} + \frac{J}{R^4}\,\frac{\bar{G}}{\bar{E}}\right) + \frac{d}{a}\,\frac{\bar{\rho}}{\bar{E}}\,A\omega^2\right]\;,$$

$$\tilde{Z}_{31} = \bar{E}\left(\frac{R}{a}\right)^2\left[-n^3\left(\frac{\Lambda}{R^2}\,\frac{d}{a} - \frac{R}{a}\,\frac{I_1}{R^4}\right) + n\,\frac{\Lambda}{R^2} + n\,\frac{d}{a}\,\frac{\bar{\rho}}{\bar{E}}\,A\omega^2\right]\;,$$

$$\tilde{Z}_{33} = \bar{E}\left(\frac{R}{a}\right)^3\left[n^2\left(\frac{\Lambda}{R^2} + \frac{I_1}{R^4}\right) - \frac{\bar{\rho}}{\bar{E}}\,A\omega^2\right]\;,$$

$$\tilde{Z}_{42} = -\bar{E}\left(\frac{R}{a}\right)^2 n^2\left(\frac{I_2}{R^4} + \frac{J}{R^4}\,\frac{\bar{G}}{\bar{E}}\right) + \frac{d}{a}\,\tilde{Z}_{22}\;,$$

$$\tilde{Z}_{44} = \bar{E}\left(\frac{R}{a}\right)^2\left[n^2\left(\frac{I_2}{R^4}\,\frac{d}{a} + \frac{J}{R^4}\,\frac{\bar{G}}{\bar{E}}\right) + \frac{R}{a}\,\frac{I_2}{R^4} - \left(\frac{R}{a}\right)\frac{J}{R^2A}\,\frac{\bar{\rho}\Lambda}{\bar{E}}\,\omega^2\right] - \frac{d}{a}\,\tilde{Z}_{24}$$

The signs in terms $\tilde{Z}_{31}$ and $\tilde{Z}_{13}$ have been reversed from those given in Ref. 19 to account for the radial outward coordinate system. The dimensions of the ring are given in Fig. A.1, $\bar{E}$ and $\bar{G}$ are respectively the elastic and shear moduli of the ring material, $\bar{\rho}$ is the density of the ring, I_1 and I_2 are respectively the moment of inertia of the cross section about the in-plane and out-of-plane bending axis, J is the polar moment of inertia of the cross-section, and A is the cross-sectional area.

APPENDIX E

MODEL OF SOUND ABSORPTIVE LINER

APPENDIX E

MODEL OF SOUND ABSORPTIVE LINER

The analytical model of the absorptive liner along the fuselage wall is based on the lumped parameter representation of Ref. 3. This model assumes the liner to be locally reacting (i.e., non-wavebearing) and extends the representation of Ref. 3 to include the effects of liner stiffness.

The liner is idealized as a insulating blanket with specific flow resistance R_ℓ, mass per unit area M_ℓ, and stiffness K_ℓ. Assuming a pressure and velocity on the front and back sides of the liner given by P_f, v_f and P_b, v_b respectively, the following governing equations are used.

$$-i\omega M_\ell v_\ell = P_f - P_b \tag{E.1}$$

$$(v_f - v_b) = -\frac{i\omega}{K_\ell}(P_f + P_b) \tag{E.2}$$

$$\frac{1}{2}(v_f + v_b) - v_\ell = \frac{1}{R_\ell}(P_f - P_b) \tag{E.3}$$

The first equation is a statement of Newton's law for the liner matrix having a mean velocity v_ℓ, the second models the compressibility of the liner as a spring, and the third relates the mean flow through the liner to the specific flow resistivity. By letting the liner be infinitely stiff ($K_\ell \to \infty$), the result of Ref. 3 is recovered.

From Eq. E.2, the velocity ratio across the liner is related to the impedances on both sides as

$$\frac{v_f}{v_b} = \left(1 - \frac{i\omega}{K_\ell} Z_b\right) / \left(1 + \frac{i\omega}{K_\ell} Z_f\right) \tag{E.4}$$

where

$$Z_f = P_f/v_f$$

is the impedance looking into the blanket from the fluid and

$$Z_b = P_b/v_b$$

is the impedance backing the lining.

The liner velocity v_ℓ can be eliminated from Eq. E.1 and E.3 giving

$$\frac{1}{2}\,(1+v_b/v_f) = \left(\frac{i}{\omega M_\ell} + \frac{1}{R_\ell}\right)\,(Z_f - Z_b v_b/v_f) \tag{E.5}$$

Substituting for the velocity ratio v_f/v_b from Eq. E.4 gives the backing impedance Z_b in terms of the liner parameters and the fluid impedance Z_f. This yields

$$Z_b = \frac{1+\left\{\frac{i\omega}{2K_\ell} - \frac{i}{\omega M_\ell} - \frac{1}{R_\ell}\right\} Z_f}{\frac{i\omega}{2K_\ell} - \left(\frac{i}{\omega M_\ell} + \frac{1}{R_\ell}\right)(1+ \frac{i2\omega}{K_\ell}\, Z_f)} \tag{E.6}$$

Alternatively the impedance looking into the blanket can be expressed in terms of the backing impedance as follows:

$$Z_f = \frac{\left(\frac{i}{\omega M_\ell} + \frac{1}{R_\ell}\right)^{-1}\left(1- \frac{i\omega}{2K_\ell}\, Z_b\right)+Z_b}{1- \frac{2i\omega}{K_\ell}\, Z_b - \frac{i\omega}{2K_\ell}\left(\frac{i}{\omega M_\ell} + \frac{1}{R_\ell}\right)^{-1}} \tag{E.7}$$

The ratio of fluid to shell velocities is obtained in terms of the fluid impedance and blanket parameters by substituting Eq. E.6 in to Eq. E.4.

The normal incidence absorption coefficient of the acoustical blanket is calculated assuming normal incidence on a rigidly backed layer. Under the assumption of large mass impedance compared to resistance, the impedance Z_f in Eq. E.7 with Z_b infinite is given by

$$Z_f = \frac{1}{4}\, R_\ell + \frac{i}{2\omega}\, K_\ell \tag{E.8}$$

The absorption coefficient α is expressed using Z_f as

$$\alpha = 1 - \left|\frac{Z_f - \rho c}{Z_f + \rho c}\right|^2 \tag{E.9}$$

For typical materials, the stiffness of the liner is expected to be dominated by that of the air in the pores with the matrix skeleton being relatively soft. Thus we assume the stiffness K_ℓ of the layer to be that of a column of air with length given by the thickness of the liner; that is,

$$K_\ell = \gamma P_a / h_\ell \tag{E.10}$$

where

P_a is atmospheric pressure

h_ℓ is the layer thickness, and

γ is the ratio of specific heats which equals 1.4 for air.

Fig. II.7 shows the absorption coefficient obtained from this model for a reasonably dense Fiberglass ($\rho_\ell = 1.1 \times 10^{-6}$ lbf-s^2/in^4=11.2 kg/m^3) having a flow resistance of 5.5×10^{-3} lbf-s/in^4 (5.8×10^4 N-s/m^4). The specific flow resistance per unit thickness or flow resistivity is taken from Ref. 3. In the frequency range of Fig. II.7 the absorption coefficient increases with both frequency and liner thickness. The absorption values and trends shown on Fig. II.7 are in reasonable agreement with measurements made on similar materials (see Ref. 21).

APPENDIX F

WAVENUMBER SPECTRUM

APPENDIX F

WAVENUMBER SPECTRUM

The wavenumber spectrum of a response field is defined as the power spectrum resulting from the Fourier transform of the spatial distribution of the response. Of particular interest is the response field along the length of the fuselage. For the simply-supported shell the radial acceleration and the pressure can both be represented over the span $0 \leq x \leq L$ in terms of the following modal summation (see Appendix B):

$$f(x,\phi) = \sum_n \sum_m F_{mn} \sin k_m x \cos n\phi \tag{F.1}$$

where $f(x,\phi)$ is the response function, F_{mn} are the corresponding modal amplitudes and $k_m = m\pi/L$. The Fourier transform of this response field is given by

$$\tilde{f}(k,\phi) = \int_{x_1}^{x_2} f(x,\phi) e^{-ikx} dx \tag{F.2}$$

where $x_1 \leq x \leq x_2$ is the spatial aperture of interest. The wavenumber spectrum is then defined as the following power spectrum (Ref. 22):

$$\tilde{F}(k,\phi) = \frac{|\tilde{f}(k,\phi)|^2}{2\pi\ell} \tag{F.3}$$

where $\ell \equiv x_2 - x_1$.

When Eq. F.1 is substituted into Eq. F.2, the Fourier transform of the spatial field is obtained in the following form:

$$\tilde{f}(k,\phi) = \sum_n \sum_m A_{nm} I_{mk} \cos n\phi \tag{F.4}$$

$$I_{mk} = \frac{1}{(k^2 - k_m^2)} \left[e^{-ikx_2} (k_m \cos k_m x_2 + ik \sin k_m x_2) - e^{-ikx_1} (k_m \cos k_m x_1 + ik \sin k_m x_1) \right] \tag{F.5}$$

For the arbitrary aperture, all modes contribute to the transform at each value of spatial wavenumber. The wavenumber spectrum is obtained by substituting Eqs. F.4 and and F.5 into Eq. F.3.

APPENDIX G

THE CONTRIBUTION OF MEMBRANE (COMPRESSIONAL) WAVES IN A CYLINDRICAL SHELL TO INTERIOR NOISE LEVEL PREDICTIONS

APPENDIX G

THE CONTRIBUTION OF MEMBRANE (COMPRESSIONAL) WAVES IN A CYLINDRICAL SHELL TO INTERIOR NOISE LEVEL PREDICTIONS

The wing and fuselage structures of the Beechcraft Baron consist of nonplanar, orthogonally stiffened thin skins. Characteristic dimensions are the skin thickness 0(.1 cm.), the rib or stringer depths 0(1-10 cm.), the rib or stringer spacings $0(10-10^2$ cm.), and the overall aircraft dimensions $0(10^2 - 10^3$ cm.). For stiffened skin constructions SEA subsystems are generally chosen to be of the scale of the framing spacings, requiring the analysis of coupling loss factors among adjacent skin panels and framing segments (Refs. 16, 17). Thus the SEA requirement that the characteristic length of a subsystem (L_c) measure many wavelengths, say N, yields $L<L_c/N$. For example, taking $L_c=30$ cm. simple flexure in .1 cm. aluminum plating satisfies this criterion above $f(Hz)>200xN^2$ or, taking N=2, f>800 Hz. A more stringent limitation results if one considers compressional waves, namely f(Hz)>17,000xN or, again taking N=2, f>34 kHz. For this reason SEA techniques are rarely applied to structural-acoustic problems for which compressional waves may be of significance. The role of such waves for the problem at hand may be investigated by exercising the cylindrical fuselage model described in Section II. Presented in Figs. G.1a and b are cabin noise predictions at two interior locations for a point force drive positioned as shown, with and without the inclusion of membrane (compressional) wave terms. In the absence of membrane waves the cylinder responds in flexure only. In this comparison the cylinder is bare, that is no stiffeners are modelled, and we note that all frequencies plotted are below the ring frequency of the shell. Differences in predicted levels in excess of 10 dB are observed. Significant dynamic coupling between compressional and flexural waves in fuselage stiffening members can also be anticipated. Thus analyses that exclude such waves may be limited in both their ability to replicate data and assess potential benefits of noise control measures regardless of their precision in modelling other details.

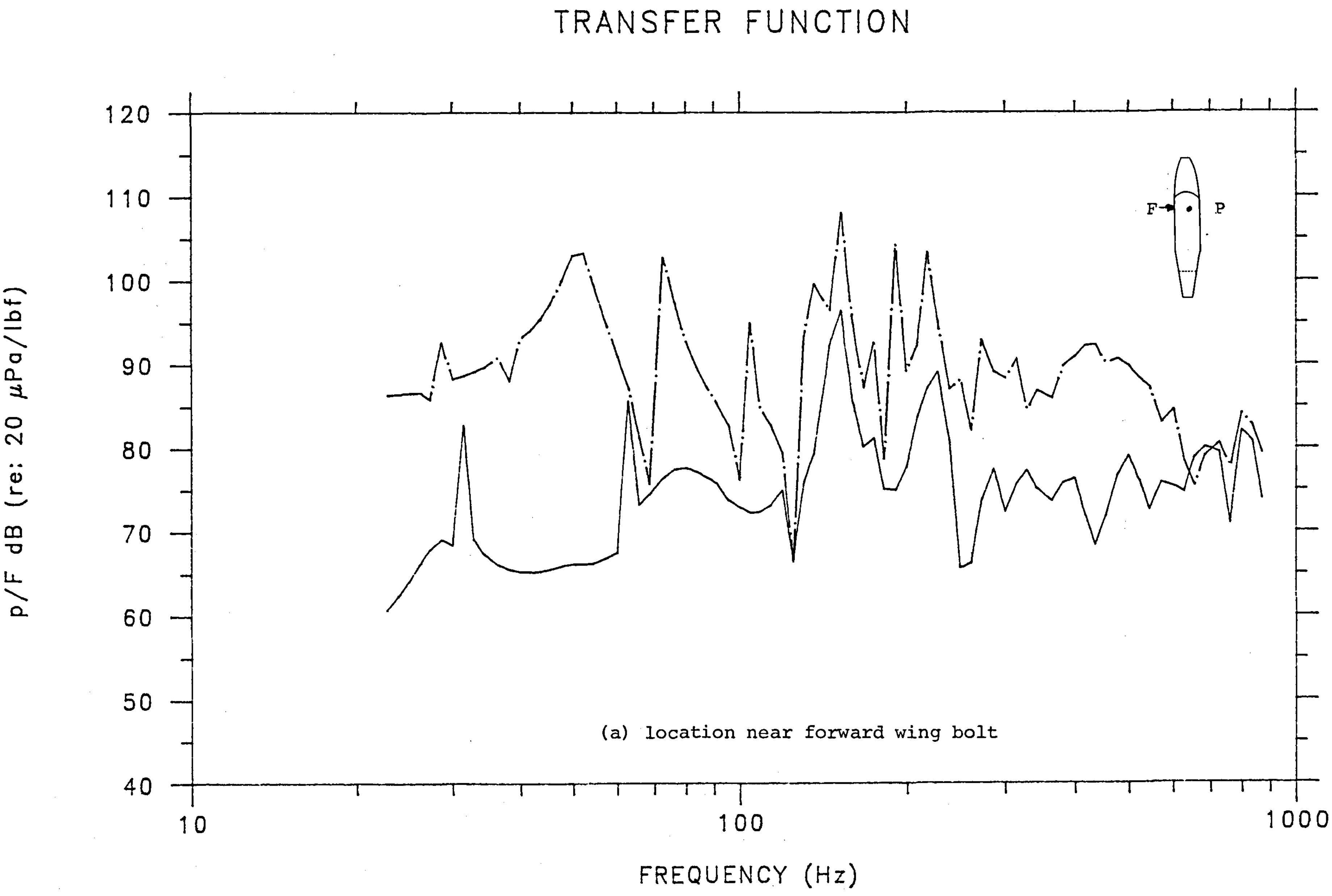

Fig. G.1a Interior noise level predictions for a force driven bare cylindrical shell with (—·—) and without (——) the inclusion of membrane waves.

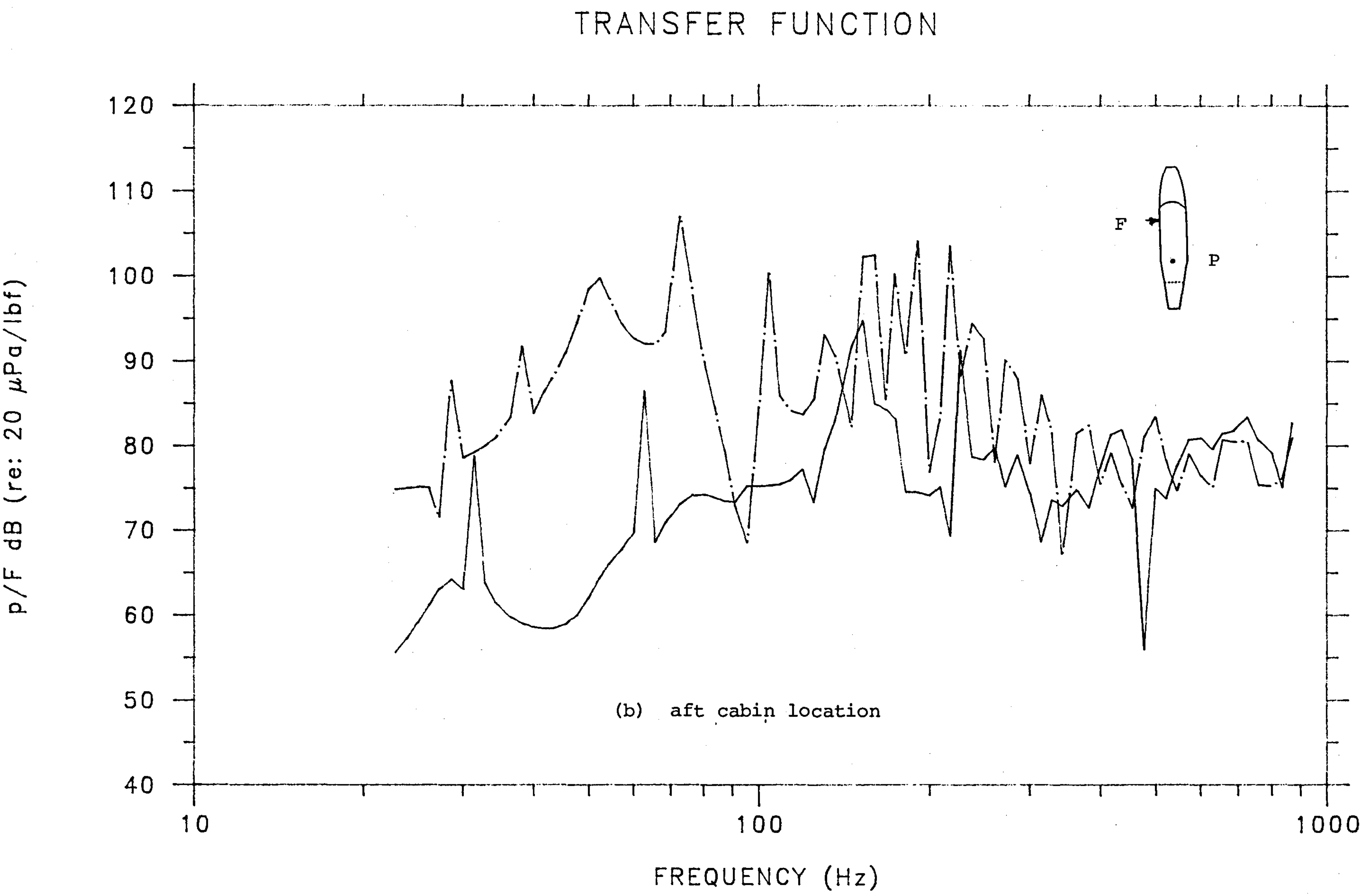

Fig. G.1b Interior noise level predictions for a force driven bare cylindrical shell with (—·—) and without (——) the inclusion of membrane waves.

National Aeronautics and Space Administration

Report Documentation Page

1. Report No. NASA CR-4136	2. Government Accession No.	3. Recipient's Catalog No.

4. Title and Subtitle
Analytical Modeling of the Structureborne Noise Path on a Small Twin-Engine Aircraft

5. Report Date
June 1988

6. Performing Organization Code

7. Author(s)
J.E. Cole III, A. Westagard Stokes, J.M. Garrelick, and K.F. Martini

8. Performing Organization Report No.
U-1541-349 (Part I)

10. Work Unit No.
535-03-11-03

9. Performing Organization Name and Address
Cambridge Acoustical Associates, Inc.
80 Sherman Street
Cambridge, MA 02140

11. Contract or Grant No.
NAS1-18020

13. Type of Report and Period Covered
Contractor Report

12. Sponsoring Agency Name and Address
National Aeronautics and Space Administration
Langley Research Center
Hampton, VA 23665-5225

14. Sponsoring Agency Code

15. Supplementary Notes
Langley Technical Monitor: William H. Mayes

16. Abstract

The structureborne noise path of a six passenger twin-engine aircraft is analyzed. Models of the wing and fuselage structures as well as the interior acoustic space of the cabin are developed and used to evaluate sensitivity to structural and acoustic parameters. Different modeling approaches are used to examine aspects of the structureborne path. These approaches are guided by a number of considerations including the geometry of the structures, the frequency range of interest, and the tractability of the computations. Results of these approaches are compared with experimental data.

17. Key Words (Suggested by Author(s))
Structureborne Noise
Propeller Noise
Aircraft Vibrations and Noise
Cabin Interior Noise

18. Distribution Statement
Unclassified - Unlimited
Subject Category 71

19. Security Classif. (of this report) Unclassified	20. Security Classif. (of this page) Unclassified	21. No. of pages 136	22. Price A07

NASA FORM 1626 OCT 86

NASA-Langley, 1988

For sale by the National Technical Information Service, Springfield, Virginia 22161-2171

End of Document